STUDY ON STEEL-CORED CONDUCTORS FOR AMPACITY CALCULATION: EXPERIMENTS AND MODELING

Ruyguara Alcantara Meyberg

Tese de Doutorado apresentada ao Programa de Pós-graduação em Engenharia Elétrica, COPPE, da Universidade Federal do Rio de Janeiro, como parte dos requisitos necessários à obtenção do título de Doutor em Engenharia Elétrica.

Orientadores: Antonio Carlos Siqueira de Lima
Maria Teresa Correia de Barros

Rio de Janeiro
Janeiro de 2021

STUDY ON STEEL-CORED CONDUCTORS FOR AMPACITY CALCULATION: EXPERIMENTS AND MODELING

Ruyguara Alcantara Meyberg

TESE SUBMETIDA AO CORPO DOCENTE DO INSTITUTO ALBERTO LUIZ COIMBRA DE PÓS-GRADUAÇÃO E PESQUISA DE ENGENHARIA DA UNIVERSIDADE FEDERAL DO RIO DE JANEIRO COMO PARTE DOS REQUISITOS NECESSÁRIOS PARA A OBTENÇÃO DO GRAU DE DOUTOR EM CIÊNCIAS EM ENGENHARIA ELÉTRICA.

Orientadores: Antonio Carlos Siqueira de Lima
Maria Teresa Correia de Barros

Aprovada por: Prof. Antonio Carlos Siqueira de Lima
Profª. Maria Teresa Correia de Barros
Dr. Antônio Paulo Cardillo Magalhães
Prof. Alberto Resende De Conti
Prof. Mauricio Valencia Ferreira da Luz
Dr. Carlos Kleber da Costa Arruda

RIO DE JANEIRO, RJ – BRASIL
JANEIRO DE 2021

Meyberg, Ruyguara Alcantara

Study on steel-cored conductors for ampacity calculation: experiments and modeling/Ruyguara Alcantara Meyberg. – Rio de Janeiro: UFRJ/COPPE, 2021.

XVI, 113 p.: il.; 29, 7cm.

Orientadores: Antonio Carlos Siqueira de Lima
Maria Teresa Correia de Barros

Tese (doutorado) – UFRJ/COPPE/Programa de Engenharia Elétrica, 2021.

Referências Bibliográficas: p. 81 – 87.

1. Steel-cored Conductors. 2. Experimental Study. 3. Electromagnetic Modeling. 4. Alternating Current Resistance. 5. Conductor Design. I. Lima, Antonio Carlos Siqueira de *et al.* II. Universidade Federal do Rio de Janeiro, COPPE, Programa de Engenharia Elétrica. III. Título.

Agradecimentos

Agradeço a Deus por ter me dados as condições para realizar esta tese e me conduzido por este caminho pelo qual tive grandes experiências e realizações, acompanhado sempre de pessoas excepcionais.

Agradeço à minha família, em especial aos meus filhos Manuela e Benjamin, à minha esposa Helena e aos meus pais Tito Lívio (em memória) e Elisete, por todo carinho e imenso apoio, em tempos de alegrias, surpresas e saudades.

Sou imensamente grato aos meus orientadores, professor Antonio Carlos e professora Maria Teresa, não só pela orientação, dedicação e apoio para a realização desta tese, como também pela amizade, aprendizado e imprescindível apoio oferecido neste período.

Agradeço muitíssimo também ao meu supervisor, pesquisador Luís Adriano, pelas orientações e o extraordinário apoio em todo este tempo em que estive no CEPEL. Muito obrigado.

Sou também muito grato ao pesquisador Farith pelo apoio, aprendizado e pela sua valiosa amizade. Agradeço o apoio de toda a equipe dos laboratórios do CEPEL: *Laboratório de Propriedades Elétricas e Magnéticas* e o *Laboratório de Alta Corrente*, aos demais colegas do *Departamento de Linhas de Transmissão e Equipamentos* do CEPEL, colegas da COPPE/UFRJ e do Instituto Superior Técnico/IST.

Resumo da Tese apresentada à COPPE/UFRJ como parte dos requisitos necessários para a obtenção do grau de Doutor em Ciências (D.Sc.)

ESTUDO SOBRE CONDUTORES DE ALMA DE AÇO PARA CÁLCULO DE AMPACIDADE: EXPERIMENTOS E MODELAGEM

Ruyguara Alcantara Meyberg

Janeiro/2021

Orientadores: Antonio Carlos Siqueira de Lima
Maria Teresa Correia de Barros

Programa: Engenharia Elétrica

A magnetização da alma de condutores de alumínio com alma de aço (CAA) pode afetar a distribuição de corrente e a resistência do condutor, dependendo de fatores como a intensidade da corrente conduzida, número de camadas de alumínio e propriedades magnéticas do aço. Entretanto, o efeito desta magnetização é geralmente representado de forma simplificada no cálculo da ampacidade destes condutores.

Esta tese apresenta um estudo sobre os efeitos da magnetização da alma de aço, seus modelos de cálculo e o uso destes modelos no cálculo da ampacidade de linhas, especialmente diante da possibilidade de aumento da ampacidade destes condutores. São realizados estudos experimentais sobre um condutor CAA e sobre sua alma, e desenvolvidos um modelo eletromagnético para cálculo da distribuição de corrente e resistência destes condutores e um algoritmo para incluir no modelo o gradiente radial de temperatura de regime permanente. O modelo desenvolvido é então usado para obtenção do cálculo aperfeiçoado da ampacidade para até elevadas correntes.

Os resultados experimentais mostram variações inesperadas da permeabilidade do aço em valores de temperatura ainda não investigados e uma redistribuição das correntes do condutor durante o seu aquecimento. Através do novo modelo mostra-se que esta redistribuição ocorre devido ao gradiente radial de temperatura. Mostra-se também que as correntes nas camadas de aço podem ter um papel na redução da magnetização da alma, sendo possível reduzir perdas através do projeto da alma de aço. Por fim, mostra-se que a ampacidade de condutores de alma de aço calculada pelos modelos existentes tende a ser superestimada para altas correntes e, acentuadamente, quando o condutor possui apenas uma camada de alumínio, representando um alto risco de acidentes.

Abstract of Thesis presented to COPPE/UFRJ as a partial fulfillment of the requirements for the degree of Doctor of Science (D.Sc.)

STUDY ON STEEL-CORED CONDUCTORS FOR AMPACITY CALCULATION: EXPERIMENTS AND MODELING

Ruyguara Alcantara Meyberg

January/2021

Advisors: Antonio Carlos Siqueira de Lima
Maria Teresa Correia de Barros

Department: Electrical Engineering

The core magnetization of aluminum conductors steel reinforced (ACSR) can affect their resistance and current distribution, depending on factors such as the intensity of the carried current, number of aluminum layers, and the steel magnetic properties. However, the effect of this magnetization is generally represented in a simplified way when calculating the ampacity of these conductors.

This thesis presents a study on the effects of the steel core magnetization, their calculation models, and the use of these models in the ampacity calculation of overhead lines, especially from the perspective of increasing the ampacity of these conductors. Experimental studies are carried out on an ACSR conductor and its steel core, and it is developed an electromagnetic model for calculating the current distribution and resistance of these conductors and an algorithm for including in this model the steady-state radial temperature gradient. The developed model is then used to obtain an improved calculation of the ampacity for up to high currents.

The experimental results show unexpected variations in the steel permeability at temperature values not investigated before and a current redistribution during the conductor heating. Calculations using the new model show that this current redistribution is caused by the radial temperature gradient. It is also shown that the currents in the steel layers can play a role in reducing the core magnetization and that it is possible to reduce losses by changing the design of the steel core. Finally, it is shown that the ampacity of steel-cored conductors calculated using existing models tends to be overestimated for high currents and, severely, when the conductor has only one aluminum layer, representing a high risk of accidents.

Contents

List of Figures

List of Tables

List of Abbreviations

ACSR	Aluminum conductor steel reinforced
ACSS	Aluminum conductor steel suported
ANEEL	*Agência Nacional de Energia Elétrica*
CEPEL	*Centro de Pesquisas de Energia Elétrica*
CIGRÉ	*International Council on Large Electric Systems*
CT	Current transformer
DLR	Dynamic Line Rating
IEEE	Institute of Electrical and Electronics Engineers
SPM	Secondary permeability maximum
T-ACSR	Thermal resistant aluminum conductor, steel reinforced

Chapter 1

Introduction

Power utilities are facing a need to increase the power transmission capacity in existing circuits be it for environmental restrictions or the high costs related to the construction of new transmission lines. This scenario led to an increase in the interest in technologies related to maximize the current carrying capacity (ampacity) of overhead lines. Among these, the Dynamic Line Rating (DLR) has received some attention [1–6]. Traditionally, the transmission line current capacity is set based on conservative static or seasonal weather conditions [7, 8]. DLR uses real-time monitored or estimated environmental conditions to compute the additional current capacity [1, 9], which can be up to 100% [6]. Another technology is the development of improved current capacity conductors, which can operate continuously at higher temperatures and even reduced sag [10–12]. Having a higher thermal limit and a lower expansion coefficient than conventional conductors, their current capacity is increased. The ACSS (for aluminum conductor steel supported), for example, made from annealed aluminum wires and zinc-5% aluminum-Michmetal alloy-coated steel core, can operate at temperatures up to 250 °C without loss of strength, while the maximum operating temperature for conventional ACSR (for aluminum conductor steel reinforced) is 90 °C [13]. In some cases, an ACSS conductor can double the current capacity of a conventional ACSR of equivalent diameter [11].

With the increase in the current capacity, however, steel-cored conductors require special attention. These conductors are widely used in overhead lines, consisting of concentric layers of aluminum wires helically wound over a core of galvanized steel wires as depicted in Fig. 1.1. The steel core is magnetized when the conductor has an odd number of aluminum layers, causing losses due to hysteresis and eddy currents, affecting the conductor AC resistance. The intensity of the core magnetization depends on the (odd) number of aluminum layers, being stronger in conductors with a single aluminum layer, moderate in three-layer conductors, and it may be disregarded for conductors with five or more aluminum layers. [14]. In the case of three-layer conductors, the magnetic flux in the steel core also results in a redistribution

of current between the aluminum layers, known as the *transformer effect* [15–18], which modifies the internal transient temperature of the conductor [19–21] and its AC resistance. The magnetic flux in the core, in turn, depends on the steel permeability (which varies with temperature and mechanical stress [22]), as well as on the frequency [23, 24] and intensity of the current carried by the conductor. With the increase in the current capacity of such conductors, the core magnetization can reach higher levels, for which investigations are not found in the literature. This perspective of strengthening the magnetization of steel core also increases the importance of the correct modeling of the phenomenon and the search for possible mitigations.

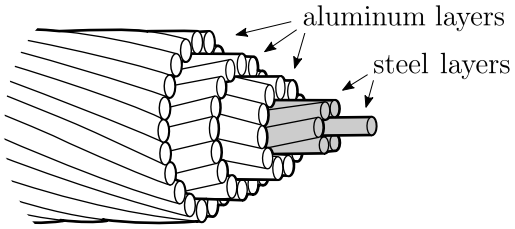

Figure 1.1: Illustration of a steel-cored conductor with 3 aluminum layers.

This thesis presents a study conducted on the effects of the core magnetization of steel-cored conductors on their resistance and current distribution, on their calculation models, and their use in calculating the ampacity of overhead lines. It addresses aspects that have not yet been investigated experimentally and limitations in the electromagnetic modeling of these conductors, especially from the perspective of increasing their current carrying capacity. The specific motivations and objectives of each aspect addressed in this thesis are following.

1.1 Motivation and Objectives

1.1.1 Impact of the AC Resistance Calculation Model on the Ampacity of Transmission Lines with Conventional Steel-Cored Conductors

Traditionally, the effect of the steel core magnetization on three-layer conductor resistance is accounted for by a multiplying factor, based on experimental data, as a function of the total current value of the conductor [14, 25, 26]. This approach is used in the two main methodologies for calculating the carrying capacity of overhead lines, developed by IEEE [27] and CIGRÉ [28].

However, the core magnetization depends not only on the value of the total current carried by the conductor but also on the frequency and on the permeability

of the steel core, which varies with temperature and mechanical stress. These aspects can be properly accounted for using the *equivalent circuit models* proposed in [15, 16], which represents each aluminum layer as an equivalent circuit, with resistances and inductances associated to the longitudinal and circular magnetic flux internal to the conductor. Core losses are accounted for by means of the complex permeability of the steel core. Despite the accuracy of the model in calculating the conductor AC resistance and the ability to consider the several aspects that affect the steel core magnetization, these models are not used in the main ampacity calculation methodologies.

One of the objectives of this thesis is to analyze the impact of using the existing *equivalent circuit model* in the calculation of overhead line ampacity for typical maximum operating conditions of conventional steel-cored conductors, comparing it with the other models used in the main ampacity calculation methodologies (IEEE, CIGRÉ) and with the current Brazilian methodology [29]. The ampacity calculation method based on the existing *equivalent circuit model* will be later used as a background for analyzing the advances made in this thesis on the ampacity calculation of steel-cored conductors.

1.1.2 Experimental Studies

Study on the magnetic properties of the steel core

One of the advantages of using the *equivalent circuit model* is to account for the magnetic losses in steel core by means of complex permeability and to be able to represent its variations with temperature and mechanical stress. Naturally, it is necessary that the complex permeability is known for the different magnetic field strengths, temperature and mechanical stresses that can occur in the conductor's operation.

The permeability variation with temperature, at constant magnetic field strength and tensile stress, was measured by several authors on steel wires of different diameters and over different temperature ranges. Double [30] carried out the measurements on a single galvanized steel wire of 4.5 mm diameter taken from an ACSR conductor, in the range from 16 °C to 52 °C. Matsch and Lewis [31] measured the variation of the permeability on galvanized steel wires of diameter from 1.61 mm to 4.79 mm, over the range from 20 °C to 100 °C. The same variation was measured by Morgan and Price [32] on wires of 2.69 mm, 3.12 mm and 3.56 mm diameter, over the range from 20 °C to 130 °C. Later, the measurement was made by Riaz [33] on wires of diameter from 2.36 mm to 4.78 mm, over the range from 0 °C to 150 °C, and Morgan et al. [22], on a steel core of 2.24 mm diameter wires taken from a "*Grackle*" ACSR conductor, in the range from 25 °C to 120 °C. All authors reported

the increase of permeability with temperature, which was attributed to a reduction in the internal strains in the crystals and in the anisotropy of the crystal structure with increasing temperature [22].

The temperature range covered by the authors was from 0 °C to 150 °C, which exceeds the maximum emergency overload temperatures of conventional conductors. However, an ACSS conductor, having the same steel core of a conventional ACSR conductor but with annealed aluminum wires, can operate up to 200 °C [34]. The magnetic properties of the steel core at these higher temperatures, which the improved current capacity conductors may reach, should be investigated.

One of the objectives of this thesis is to investigate the magnetic properties of the steel core of an ACSR conductor at higher temperatures. For this purpose, experimental work was carried out on a sample of the steel core taken from an ACSR "*Duck*" conductor, which was used in the experimental studies of this thesis. Conductor details are given in Appendix A.1.

Study on the transformer effect

The AC resistance is an essential electrical parameter that may be obtained by many measurement techniques [24]. It is measured in several studies on the *transformer effect*, its variation with the conductor total current value [15, 24, 35, 36], power frequency [23, 24] and temperature [24] being analyzed. The measurement of current distribution between layers of a steel-cored conductor is a more complex task, only being reported in [15]. In this reference, the current density of each layer was measured by means of voltage probes, installed on the outer surface of a randomly selected wire of each layer. All the aluminum wires were unwrapped for the probes installation and the current was injected during a limited number of cycles, avoiding heating the conductor. The effect of the conductor heating on current density redistribution was not measured but only calculated [17], considering the variation of the core permeability with temperature.

The calculation of the conductor current distribution is necessary for its correct thermal modeling [19, 20], whose importance is highlighted by the increase in the current capacity of lines, in order to ensure its integrity and the transmission line safe operation.

One objective of this thesis is, therefore, to investigate the current distribution in an ACSR conductor during its heating, supplied with currents up to 6 kA. For this, a series of laboratory experiments is carried out on an ACSR "*Duck*" conductor (details of the conductor are given in the Appendix A.1). The experimental arrangement is designed in order to allow the simultaneous measurement of the current in all aluminum wires of the conductor and to keep the maximum conductor length undisturbed.

1.1.3 Modeling of Steel-Cored Conductors

Improving the equivalent circuit model

In the validation of Barrett's *equivalent circuit model* [15], it was used experimental data of an ACSR "*Grackle*" conductor at 20 °C with its three aluminum layers and with its inner aluminum layer only (obtained by removing its outer aluminum layers). The results show good agreement for the measured AC/DC resistance ratio of the three-layer "*Grackle*" conductor. In the case of a single-layer conductor, however, the same accuracy is not observed for higher current values. According to its authors, the discrepancy occurs because the model does not represent the spiral current flow in the steel core and the circular magnetic flux within it, yet the model has good accuracy in the normal operating current range. However, with the prospect of increasing the current capacity of overhead lines by technologies such as Dynamic Line Rating (DLR) [3] and the development of improved capacity conductors, the development of a comprehensive model, capable of accurately calculating the AC resistance variation of conductors with any number of aluminum layers in a wider current range is necessary.

In addition, electromagnetic modeling also represents an important tool for the design of steel-cored conductors [17, 37], allowing to identify adjustments in the lay length and wire diameter in each layer that reduce power losses resulting from the core magnetization. However, as the existing models represent the steel core in a simplified way, as a single circuit, and of not-spiraled current, the changes in conductor design have been limited to the aluminum layers. Furthermore, such optimization has been applied to three-aluminum layer conductors only [17, 37], in spite the fact that optimization is further important in conductors with a single aluminum layer, as they have higher losses due to the core magnetization. A significant loss reduction of these conductors can only be achieved by optimizing the steel core, thus being utmost important that each steel layer is appropriately represented.

One objective of this thesis is the development of an electromagnetic model for the calculation of the AC resistance and current distribution of steel-cored conductors in which the representation of the steel core is refined, aiming to overcome the limitations of the existing models.

Including steady-state thermal behavior in electromagnetic modeling

It has been reported in the literature that steady-state radial temperature differences between the steel core and the conductor surface ranging from 10 °C to 25 °C have been measured [27] and can reach up to 30 °C [38]. Indeed, there is a radial temperature gradient that becomes relevant in ACSR conductors with three or more aluminum layers at current densities above 1 A/mm^2, increasing with the

total current value [27]. This temperature difference must be included in the electromagnetic model when dealing with higher currents, in which this temperature gradient becomes significant.

One of the objectives of this thesis is, therefore, the development of a calculation algorithm that includes the steady-state radial temperature gradient in the calculation of the current distribution and the AC resistance of steel-cored conductors, since the presence of this temperature gradient at high current values cannot be further neglected.

Improved prediction of transmission line ampacity

The last of the objectives of this thesis is to gather the advances made in the present work on the calculation of the AC resistance of steel-cored conductors, obtaining an improved ampacity calculation method for these conductors. Then, it is aimed to analyze the impact of using this method on the ampacity calculation of steel-cored conductors with improved current capacity, comparing it with those used in the main methodologies (IEEE, CIGRÉ) and with the one based on the existing *equivalent circuit* model, considering both maximum operating conditions of conventional conductors as well as of those with improved current capacity.

Therefore, the contributions of this thesis encompass the advances in the experimental study of the phenomenon of the magnetization of steel core and its modeling, as well as the development of appropriate tools for dimensioning the current carrying capacity of these conductors intended for operation at higher current values, which are being widely investigated.

1.2 Thesis Outline

Chapter 2 presents the main electromagnetic phenomena that affect the AC resistance of steel-cored conductors and the models for calculating their resistance considering such phenomena. The calculation models used in the main methodologies for calculating overhead line ampacity are presented. Then, an ampacity calculation method is proposed. Finally, an application example is performed where the ampacity of a conventional steel-cored conductor is calculated using the proposed method and the existing methodologies presented.

Chapter 3 presents the experimental studies on the magnetic properties of an ACSR conductor steel core and on the current distribution (*transformer effect*) in the same conductor. The experimental procedures are presented and then the results with relevant discussions.

Chapter 4 describes a new electromagnetic model developed for steel-cored con-

ductors in order to overcome some limitations identified in the existing models. The developed model is presented, validated with published experimental data and used for the optimization of the conductor design to reduce losses. Then, a calculation algorithm for the inclusion of the steady-state radial temperature gradient in electromagnetic modeling is presented and the effect of this temperature gradient on the current distribution and the conductor resistance is analyzed in application examples. Finally, the advances made through the experimental studies and developments in the calculation of the AC resistance of steel-cored conductors are used in application examples, in which the impacts of including these advances on the ampacity calculation of improved current capacity conductors are analyzed.

Chapter 5 presents the main conclusions drawn during the development of the thesis research and suggestions for future work.

1.3 Publications

The following works were accepted for publication during the development of this thesis:

- LIMA, A. C. S., MAGALHAES, A. P. C., ROCHA, P. E. D., **MEYBERG, R. A.,** CORREIA DE BARROS, M. T. "A Noniterative Approximation of a Full-Wave Model of Thin Wire Above and Buried in a Lossy Ground", *IEEE Transactions on Electromagnetic Compatibility*, pp. 1–9, 2017. doi: 10.1109/temc.2017.2762241.

- **MEYBERG, R. A.**, LIMA, A. C. S., SALAS, F. M. A., et al. "Analysis of AC resistance model of steel-cored conductors on transmission lines ampacity". In: *2018 Simposio Brasileiro de Sistemas Eletricos (SBSE)*. IEEE, may 2018. doi: 10.1109/sbse.2018.8395878.

- **MEYBERG, R. A.**, SALAS, F. M. A., DOMINGUES, L. A. M. C., CORREIA DE BARROS, M. T., LIMA, A. C. S., "Experimental study on the transformer effect in an ACSR cable", *International Journal of Electrical Power & Energy Systems*, 2020, **119**, pp. 105861 doi: 10.1016/j.ijepes.2020.105861.

- **MEYBERG, R. A.**, SALAS, F. M. A., DOMINGUES, L. A. M. C., et al. "Magnetic properties of an ACSR conductor steel core at temperatures up to 230 °C and their impact on the transformer effect", *IET Science, Measurement & Technology*, jan 2021. doi: 10.1049/smt2.12016

- **MEYBERG, R. A.**, CORREIA DE BARROS, M. T., SALAS, F. M. A., DOMINGUES, L. A. M. C., LIMA, A. C. S., "Improvements in electromagnetic

model for steel-cored conductors", *IEEE Transactions on Power Delivery*. doi: 10.1109/tpwrd.2021.3056062

Chapter 2

Background on Transmission Line Ampacity Calculation

2.1 Introduction

This chapter presents the two main electromagnetic phenomena that affect the AC resistance of steel-cored conductors, the *skin effect* and the *steel core magnetization*, as well as the resistance calculation models by which the effects of these phenomena are accounted for. Then, the AC resistance calculation models proposed in the main ampacity calculation methods (IEEE and CIGRÉ), and also in the current Brazilian methodology, are presented and discussed. A methodology for calculating the ampacity using a different resistance calculation model is proposed, and an application example is performed. This new methodology, based on an existing resistance calculation model, is later used as a background in Chapter 4, in order to analyze the advances in the ampacity calculation of the steel-cored conductors made in this thesis.

2.2 Underlying Physical Phenomena

2.2.1 Basic Assumptions

Steel-cored conductors, such as the aluminum conductor steel reinforced (ACSR), are composed of layers of aluminum wires helically wound in alternating directions over a core of layers of steel wires, which are also helically wound in alternating directions. Since the contact resistance between wires is much higher than the resistance of the wires themselves, the current tends to follow the spiral wire path [32, 35, 36], producing a magnetic field with two components, one circular $\mathbf{H}\varphi$ and one longitudinal $\mathbf{H}z$, as depicted in Fig. 2.1 for the current flow in one of the conductor's layers. Note that, in this assumption, the current density $\mathbf{J}$ has two components

($\mathbf{J}\varphi$ and $\mathbf{J}z$), each producing a component of the magnetic field.

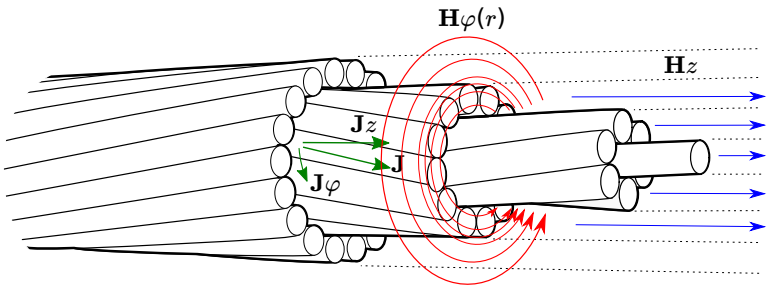

Figure 2.1: Illustration of the current density and magnetic field components resulting from the current flow through the spiral path of the wires.

The circular component of the magnetic field $\mathbf{H}\varphi$ is produced by the longitudinal current component and is concentric to the conductor axis. Assuming the wires to be non-ideal conductors (i.e., their electrical resistivity is different from zero), the circular component is found both inside the wire in which the current flows and around it (see Fig. 2.1). The longitudinal magnetic field $\mathbf{H}z$, in turn, is produced by the circular current component, much like a solenoid, being internal to the conductor (both within the wire in which the current flows and in the area encircled by it) and parallel to its axis. The direction of this longitudinal component is determined by the stranding of the layer.

Each of these components underlies an electromagnetic phenomenon that affects the conductor AC resistance: the *skin effect* and the conductor's *steel core magnetization*, as described below. The *proximity effect*, i.e., the variation of the current density in closely spaced conductors due to non-uniform mutual magnetic inductances [35, 39–41], is not considered between the wires of the same stranded conductor as the circular magnetic field is assumed concentric to the conductor axis, and not to each wire. The *proximity effect*, therefore, is not addressed in this thesis.

2.2.2 Skin Effect

In direct current, the current density in each layer of a stranded conductor, as depicted in Fig. 2.1, whose wires are non-ideal conductors, is uniformly distributed in its cross-section. For alternating current, the current density in each layer is not uniform but increases radially, due to the voltages induced by the *circular* magnetic flux within the wires. This phenomenon is known as the *skin effect* and depends on the frequency, permeability, and the material electrical resistivity [42]. The *skin effect* results in increasing the conductor effective resistance and decreasing its internal inductance [35].

2.2.3 Effect of Steel Core Magnetization

As the layers are stranded with alternate right-hand and left-hand directions, the longitudinal components of the magnetic field produced by adjacent layers are opposed, which tends to cancel the resulting field [25]. In this way, steel-cored conductors with an even number of aluminum layers have the same number of layers producing the longitudinal component in opposite directions and, therefore, the resulting field in their core tends to be canceled [27]. In the case of conductors with an odd number of aluminum layers, the resulting field in the steel core causes power losses due to hysteresis and eddy currents, affecting the conductor AC resistance.

The steel core magnetization is higher in single aluminum layer conductors [14, 26, 27], reducing with the (odd) number of layers, and it may be disregarded for conductors with five or more aluminum layers [14].

In conductors with three aluminum layers, such as ACSR conductors "*Tern*", "*Rail*" and "*Bluejay*", the magnetization of the steel core also changes the current distribution between aluminum layers, causing the current in the middle layer to increase and in the other layers to decrease. This current redistribution is known in the literature as the *transformer effect* [15–18, 23] and modifies the conductor AC resistance and its internal transient temperature [19–21]. The intensity of the *transformer effect* depends on the resulting longitudinal magnetic flux in the core and therefore varies with the current carried by the conductor (see Fig. 2.2), frequency [23, 24] (see Fig. 2.3) and the steel core permeability, which depends on the temperature (see Fig. 2.4) and tensile stress [22].

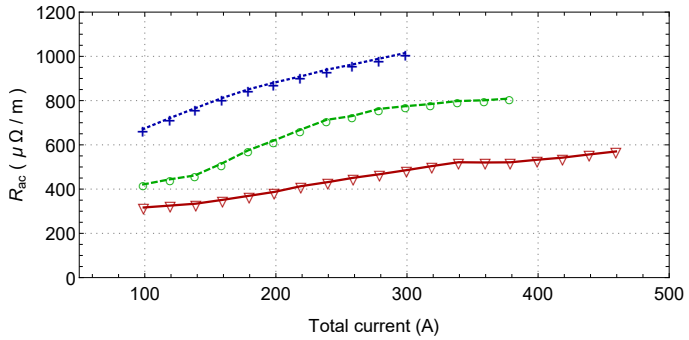

Figure 2.2: Measured variation of the AC resistance with the total current value of single-layer ACSR conductors (6/1) "*Penguin*" (—▽—) and "*Raven*" (···+···), and (12/7) "*Guinea*" (--○--). [43]

2.2.4 Steel Core Magnetic Properties

The steel used in the conductor's core is a magnetic material and, therefore, has specific magnetic properties. Its behavior is characterized by non-linearity and non-reversibility, described by the $B - H$ curves (also known as *hysteresis loops*),

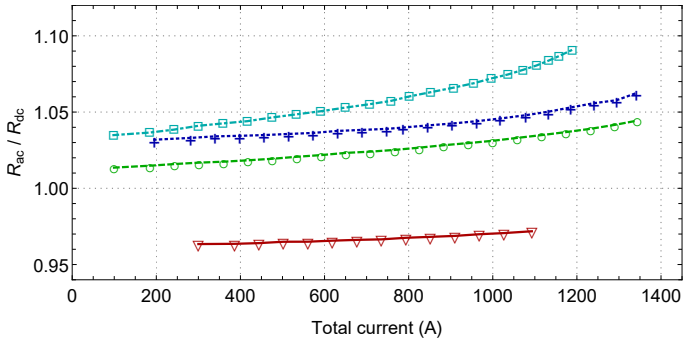

Figure 2.3: Measured variation of the AC/DC resistance ratio with the total current value of a three-layer ACSR "*Paw-Paw*" conductor (54/19) at 25 Hz (—▽—), 40 Hz (--○--), 50 Hz (···+···) and 60 Hz (···□···). [23]

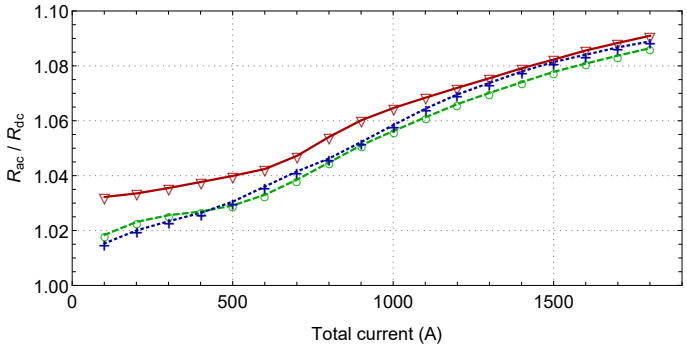

Figure 2.4: Calculated variation of the AC/DC resistance ratio with the total current value of a three-layer ACSR "*Grackle*" conductors (54/19) at 25 °C (—▽—), 80 °C (--○--), and 120 °C (···+···). [17]

represented in Fig. 2.5. Each closed loop represents the cyclic variation of the magnetic induction B in the material for the sinusoidal variation of the magnetic field strength H, showing the dependence of B on the previous magnetic history (hysteresis). By plotting the maximum values of B and H at the tips of the hysteresis loops, the *magnetization curve* of the material is obtained. This curve is also used to describe the material properties, displaying its non-linear characteristics. Fig. 2.6(a) shows the *magnetization curve* obtained from the $B-H$ curve depicted in Fig. 2.5. The non-linearity of the material can also be described by the *permeability curve*, obtained by plotting the permeability μ (defined by the ratio B/H) against H or B. Fig. 2.6(b) shows the *permeability curve* corresponding to the curves depicted in Fig. 2.5 and Fig. 2.6(a), using the relative permeability $\mu_r = \mu/\mu_0$, where μ_0 is the permeability of free space.

In each cycle, represented by a closed loop on the $B-H$ curve depicted in Fig. 2.5, small magnetized regions within the material (called magnetic domains) move in order to align with the applied field H. The energy required for this movement is dissipated as heat, being called *hysteresis losses*, and is proportional to the internal area of the loop and the material volume.

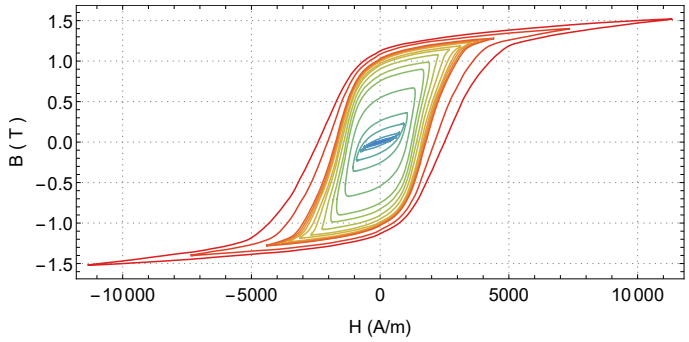

Figure 2.5: $B-H$ curves of a steel core for different magnetic field strengths (measured in [44]).

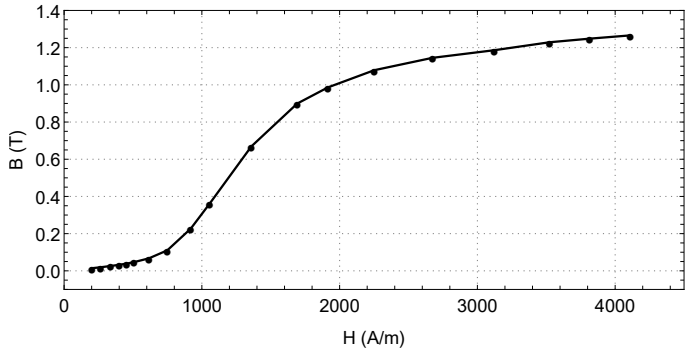

a

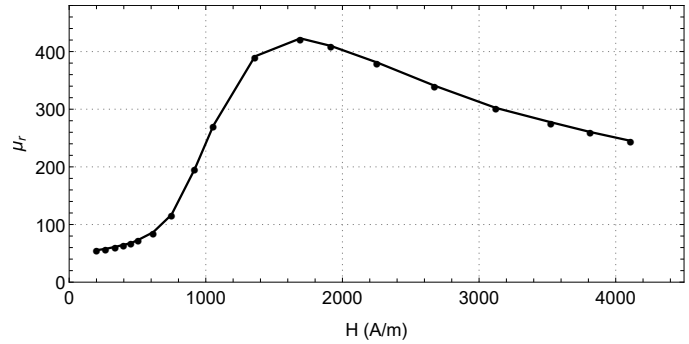

b

Figure 2.6: Variation of the mangetic induction B (a) and relative permeability modulus μ_r (b) of a steel core with magnetic field strength H (measured in [44]).

An alternative way of expressing the material permeability and losses by a single quantity is through the representation of the complex permeability [45], in which the $B-H$ relation is described by an equivalent complex value $\overline{\mu}$, given by

$$\overline{\mu} = \frac{B_p}{H_p} e^{-j\delta} \tag{2.1}$$

where H_p and B_p are the peak value of the magnetic field strength and induction, respectively, and δ is the hysteretic angle, i.e., phase shift between B and H.

In this representation the $B-H$ loop is elliptical, with an area

$$A_{ellipse} = \pi B_p H_p \sin\delta \tag{2.2}$$

which represents the energy losses per unit volume in one cycle. The hysteretic angle δ is then calculated so that the area of the ellipse (2.2) is the same as the measured $B-H$ curve [46–48]. Although the $B-H$ relation is linear only for lower values of H, see Fig. 2.7, δ is calculated so that the same losses from the original curve are accounted for, and thus the permeability and losses are appropriately represented.

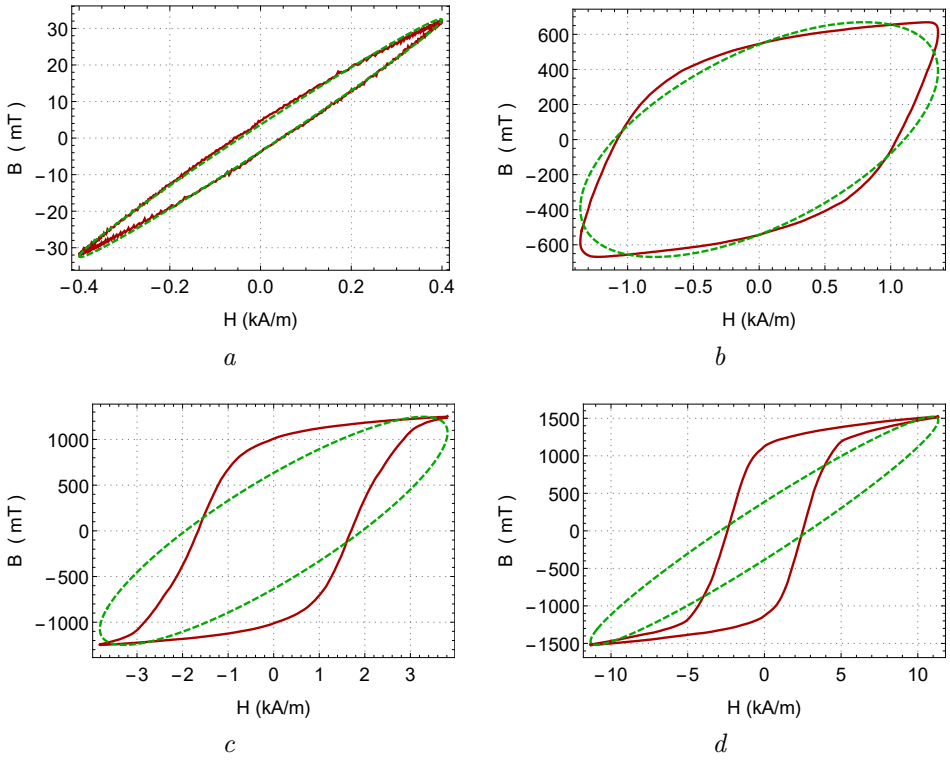

Figure 2.7: Measured $B-H$ curves of a steel core (——) [44] and the corresponding ellipse of the complex permeability (-----), for the sinusoidal variation of the magnetic field strength H, with a maximum value of 400 A/m (a), 1.4 kA/m (b), 3.4 kA/m (c), and 10.1 kA/m (d).

The steel core magnetic properties, in turn, are affected by tensile stress [22, 30, 32] and, most significantly, by the temperature [22, 30–33] as shown in Fig. 2.8, and therefore vary during the line operation.

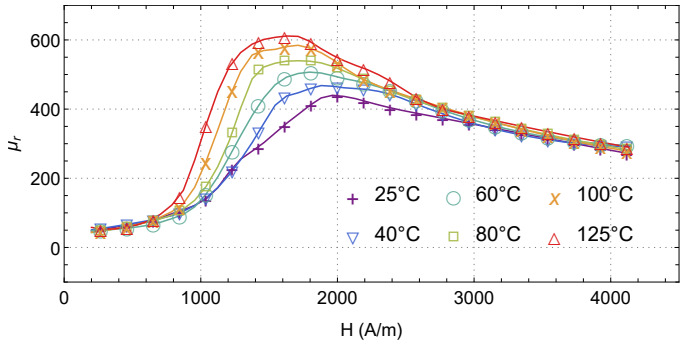

Figure 2.8: Variation of the relative permeability modulus (μ_r) of a steel core with magnetic field strength for different temperature values. [22]

2.3 AC Resistance Models for Steel-Cored Conductors

2.3.1 Model Based on Correction Factors

The AC resistance of steel-cored conductors is traditionally calculated by applying a correction factor due to the *skin effect* k_{se} to the direct current (DC) resistance value R_{dc}. If the conductor has three aluminum layers, a multiplier factor k_m is also applied in order to account for the effects caused by the core magnetization, this depending on the current carried by the conductor I_{ac}, as follows

$$R_{ac} = k_{se} \cdot k_m(I_{ac}) \cdot R_{dc} \tag{2.3}$$

Variations in conductor resistance due to temperature can also be corrected on its DC resistance value, as follows

$$R_{T,dc} = R_{dc}\left[1 + \alpha_i\left(T - 20\right)\right] \tag{2.4}$$

where R_{dc} is the conductor DC resistance at 20 °C, T is the conductor temperature in °C, and α_i is the temperature coefficient of resistance.

A brief description of each correction factor follows.

Correction factor due to the *skin effect*

The correction due to the *skin effect* k_{se} is calculated assuming the conductor to be *tubular* with an internal radius r_i and external radius r_o equal to the outer radius of the steel core and the conductor, respectively, as shown in the Fig. 2.9. According to [35], the error in this approximation is less than 1.44% for conductors with four aluminum layers and less than 1.76% for conductors with two aluminum layers.

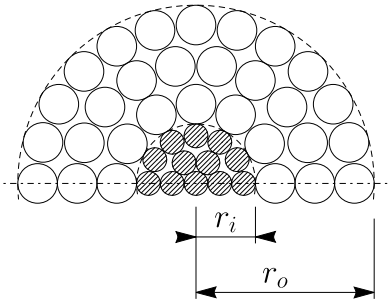

Figure 2.9: Half of the cross-section and corresponding radii of a conductor composed of wires of aluminum (○) and steel (▨).

The correction factor for the *skin effect* k_{se} is found from the AC/DC resistance ratio of the equivalent *tubular* conductor, as follows

$$k_{se} = R_{t,ac}/R_{t,dc} \tag{2.5}$$

where $R_{t,ac}$ is the *tubular* conductor AC resistance, given by [42]

$$R_{t,ac} = Re\left\{\rho\frac{k}{2\pi r_o}\left[\frac{K_1(kr_i)I_0(kr_o) + I_1(kr_i)K_0(kr_o)}{I_1(kr_o)K_1(kr_i) - I_1(kr_i)K_1(kr_o)}\right]\right\} \tag{2.6}$$

where ρ is the material resistivity. I_0 and I_1 are the modified Bessel functions of the first kind, zero and first order, respectively. K_0 e K_1 are the modified Bessel functions of the second kind, zero and first order, respectively. $k = \sqrt{j\omega\mu/\rho}$, where ω is the angular frequency and μ is the material permeability.

$R_{t,dc}$ in (2.5) is the DC resistance of the same *tubular* conductor, given by

$$R_{t,dc} = \frac{\rho}{\pi\left({r_o}^2 - {r_i}^2\right)} \tag{2.7}$$

Multiplier factor due to the steel core magnetization

The multiplier factor due to the core magnetization k_m, used only for steel-cored conductors with three aluminum layers, is based on experimental data [14, 25, 26] and depends on the current carried by the conductor I_{ac}. In [14], two multiplier factors are proposed, one for conductors of high mechanical strength (54/7 and 54/19 stranding) and another for conductors of low mechanical strength (45/7 stranding). On a larger number of samples, a multiplier factor is proposed in [25] for all strandings of three-layer aluminum conductors. The factors proposed in [14] and [25] are represented in Fig. 2.10.

In conductors with a single aluminum layer such as the ACSR conductors (6/1) "*Penguin*" and "*Raven*", and (12/7) "*Guinea*", the core magnetization is even higher, and the multiplier factors are not applied. In this case, the resistance is calculated

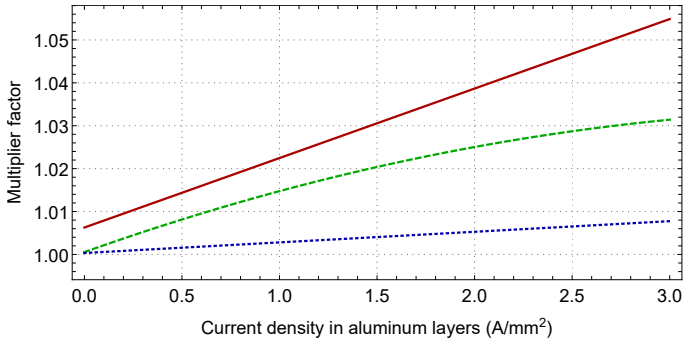

Figure 2.10: Steel core magnetization multiplier factors for ACSR conductors of all strandings (——) [25], conductors of 54/7 and 54/19 strandings (- - - -) [14], and 45/7 stranding (·····) [14].

based on laboratory measurements [14, 26, 27]. It is worth remembering that in the case of conductors with an even number of aluminum layers, the core is not magnetized and, therefore, their AC resistance is calculated only by applying the factor due to the *skin effect* k_{ep} in (2.3).

2.3.2 Equivalent Circuit Models

The equivalent circuit model proposed by Barrett *et al.* [15], like some previous ones [32, 49], represents each aluminum layer as an equivalent circuit, with resistances and inductances associated to the longitudinal and circular magnetic flux internal to the conductor, as illustrated in Fig. 2.11.

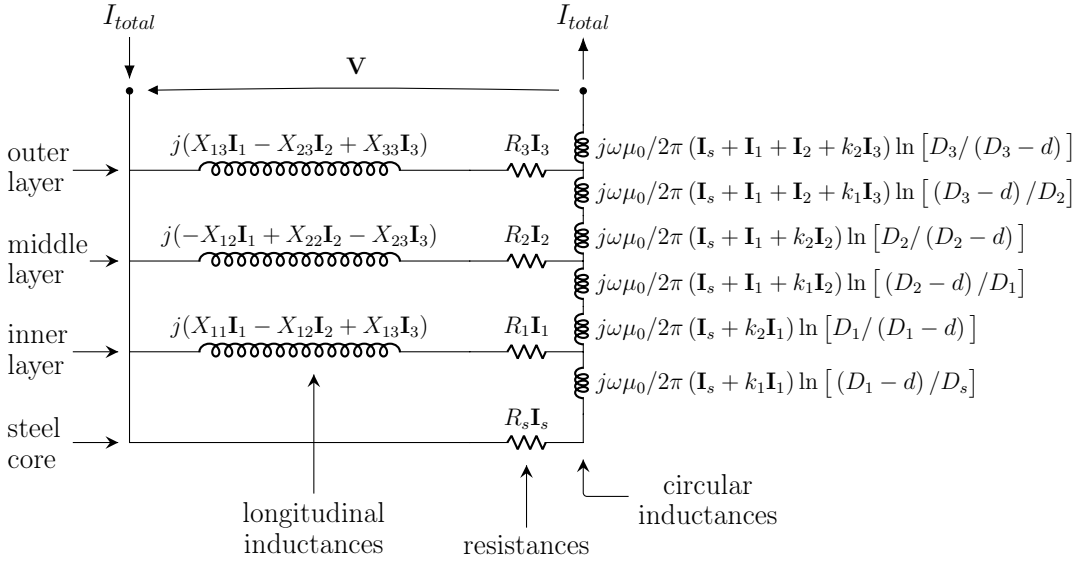

Figure 2.11: Schematic diagram of the equivalent circuit model proposed by [15] for a steel-cored conductor with 3 aluminum layers.

The main contribution of the model by Barrett *et al.* was to account core losses for by means of the complex permeability of the steel core. For a steel-cored conductor with 3 aluminum layers, for example, the voltage drop per meter length on the

conductor surface $\mathbf{V}$ is described by (2.8)-(2.11), as a function of the current flow in the steel core (as if it wasn't spiraled), and the inner, middle and outer aluminum layers, respectively.

$$\begin{aligned}\mathbf{V} =& R_s\mathbf{I}_s + j\frac{\omega\mu_0}{2\pi}\left(\mathbf{I}_s + k_1\mathbf{I}_1\right)\ln\left(\frac{D_1 - d}{D_s}\right) \\ &+ j\frac{\omega\mu_0}{2\pi}\left(\mathbf{I}_s + k_2\mathbf{I}_1\right)\ln\left(\frac{D_1}{D_1 - d}\right) \\ &+ j\frac{\omega\mu_0}{2\pi}\left(\mathbf{I}_s + \mathbf{I}_1 + k_1\mathbf{I}_2\right)\ln\left(\frac{D_2 - d}{D_1}\right) \\ &+ j\frac{\omega\mu_0}{2\pi}\left(\mathbf{I}_s + \mathbf{I}_1 + k_2\mathbf{I}_2\right)\ln\left(\frac{D_2}{D_2 - d}\right) \\ &+ j\frac{\omega\mu_0}{2\pi}\left(\mathbf{I}_s + \mathbf{I}_1 + \mathbf{I}_2 + k_1\mathbf{I}_3\right)\ln\left(\frac{D_3 - d}{D_2}\right) \\ &+ j\frac{\omega\mu_0}{2\pi}\left(\mathbf{I}_s + \mathbf{I}_1 + \mathbf{I}_2 + k_2\mathbf{I}_3\right)\ln\left(\frac{D_3}{D_3 - d}\right)\end{aligned} \tag{2.8}$$

$$\begin{aligned}\mathbf{V} =& R_1\mathbf{I}_1 + jX_{11}\mathbf{I}_1 - jX_{12}\mathbf{I}_2 + jX_{13}\mathbf{I}_3 \\ &+ j\frac{\omega\mu_0}{2\pi}\left(\mathbf{I}_s + k_2\mathbf{I}_1\right)\ln\left(\frac{D_1}{D_1 - d}\right) \\ &+ j\frac{\omega\mu_0}{2\pi}\left(\mathbf{I}_s + \mathbf{I}_1 + k_1\mathbf{I}_2\right)\ln\left(\frac{D_2 - d}{D_1}\right) \\ &+ j\frac{\omega\mu_0}{2\pi}\left(\mathbf{I}_s + \mathbf{I}_1 + k_2\mathbf{I}_2\right)\ln\left(\frac{D_2}{D_2 - d}\right) \\ &+ j\frac{\omega\mu_0}{2\pi}\left(\mathbf{I}_s + \mathbf{I}_1 + \mathbf{I}_2 + k_1\mathbf{I}_3\right)\ln\left(\frac{D_3 - d}{D_2}\right) \\ &+ j\frac{\omega\mu_0}{2\pi}\left(\mathbf{I}_s + \mathbf{I}_1 + \mathbf{I}_2 + k_2\mathbf{I}_3\right)\ln\left(\frac{D_3}{D_3 - d}\right)\end{aligned} \tag{2.9}$$

$$\begin{aligned}\mathbf{V} =& R_2\mathbf{I}_2 - jX_{12}\mathbf{I}_1 + jX_{22}\mathbf{I}_2 - jX_{23}\mathbf{I}_3 \\ &+ j\frac{\omega\mu_0}{2\pi}\left(\mathbf{I}_s + \mathbf{I}_1 + k_2\mathbf{I}_2\right)\ln\left(\frac{D_2}{D_2 - d}\right) \\ &+ j\frac{\omega\mu_0}{2\pi}\left(\mathbf{I}_s + \mathbf{I}_1 + \mathbf{I}_2 + k_1\mathbf{I}_3\right)\ln\left(\frac{D_3 - d}{D_2}\right) \\ &+ j\frac{\omega\mu_0}{2\pi}\left(\mathbf{I}_s + \mathbf{I}_1 + \mathbf{I}_2 + k_2\mathbf{I}_3\right)\ln\left(\frac{D_3}{D_3 - d}\right)\end{aligned} \tag{2.10}$$

$$\begin{aligned}\mathbf{V} =& R_3\mathbf{I}_3 + jX_{13}\mathbf{I}_1 - jX_{23}\mathbf{I}_2 + jX_{33}\mathbf{I}_3 \\ &+ j\frac{\omega\mu_0}{2\pi}\left(\mathbf{I}_s + \mathbf{I}_1 + \mathbf{I}_2 + k_2\mathbf{I}_3\right)\ln\left(\frac{D_3}{D_3 - d}\right)\end{aligned} \tag{2.11}$$

where the subscript s corresponds to the steel core. Subscripts 1, 2 and 3 corresponds to the inner, middle and outer aluminum layers, respectively. ω is the angular frequency, μ_0 is the magnetic permeability of free space, k_1 and k_2 are factors referring to the contribution of circular magnetic flux internal and external to the layers, which depend on the conductor geometry, their calculation is described in Appendix B. $\mathbf{I}_i$ is the current in the i-th layer and D_i is the outer diameter of this layer. d is the aluminum wire diameter, and R_i is the resistance of layer i, given by

$$R_i = \frac{\rho_i}{A_i}\sqrt{1 + \left[\frac{\pi \cdot (D_i - d)}{\lambda_i}\right]^2} \tag{2.12}$$

where ρ_i is the material resistivity, $A_i = n_i\pi d^2/4$ is the layer area, n_i and λ_i are the number of wires and the lay length (pitch) of the layer i, respectively.

X_{pq} is the mutual reactance from layer p to q due to the longitudinal component of the magnetic field, given by

$$X_{pq} = \omega\mu_0\left[\overline{\mu}_r A_s + (A_c - A_s)\right]/\lambda_p\lambda_q \tag{2.13}$$

where A_c is the common internal area between layers p and q, defined as $A_c = \pi R_m^2$, R_m being the layer mean radius. A_s is the area of the steel core and $\overline{\mu}_r$ is the complex relative permeability of the steel, which varies with the intensity of the resulting longitudinal magnetic field in the steel core $\mathbf{H}z$, given by

$$\mathbf{H}z = \mathbf{I}_1/\lambda_1 - \mathbf{I}_2/\lambda_2 + \mathbf{I}_3/\lambda_3 \tag{2.14}$$

Furthermore, the conductor total current I_{total} must be equal to the sum of the current in each layer and the steel core, i.e.,

$$I_{total} = \mathbf{I}_s + \mathbf{I}_1 + \mathbf{I}_2 + \mathbf{I}_3 \tag{2.15}$$

Equations (2.8)-(2.15) are a set of non-linear equations, due to the steel permeability depending on the current. The equation variables are the surface voltage drop $\mathbf{V}$ and the current in each layer. The conductor's AC resistance is calculated from the real part of the surface voltage drop $\mathbf{V}$, obtained by solving the set of equations, as follows

$$R_{ac} = Re\left(\frac{\mathbf{V}}{I_{total}}\right) \tag{2.16}$$

2.4 Methodologies for Transmission Lines Ampacity Calculation

The current carrying capacity (ampacity) of an overhead line is defined so that the heating caused by the current flow (*Joule* heating) along with the other heat exchanges between the conductor and the surrounding environment does not cause it to exceed, in steady state, its maximum allowable temperature, set for safety reasons. The conductor steady-state temperature, in turn, is reached when heat losses are equal to heat gains, as described by the thermal balance equation, given by

$$Q_j + Q_s = P_r + P_c \tag{2.17}$$

where Q_j and Q_s are the heat gains due to *Joule* and solar heating, respectively. P_c and P_r are the heat losses by convection and radiation, respectively.

Using this equation, the conductor steady state temperature can be calculated for a given current and climatic conditions. The equation can also be used to calculate the current so that the conductor reaches a certain steady state temperature for given climatic conditions. The latter consists of calculating the ampacity, where the calculated current is the line current capacity, the temperature is the maximum allowed and the climatic conditions are usually conservative (e.g. low wind speed, high solar radiation).

The *Joule* heat gain Q_j is thus calculated by the maximum allowed current I_{ac} and the AC resistance at the maximum allowed temperature on the conductor surface R_{Tac}, as follows

$$Q_j = {I_{ac}}^2 R_{Tac} \tag{2.18}$$

The terms P_r, P_c, and Q_s depend on the weather conditions. Their calculation method according to CIGRÉ (followed by the Brazilian standard [29]) is described in the Appendix C. Equation (2.18) allows to evaluate the impact of the AC resistance on the ampacity calculation.

From (2.17) and (2.18), we get

$${I_{ac}}^2 R_{Tac} + Q_s = P_r + P_c \tag{2.19}$$

thus,

$$I_{ac} = \sqrt{\frac{P_r + P_c - Q_s}{R_{Tac}}} \tag{2.20}$$

by which the maximum operating current is calculated by the two main used methodologies (IEEE [27] and CIGRÉ [28]) and the current Brazilian methodology [29]. The conductor AC resistance model used in (2.20) to calculate the ampacity, however,

differs for each methodology.

2.4.1 IEEE Methodology

The IEEE methodology for the calculation of overhead conductor ampacity is described in [27]. Its authors propose the use of tabulated values of the conductor AC resistance and the linear adjustment for its surface temperature T, as follows

$$R_{ac}(T) = \frac{R_{ac}(T_{high}) - R_{ac}(T_{low})}{T_{high} - T_{low}} \cdot (T - T_{low}) + R_{ac}(T_{low}) \tag{2.21}$$

where $R_{ac}(T_{high})$ and $R_{ac}(T_{low})$ are the conductor AC resistance at a high temperature T_{high} and a low temperature T_{low}, respectively. In this calculation, T can be up to 25 °C higher than T_{high}.

In addition, for steel-cored conductors with a single aluminum layer, the authors propose the use AC resistance values given in tables from [14] or [50], which include the effect of the core magnetization. In the case of steel-cored conductors with three aluminum layers, it is recommended to apply a multiplier factor k_m from [14] or [25], shown in Fig. 2.10 in section 2.3.1, to the AC resistance tabulated value, adjusted for temperature T, i.e.,

$$R_{Tac} = k_m(I_{ac}) \cdot R_{ac}(T) \tag{2.22}$$

2.4.2 CIGRE Methodology

The methodology for calculating the ampacity of overhead lines is proposed by CIGRÉ in [28]. It is recommended to calculate the conductor AC resistance from its DC value, applying the factor due to the *skin effect* and correction due to its temperature (2.4), as described in section 2.3.1.

In the case of steel-cored conductors with up to three aluminum layers, it is proposed to calculate the ampacity in direct current and convert it to alternating current using empirical formulae, depending on the number of aluminum layers and the conductor cross-sectional area.

The direct current ampacity is calculated assuming that the heat gain in alternating current is the same as in direct current, i.e.,

$$\begin{aligned} Q_{jdc} &= Q_{jac} \\ {I_{dc}}^2 R_{Tdc} &= {I_{ac}}^2 R_{Tac} \end{aligned} \tag{2.23}$$

From (2.19) and (2.23) we have

$${I_{dc}}^2 R_{Tdc} = P_r + P_c - Q_s \tag{2.24}$$

that leads us to the formulation of direct current ampacity, given by

$$I_{dc} = \sqrt{\frac{P_r + P_c - Q_s}{R_{Tdc}}} \tag{2.25}$$

where R_{Tdc} is the DC resistance at the maximum allowed temperature on the conductor surface.

For steel-cored conductors with three aluminum layers, the conversion of the ampacity, from DC to AC, is based on the following I_{ac}/I_{dc} ratio from [51]

$$I_{dc} = I_{ac} \cdot \sqrt{1.0123 + 2.36 \cdot 10^{-5} I_{ac}} \tag{2.26}$$

the DC/AC conversion, in turn, is given by

$$I_{ac} = \frac{I_{dc}}{\sqrt{1.0123 + 2.319 \cdot 10^{-5} I_{dc}}} \tag{2.27}$$

For steel-cored conductors with a single or double aluminum layer, different formulations are proposed for the ampacity conversion, depending on its nominal cross-sectional area. For steel-cored conductors with a single or double aluminum layer and nominal cross-sectional area $A \geq 175$ mm^2, the conversion is given by

$$I_{ac} = \frac{I_{dc}}{\sqrt{1.0045 + 0.09 \cdot 10^{-6} I_{dc}}} \tag{2.28}$$

If the nominal cross-sectional area $A < 175$ mm^2, then, for $I_k = I_{dc}/A$, conversions are proposed for the following cases:

- If $I_k \leq 0.742$, then

$$I_{ac} = I_{dc} \tag{2.29}$$

- If $0.742 < I_k \leq 2.486$, then

$$\begin{aligned} I_{ac} =& I_{dc} / \big[1 + 0.02 \cdot \big(25.62 - 133.9\, I_k + 288.6\, I_k^2 - 334.5\, I_k^3 + 226.5\, I_k^4 \\ & - 89.73\, I_k^5 + 19.31\, I_k^6 - 1.744\, I_k^7\big)\big]^{1/2} \end{aligned} \tag{2.30}$$

- If $2.486 < I_k \leq 3.908$ then

$$\begin{aligned} I_{ac} =& I_{dc} / \big[1 + 0.02 \cdot \big(2.978 - 22.02\, I_k + 24.87\, I_k^2 - 11.64\, I_k^3 + 2.973\, I_k^4 \\ & - 0.4135\, I_k^5 + 0.02445\, I_k^6\big)\big]^{1/2} \end{aligned} \tag{2.31}$$

- If $I_k > 3.908$ then

$$I_{ac} = I_{dc}/\sqrt{1.1} \tag{2.32}$$

2.4.3 ANEEL Methodology

The methodology for calculating the ampacity of overhead transmission lines in Brazil is established by the Brazilian Electricity Regulatory Agency (*Agência Nacional de Energia Elétrica* – ANEEL) in the Normative Resolution 191/2005 [52]. The calculation of the maximum operating current is described in the Technical Note 38/2005 [29] and follows the CIGRÉ methodology.

The calculation of the conductors AC resistance follows the criteria and equations given in section 2.4.2, except for the DC/AC conversion of the ampacity for steel-cored conductors with three aluminum layers, which is given by

$$I_{ac} = \frac{I_{dc}}{\sqrt{1.0123 + 2.36 \cdot 10^{-5}}} \tag{2.33}$$

which corresponds to equation (2.26) of CIGRÉ methodology, without the current I_{ac} in the square root.

2.4.4 Discussion

The conversion of ampacity, from DC to AC, proposed in the CIGRÉ methodology (and followed by ANEEL) is equivalent to applying a factor R_{Tac}/R_{Tdc} to the conductor DC resistance, obtaining its corresponding AC value, as described below.

Consider the conversion factor $f_{ac/dc} = I_{ac}/I_{dc}$, from (2.23):

$$\left(\frac{I_{ac}}{I_{dc}}\right)^2 = \frac{R_{Tdc}}{R_{Tac}} = \frac{1}{R_{Tac}/R_{Tdc}} \tag{2.34}$$

thus,

$$f_{ac/dc} = \frac{I_{ac}}{I_{dc}} = \frac{1}{\sqrt{R_{Tac}/R_{Tdc}}} \tag{2.35}$$

Equation (2.26), in turn, can be rewritten as:

$$\frac{I_{ac}}{I_{dc}} = \frac{1}{\sqrt{1.0123 + 2.36 \cdot 10^{-5} I_{ac}}} \tag{2.36}$$

Note from (2.35) that the terms in the square root in (2.36) represent R_{Tac}/R_{Tdc} and that this resistance ratio varies with the current I_{ac}. Therefore, considering the

ampacity conversion as follows

$$I_{ac} = \frac{1}{\sqrt{R_{ac/dc}(I_{ac})}} \cdot I_{dc} \tag{2.37}$$

where $R_{ac/dc}$ is the ratio R_{Tac}/R_{Tdc} which depends on the current carried by the conductor I_{ac}, from (2.25):

$$\begin{aligned} I_{ac} &= \frac{1}{\sqrt{R_{ac/dc}(I_{ac})}} \cdot \sqrt{\frac{P_r + P_c - Q_s}{R_{Tdc}}} \\ &= \sqrt{\frac{P_r + P_c - Q_s}{R_{ac/dc}(I_{ac}) \cdot R_{Tdc}}} \end{aligned} \tag{2.38}$$

Therefore, the AC resistance is obtained in CIGRÉ methodology by applying to the conductor DC resistance R_{Tdc} (adjusted for temperature T by (2.4)), a factor $R_{ac/dc}$, which covers both the effects due to the *skin effect* and the core magnetization (varying with the current I_{ac}), as follows

$$R_{Tac} = R_{ac/dc}(I_{ac}) \cdot R_{Tdc} \tag{2.39}$$

Indeed, the $R_{ac/dc}$ ratio in (2.26) represents the AC/DC resistance ratio variation of an ACSR "*Zebra*" (54/7) conductor, measured at 50 Hz [51]. The value of 1.0123 in (2.26), according to [28], is the factor due to the *skin effect* while the second term represents the resistance variation with the current I_{ac}, due to the core magnetization. Note that if $R_{ac/dc}$ is divided by the term corresponding to the *skin effect*, a multiplying factor related only to the core magnetization k_m is obtained.

Furthermore, when analyzing $R_{ac/dc}$ in (2.33) of ANEEL methodology, it can be seen that the resistance variation with current was disregarded when the current I_{ac} in the square root term was left out in its formulation. There is thus only a constant factor due to the *skin effect* since the second term (related to the core magnetization) becomes negligible.

The different methods of accounting for the core magnetization effect on the conductor resistance are compared in Fig. 2.12, in which the corresponding multiplier factors k_m of each methodology are depicted. The factors corresponding to CIGRÉ and ANEEL methodologies are obtained by dividing the terms inside the square root in (2.26) and (2.33), respectively, by its factor due to the *skin effect* (1.0123). Results show that the curve corresponding to the CIGRÉ methodology (which represents the "*Zebra*" ACSR conductor) is close to that proposed by [14] for 54/7 stranding conductors, which is the same stranding as the "*Zebra*". In addition, the factor corresponding to ANEEL methodology remains constant, unlike the others multiplier factors.

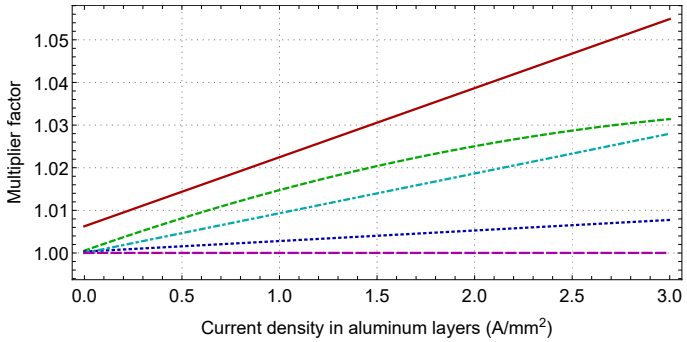

Figure 2.12: Multiplier factors for ACSR conductors with three aluminum layers: corresponding to the methodologies of CIGRÉ (------) [51] and ANEEL (- - - -) [29], and recommended in IEEE methodology from [25] (——), and from [14] for conductors of 54/7 and 54/19 strandings (- - - - -), and 45/7 stranding (·····).

Nevertheless, it must be remembered that by CIGRÉ and ANEEL methodologies, the $R_{ac/dc}$ factor applied to the conductor CC resistance covers both the effect of the core magnetization (shown in Fig. 2.12), as well as the *skin effect* and that the latter corresponds to the value of this effect on a "*Zebra*" conductor at 50 Hz. This, of course, influences the AC resistance value obtained.

To illustrate the difference in results using the resistance calculation of each methodology presented (IEEE, CIGRÉ and ANEEL) and compare them with measured values, the variation of the AC/DC resistance ratio with the current carried of a three-layer ACSR "*Grackle*" conductor, detailed in Appendix A.2, was calculated. Results and values measured in [15] at 20 °C are shown in Fig. 2.13. Results obtained using the *equivalent circuit* model, presented in section 2.3.2, were also included. Calculations following the IEEE methodology and multiplier factors from [14] and [25] are referred to by IEEE-A and IEEE-B, respectively.

Fig. 2.13 shows a better agreement of results obtained using the *equivalent circuit* model with measured values. Results obtained using IEEE-A are slightly conservative while those using IEEE-B are closer to the measured values up to the total current of 1000 A. There is also a greater discrepancy with calculated values using the CIGRÉ and ANEEL methodologies. In the latter, the resistance does not change with the current, remaining at a constant value, close to 1.0123 as already discussed. The discrepancy obtained using the CIGRÉ methodology can be attributed to the correction factor due to the *skin effect* used, which corresponds to that of the "*Zebra*" conductor at 50 Hz and not of the analyzed "*Grackle*" conductor, at 60 Hz. This shows how the formulation proposed by CIGRÉ consists of a specific case only.

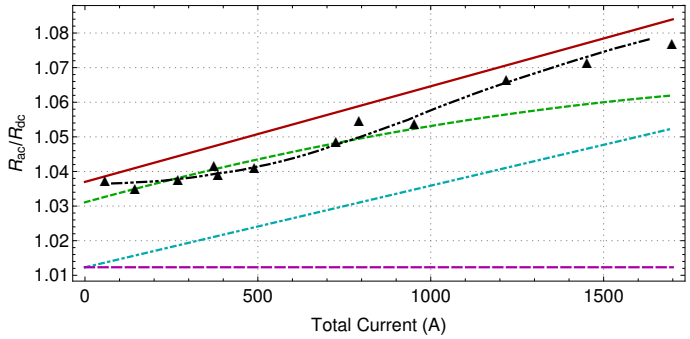

Figure 2.13: Variation of the AC/DC resistance ratio with the total current value of a "*Grackle*" conductor at 20 °C, measured (▲) [15] and calculated using methodologies of CIGRÉ (------), ANEEL (----), IEEE-A (——), IEEE-B (-----) and the equivalent circuit model (-·-·-).

2.4.5 Equivalent-Circuit-Based Proposed Methodology

Given the accuracy of the *equivalent circuit* model in calculating the AC resistance of the ACSR "*Grackle*" conductor observed in Fig. 2.13, the use of this model in calculating the ampacity of this type of conductor should be considered. A methodology for this purpose is described below and is one of the contributions of this thesis.

The method consists, first, in calculating the conductor AC resistance, using the *equivalent circuit* model, for a wide range of current and a given temperature. Fig. 2.13, for example, shows results for the temperature of 20 °C. Then, the resistance values obtained must be represented by an appropriate interpolating function $f_{R_{ac}}$, depending on the value of the total current I_{ac}. This function is used in the thermal balance equation (2.19), as follows

$$f_{R_{ac}}(I_{ac})\, I_{ac}^2 + Q_s - P_r - P_c = 0 \tag{2.40}$$

I_{ac} obtained from the numerical solution of (2.40) is the conductor ampacity.

2.4.6 Application Example

To quantify the effect of using the different resistance calculation models on the ampacity of three-layer ACSR conductors, the ampacity of the "*Grackle*" conductor was calculated. Four operating conditions were considered: maximum conductor temperature of 60 °C and 90 °C, and wind speeds of 0.5 and 1.5 m/s for each temperature. For the four scenarios, it was assumed a solar radiation of 1000 W/m^2, ambient temperature of 30 °C, an average line height of 650 m, a coefficient of emissivity and absorption of the conductor of 0.5.

The conductor AC resistance was calculated using the methodologies of

ANEEL [29], CIGRÉ [28], IEEE with multiplier factors proposed in [25] and [14], referred to as IEEE-A and IEEE-B, respectively, and using the proposed *equivalent circuit* based methodology. Fig. 2.14(a) and Fig. 2.14(b) show the variation of the AC/DC resistance ratio with the total current value calculated for the temperatures of 60 and 90 °C, respectively. Results show that the values calculated using the CIGRÉ methodology become closer to those obtained by the others with increasing temperature. This occurs due to the reduction of the AC/DC resistance ratio with temperature (see Fig. 2.4), accounted for in the calculation of the IEEE methodology and the *equivalent circuit* model, but not by CIGRÉ, whose resistance ratio does not depend on the temperature.

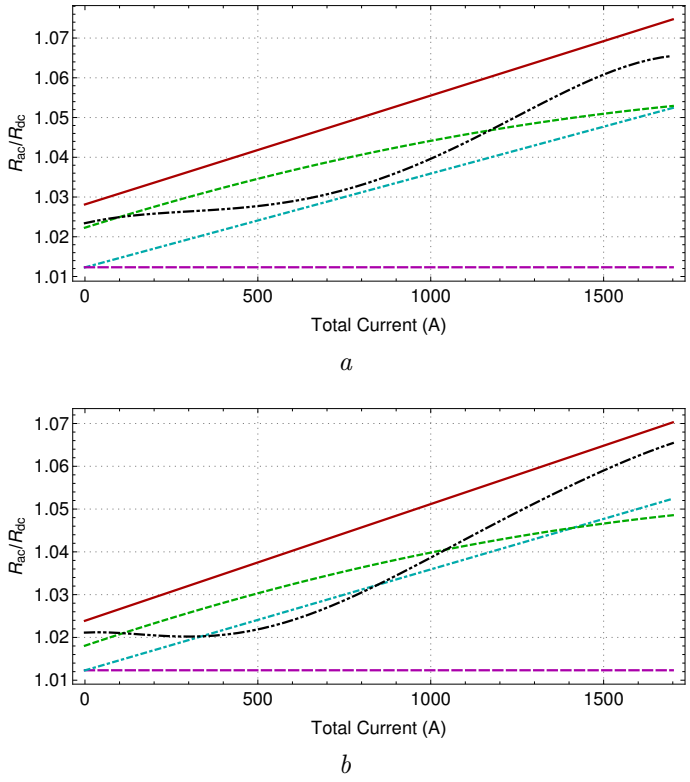

Figure 2.14: Variation of the AC/DC resistance ratio with the total current value of a "*Grackle*" conductor calculated using the methodology of CIGRÉ (------), ANEEL (------), IEEE-A (——), IEEE-B (------) and equivalent circuit model (-·-·-) for the temperature on the conductor surface of 60 °C (*a*) and 90 °C (*b*).

The ampacity results are given in Table 2.1. The deviations of the ampacity calculated by each method in relation to that by ANEEL, i.e., $I_{ANEEL} - I_{Met}$, are given in Table 2.2. Results show that the ampacity calculated according to ANEEL is always higher than that obtained using the other methods. This is easily understood by looking at Fig. 2.14, which shows that the conductor resistance calculated according to ANEEL is always lower than the others. As the *Joule* heating is the same for any of the methods, lower resistance values lead to higher currents. It is important to note that for a higher temperature and wind speed there is a

greater discrepancy between the result obtained using ANEEL methodology and the others. In these cases, the conductor can carry higher current values, either due to the greater cooling by convection or the higher allowed temperature, for which there is a greater discrepancy between the AC/DC resistance ratio calculated using ANEEL methodology and the others.

Table 2.1: Calculated ampacity for the different scenarios

T(°C)	v (m/s)	Ampacity (A)				
		ANEEL	CIGRÉ	IEEE-A	IEEE-B	Eq. Circuit
60	0.5	729.7	723.6	717.2	720.2	723.0
	1.5	982.5	971.5	962.6	967.7	970.0
90	0.5	1142.6	1127.8	1119.5	1124.7	1125.1
	1.5	1440.9	1417.6	1406.7	1417.8	1409.9

Table 2.2: Deviation of ampacity for different scenarios

T (°C)	v (m/s)	Deviation of ampacity (A)			
		CIGRÉ	IEEE-A	IEEE-B	Eq. Circuit
60	0.5	6.1	12.4	9.5	6.7
	1.5	10.9	19.8	14.8	12.4
90	0.5	14.7	23.0	16.3	17.9
	1.5	23.3	34.2	23.2	31.0

Furthermore, results show that the resistance calculation proposed in the CIGRÉ methodology is not at all appropriate, as it corresponds to a specific case ("*Zebra*" conductor at 50 Hz), and does not account for variations in the resistance ratio with temperature. The calculation according to ANEEL methodology (which follows CIGRÉ) is even more inappropriate, since it also does not represent the increase in resistance with the current, due to an error in its formulation (identified in section 2.4.4). This leads to a great risk of overestimating the line's ampacity and the conductor overheating. The IEEE methodology, therefore, is more appropriate, while the use of the multiplier factor from [25] is more conservative than that from [14].

The use of the equivalent circuit model, in turn, stands out as the best option, since it considers the various aspects that affect the core magnetization of these conductors, such as frequency, temperature, and mechanical stress. However,

its use is subject to a deeper knowledge of the conductor characteristics and its steel core. Some aspects about the magnetization of the steel core at high currents/temperatures and its representation using the equivalent circuit are not yet found in the literature and are addressed in the following chapters.

Chapter 3

Experimental Studies

3.1 Introduction

This chapter presents the experimental studies on the magnetic properties of an ACSR conductor steel core and on the transformer effect in the same conductor. All laboratory work was performed at the Electrical Energy Research Center (CEPEL) Laboratories - *Electrical and Magnetic Properties Laboratory* and *High Current Laboratory*.

3.2 Study on the Magnetic Properties of the Steel Core

This section presents the experimental study carried out on the steel core of a "*Duck*" conductor up to a temperature of 230 °C. The magnetic properties of these type of steel are known up to 150 °C [33], which even exceeds the maximum emergency overload temperatures of conventional conductors. However, steel-cored conductors with annealed aluminum wires may operate at a temperature up to 200 °C [34] and therefore the magnetic properties in this higher temperature range need to be further investigated to study the effects of the core magnetization on these conductors.

3.2.1 Experimental Procedure

The measurements were made on two galvanized steel wires of 220 mm length and 2.68 mm diameter taken from the steel core of the ACSR "*Duck*" conductor described in Appendix A.1. A pair of spools made of polyester with fiberglass, as shown in Fig. 3.1, was built for the experiment. On each coil were coaxially wound a magnetizing coil of 150 turns and a search coil of 10 turns, both of enameled-copper

wires.

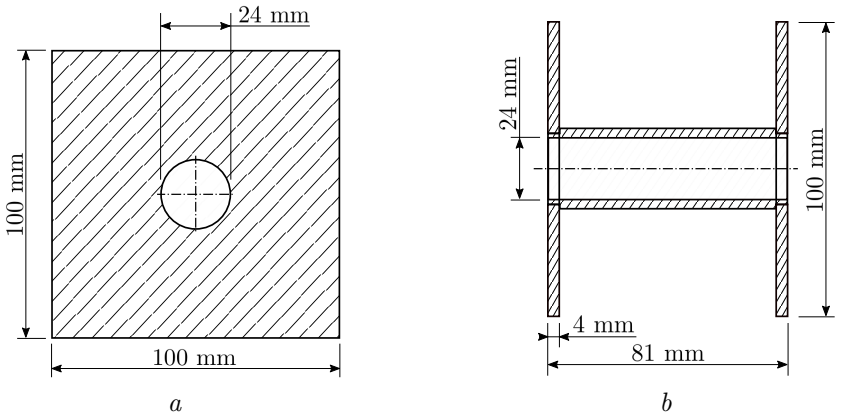

Figure 3.1: Spool built for the experiment - Side view (a) and front view (b).

The steel wires were placed inside one of the spools and their ends were compressed between two U-shaped laminated silicon steel cores, as shown in Fig. 3.2. The arrangement sets a magnetic circuit with 81 mm length of the steel wires and two parallel magnetic paths formed by the U-shaped cores. As the area of the U-shaped steel core is much larger than that of the steel wires, its reluctance may be neglected and the length of the steel wires within the coil (81 mm) may be considered as the effective length of the magnetic circuit.

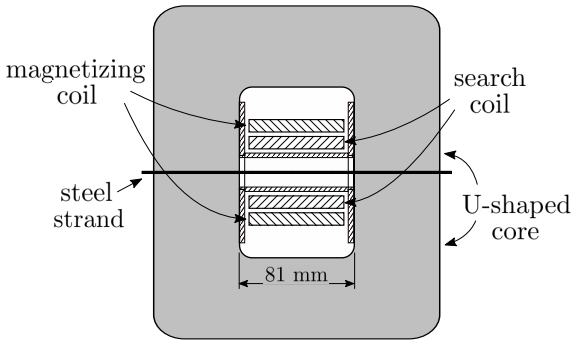

Figure 3.2: Arrangement of the magnetic circuit.

To compensate for the air gap between the search coil and the steel wires, another similar arrangement was build using two aluminum wires of the same diameter of the steel wires. The magnetizing coils of both arrangements were connected in series and supplied with sinusoidal currents at 60 Hz from a double Variac and a mercury switch. The search coils were connected in series, in opposite directions, in order to subtract the voltage induced by the magnetic flux in the air gap between the steel wires and the search coil. The resulting voltage from the search coil was supplied to an analog integrator to obtain the magnetic induction, which was recorded on a digital oscilloscope along with the magnetizing current.

The arrangement with the steel wires was placed inside a controlled ambient chamber, whose temperature ranged from 40 to 230 °C, at intervals of 10 °C. Measurements were made for a wide range of magnetizing current at each temperature in the controlled ambient chamber.

The magnetic field strength H is calculated from the magnetizing current I_m as follows:

$$H = N_m I_m / \ell \tag{3.1}$$

where N_m is the number of turns of the magnetizing coil and ℓ is the magnetic path length.

The magnetic induction B, obtained by an analog integrator, is calculated by integrating the search coil voltage v divided by its number of turns N_s and the cross-section area of the steel wires A, as follows

$$B = \frac{1}{N_s A} \int v(t)\, dt \tag{3.2}$$

The complex permeability modulus μ is found from the ratio of the peak values of B and H. The relative permeability module, in turn, is $\mu_r = \mu/\mu_0$ where μ_0 is the magnetic permeability of free space.

The hysteretic angle δ, which is the complex permeability argument, is calculated from (2.2), i.e. $\delta = \arcsin \frac{A_{ellipse}}{\pi B_p H_p}$, where $A_{ellipse}$ is the area of the measured $B - H$ loop [46–48], H_p and B_p are the peak value of the magnetic field strength and induction, respectively.

3.2.2 Results and Discussion

Relative permeability and power losses

The modulus of the complex relative permeability measured for different magnetic field strength and temperatures is shown in Fig. 3.3 and Fig. 3.4. Fig. 3.3a shows the variation with magnetic field strength with their maximum heavily influenced by the temperature. The maximum permeability value for each temperature is depicted in Fig. 3.3b.

As plotted results show, that maximum value occurs at decreasing values of magnetic field strength, for temperatures up to 130 °C. This has been reported in literature [22]. However, a different behavior is found in results for temperatures above 160 °C. This change of behavior implies that, well below the Curie temperature, a maximum value of the magnetic permeability exists, for a specific range of the magnetic field strength. This is shown in Fig. 3.4 where the variation of the relative permeability with temperature for different magnetic field values is plotted, showing a hump shape for magnetic field strength ranging from 1.0 to 2.4 kA/m.

Furthermore, the temperature at which the permeability reaches its maximum value depends on the magnetic field strength, occurring at increasing temperatures, ranging from 150 °C to 170 °C, with increasing magnetic field strength. It should be noticed that these maximum permeability values are found far below the steel Curie temperature, which is above 700 °C and at which the permeability was only expected to reach its maximum value. At the Curie temperature, magnetic materials lose their magnetic properties, causing their permeability to decrease sharply.

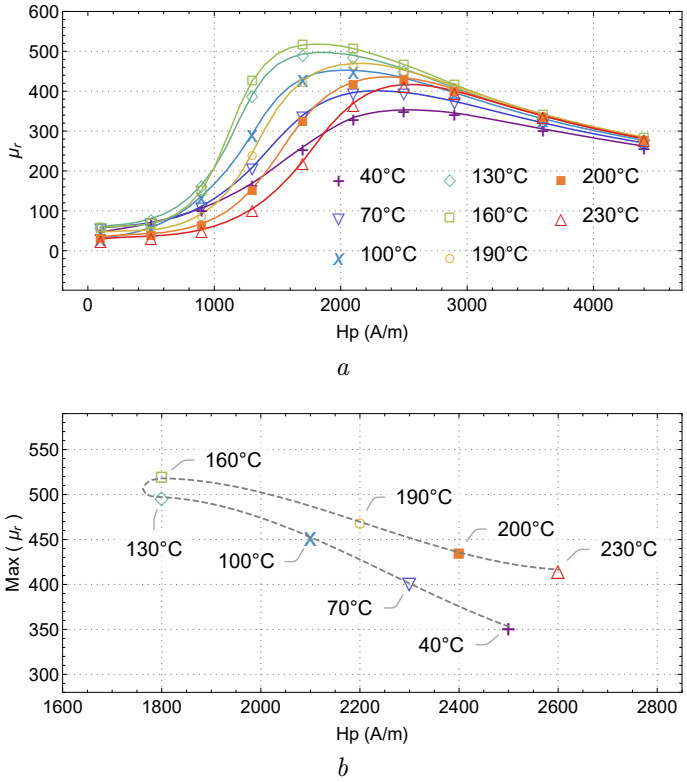

Figure 3.3: Variation of the relative permeability modulus (μ_r) with magnetic field strength for different temperature values (a) and respective maximum values (b), showing their ascending and descending behavior.

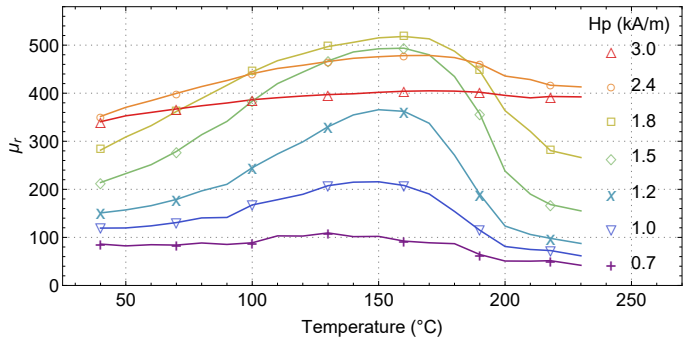

Figure 3.4: Variation of the relative permeability modulus (μ_r) with temperature for different magnetic field strength.

The existence of a maximum permeability value below Curie temperature for the

steel used in conductor cores was never reported. However, previous measurements were carried out up to 150 °C [33], thus slightly bellow the temperature at which these maxima are found.

The existence of a maximum permeability value below Curie temperature is also found in other magnetic materials such as many ferrites, occurring mainly at the temperature that the crystal anisotropy goes through zero [53, 54]. This secondary permeability maximum (SPM) depends on the chemical composition of the material and coincides with a minimum power loss [55, 56]. In order to check if similar conclusion can be drawn for the tested steel, the power losses were calculated considering the hysteresis loop area, for different values of induction and temperature. Results in Fig. 3.5 depict power losses as a function of induction for several temperature values, showing the same type of behavior as reported in literature for ferrites. In the case of the tested steel, the loss curves move down for temperatures up to 130 °C and then up from 160 to 230 °C. As already mentioned, only the behavior up to 130 °C was already known [32], thus the analysis of the behavior at higher temperatures represents an important contribution of this work. The temperature at which the losses reach their minimum, for different induction values, can be seen in Fig.3.5b and corresponds to the temperature range in which the SPM is found, i.e., from 150 to 170 °C – see in Fig. 3.4.

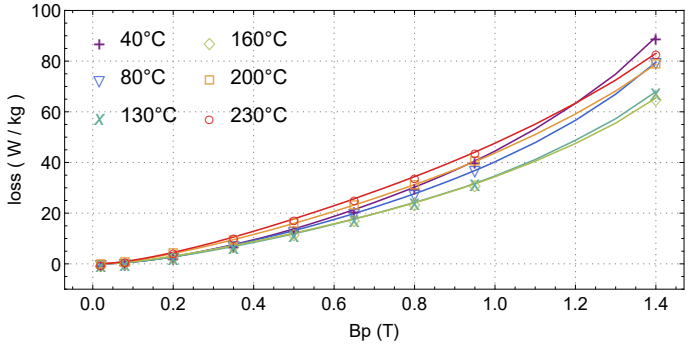

a

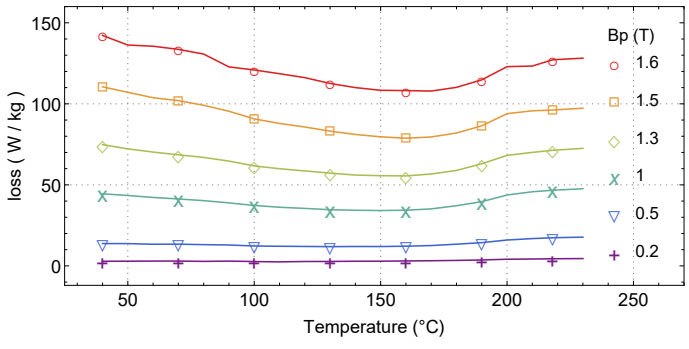

b

Figure 3.5: Variation of power losses with induction for different temperature values (a) and with temperature for different induction values (b).

The observed permeability variation will certainly influence the transformer effect in ACSR conductors, which has been experimentally studied up temperatures around 130 °C [24]. A study on the transformer effect for higher temperatures is presented in section 3.3, based on experimental results obtained for a "*Duck*" conductor.

Hysteretic angle, loss tangent and complex relative permeability

These quantities, which are related to material power losses, were computed from experimental results, according to eq. (2.1) and (2.2). Fig. 3.6 shows the variation of the hysteretic angle, δ, with magnetic field strength, for different temperatures. The variation of the corresponding loss tangent, $\tan(\delta)$, is shown in Fig. 3.7. The real and imaginary parts of the complex relative permeability are shown in Fig. 3.8, for different magnetic field strength and temperature. In all figures, two distinct behaviors of the magnetic characteristic with increasing temperature are observed: one behavior up to 130 °C and another above 160 °C, as observed in the permeability modulus. All obtained results up to 130 °C are similar to those reported in [22], which were carried out on a steel core taken from an ACSR "*Grackle*" conductor at temperatures up to 120 °C. The behavior found at temperatures above 160 °C is, therefore, a novel contribution of this work.

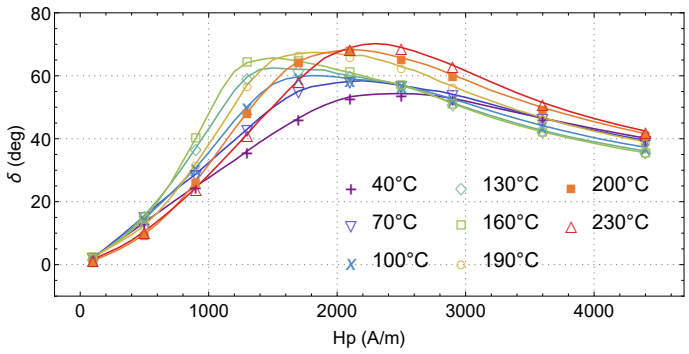

Figure 3.6: Variation of hysteretic angle δ with magnetic field for different values of temperature.

3.3 Study on the Transformer Effect in an ACSR Conductor

This section presents the experimental study carried out on an ACSR "*Duck*" conductor in which the current in each of its 54 aluminum wires was measured for different total current values and during the conductor heating. Previously, only the current density on the surface of a randomly selected wire from each aluminum layer

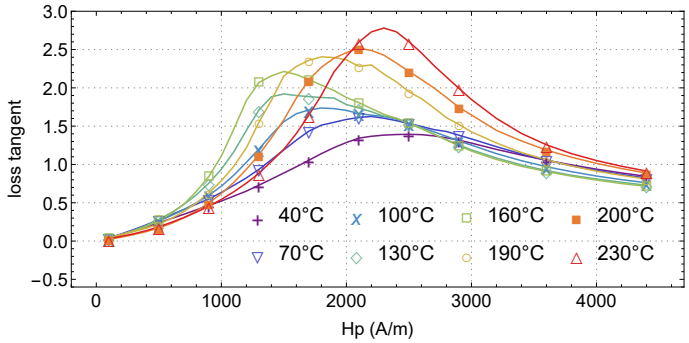

Figure 3.7: Variation of loss tangent with magnetic field strength for different values of temperature.

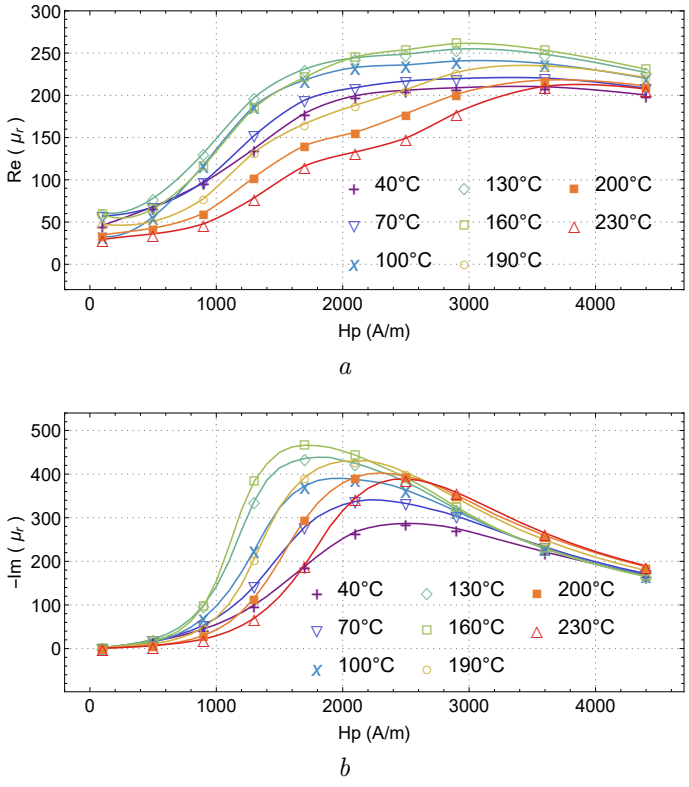

Figure 3.8: Variation of the complex relative permeability with magnetic field strength for different values of temperature - Real part (a) and Imaginary part (b).

of an ACSR conductor was measured for the analysis of the current redistribution caused by the core magnetization (transformer effect) and the conductor heating was avoided [15]. The effect of increasing the temperature on the steel core was only calculated at [17]. In this study, currents up to 6 kA were supplied to the conductor, so that a wide range of temperature and magnetic field strength was reached in the core.

3.3.1 Experimental Procedure

The conductor sample used in the experiment was an ACSR code-named "*Duck*", with nominal aluminum area of 306.9 mm^2 and 21 m length. The conductor has 54 aluminum wires in three layers over a galvanized steel core of 7 wires. Both aluminum and steel wires are 2.68 mm diameter. Further details of the conductor are given in Appendix A.1.

Six tubular profile spacer structures, made of phenolic paper, were built so that the current in each aluminum wire of the conductor sample could be measured individually. A pair of spacers was designed for each layer of aluminum with a number of holes equal to the number of layer wires and so that the spacer could be attached to the spacers of the adjacent layers. Fig. 3.9(a) shows the front view of the spacer structures of each layer with its outer diameter. The side view with the assembly scheme is shown in Fig. 3.9(b).

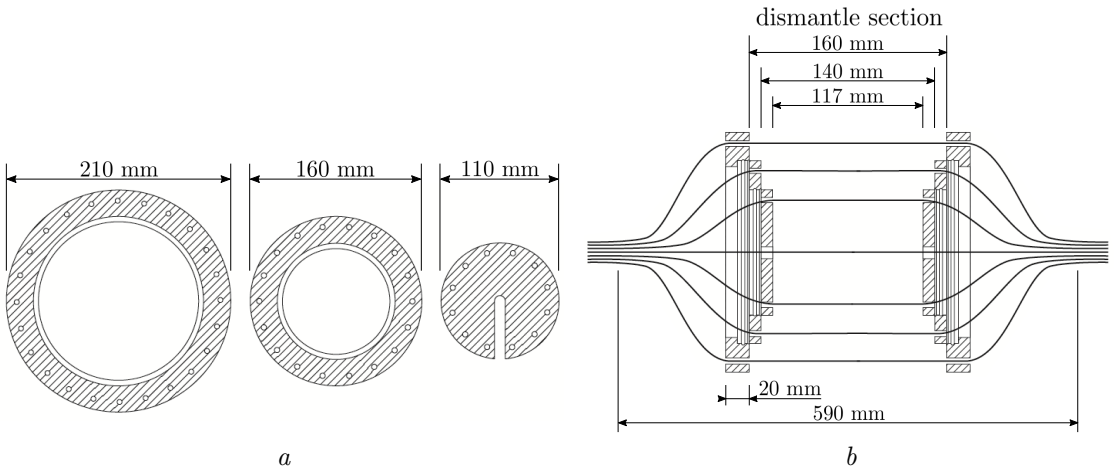

Figure 3.9: Spacer structures assembly scheme - Front view (a) and Side view (b).

For the spacer structures installation, the 54 aluminum wires were carefully cut at the mid-length of the conductor sample and manually unwrapped only in the region where the spacer structures were installed. The remainder of the conductor was kept undisturbed. After placing the spacers, each aluminum wire was inserted into a hole of the spacer structures and labeled for identification of measured quantities. Tubular profile window-type current transformers (CT) of 25 mm outer diameter were installed on each conductor wire in the conductor dismantle section. The measurement uncertainty of the CT is below 2%. Gas tungsten arc welding (GTAW) was used to reconnect the conductor wires. The welding process was previously tested on the same material and no changes were observed in the electrical resistance of the conductor wires. The length variation of each wire after the installation of the spacer structures was below 1.5%.

A 10.4 m conductor span was tensioned, as shown in Fig. 3.10 and Fig. 3.11, in the indoor *High Current Laboratory*. Six J-type thermocouples, insulated with Teflon, named Tc1 to Tc6, were attached to the surface of the conductor along the span, using thermal paste to improve their contact to the conductor. The thermocouples were calibrated before measurements and the resulting uncertainties were below 0.1%. Three tinned copper search coils of 100 turns, made of 22 AWG tinned copper wires, named from Sc1 to Sc3, were wrapped around the conductor along its length to measure the internal longitudinal magnetic flux. A window-type current transformer, calibrated with magnitude accuracy of 0.3%, and a dynamometer were used to measure the total current and mechanical tension, respectively.

The conductor was supplied with currents at 60 Hz and root mean square (RMS) value ranging from 600 A to 6000 A, from a system consisting of transformers and a reactors bank, connected to a 138 kV transmission line. Each current was supplied to the conductor at ambient room temperature (about 23 °C) and held approximately constant (±0.9 %), by means of transformer tap changes, until the measured temperatures became steady or reached 200 °C. The conductor sample was tensioned

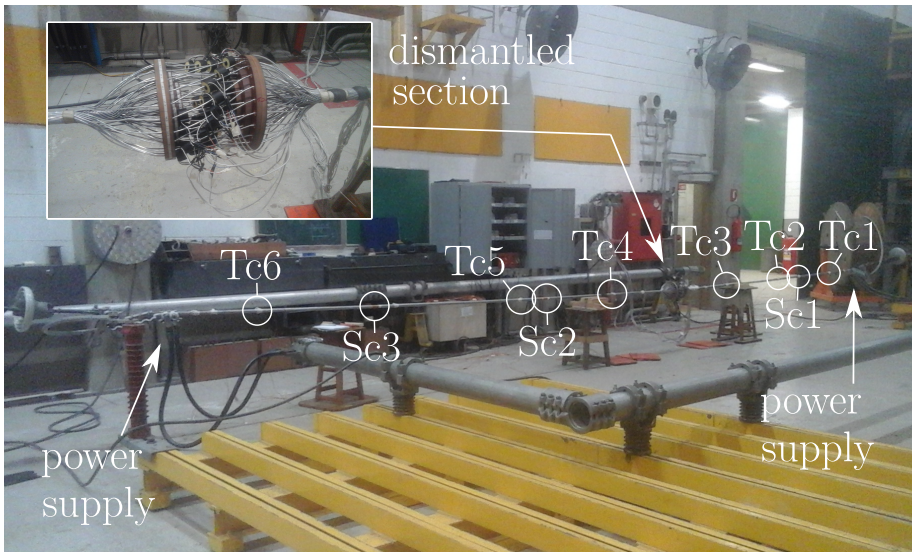

Figure 3.10: Arrangement of the ACSR "*Duck*" conductor (Tc: Thermocouple, Sc: Search Coil).

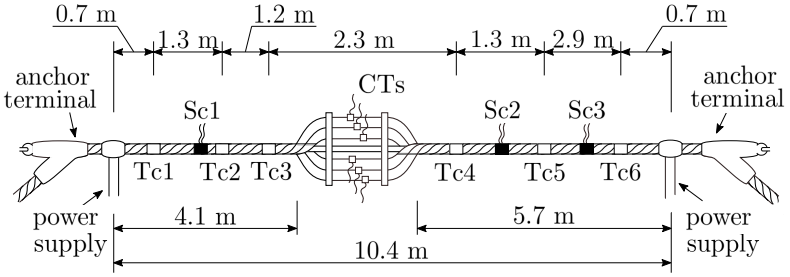

Figure 3.11: Arrangement of the ACSR "*Duck*" conductor - schematic illustration.

by means of hydraulic cylinders at 300 kgf.

A digital system of signal conditioning, acquisition and storing, called IMA-DP [57, 58], was used to record and monitor all the current measurements and voltage at the search coils. The system, developed at CEPEL using the PXI platform, is intended for the monitoring and analysis of partial discharges in high voltage equipment and was adapted for this experiment. Samples of 9 cycles of the waveform were recorded every 30 seconds and the root mean square (RMS), maximum, minimum and mean values of all currents and coil voltages were recorded every 5 seconds. A second digital system was used for the recording and monitoring of temperature measurements with storage intervals of 7 seconds. Both systems were about 3 m away from the experimental arrangement, in a separated location, and every conductive object was at least 1.7 m away from the energized part of the conductor sample.

3.3.2 Results and Discussion

Temperature measurements

The current being held approximately constant, the temperature on the conductor surface was measured by 6 different thermocouples along the conductor sample. Fig. 3.12 shows the measured values along time for different total current values. Note that the time frames in Fig. 3.12 are different.

For currents up to 1100 A, the steady-state temperature was below 200 °C, increasing with the total current value. For higher current the temperature exceeded 200 °C and the power supply was turned off. It is also observed that the temperature along the conductor sample is not uniform, due to non-uniform heat dissipation effect. The thermocouples installed near the ends of the tested conductor section (Tc1 and Tc6, see Fig. 3.12) show the lowest temperatures, due to it being connected to the non-energized sections of the conductor sample. The temperature measured by the central thermocouples (Tc3 and Tc4) is slightly affected, due to the effect of the spacers.

The conductor temperature will be defined by the average of the values measured by the thermocouples Tc2 to Tc5, which are less affected by non-uniform heat dissipation. The chosen representative times (initial t_i and final t_f) are indicated in Fig. 3.12. For total currents from 1000 to 2300 A, an intermediate time (t_m) is also indicated, at which a maximum magnetic flux value was found.

Longitudinal magnetic flux measurements

The axial magnetic flux is calculated by integrating the measured search coil voltage divided by its number of turns N_s. Fig. 3.13 presents the variation of the

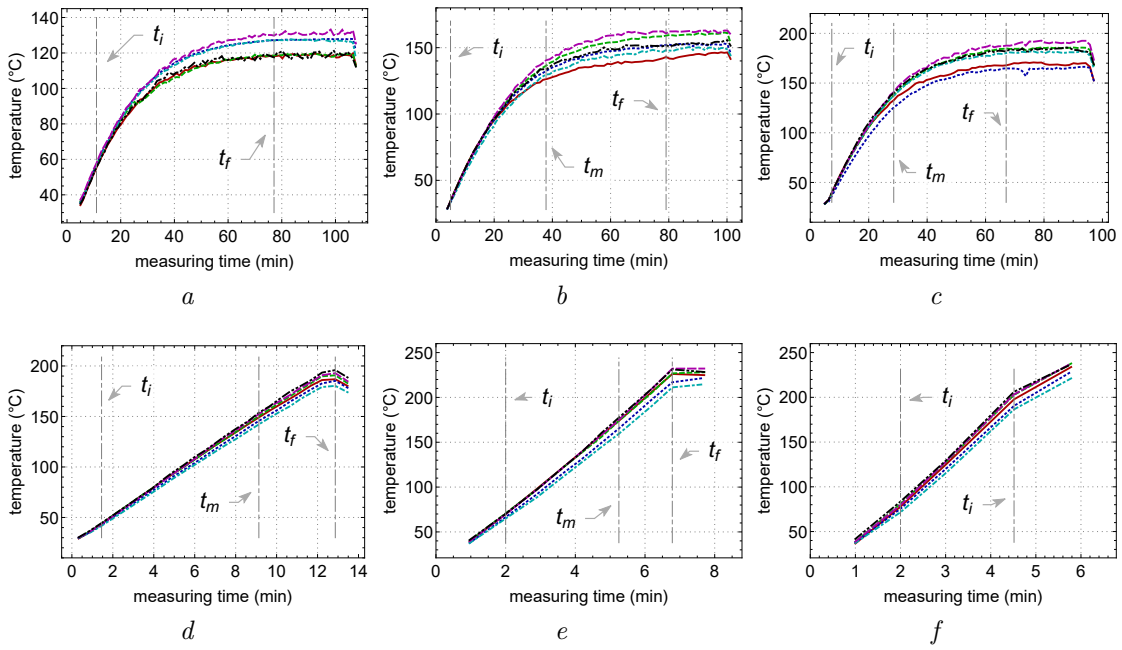

Figure 3.12: Variation of the temperature on the conductor surface along time, measured by thermocouples Tc1 (——), Tc2 (- - - -), Tc3 (·····), Tc4 (-·-·-), Tc5 (– – –) and Tc6 (–·–·–), with total current values of 900 A (a), 1000 A (b), 1100 A (c), 1600 A (d), 2300 A (e) and 2700 A (f).

RMS value of the axial magnetic flux along time, corresponding to each coil, for the six total current values. The difference between the values measured by the three search coils can be attributed to the temperature variation in the conductor along the span, measured by the thermocouples (see Fig. 3.11), higher flux values corresponding to higher temperatures.

For the different total current values, results in Fig. 3.13 show two distinct behaviors of the magnetic flux along time and thus during the conductor heating process. For total current values bellow 1000 A, the magnetic flux continuously increases with temperature. However, from 1000 A up to 2300 A, the magnetic flux along time presents a hump shape, i.e., it increases with temperature, reaches a maximum value at the intermediate time (t_m), marked in Fig. 3.13 with a vertical line, and then decreases. Fig. 3.12 shows that the conductor surface temperature measured at t_m increases with increasing total current value and therefore with increasing magnetic field strength in the core, such as that observed in the variation of permeability with temperature in section 3.2 (see Fig. 3.4). The temperature on the conductor surface at t_m ranges from 134 °C to 168 °C, while the maximum permeability value of the steel core was found at temperatures from 150 °C to 170 °C. It should be noticed that the temperature in the steel core may be higher than that on the conductor surface, depending on the conductor radial temperature gradient, which is relevant for current densities greater than 1 A/mm^2 [27].

For total current higher than 2.3 kA, the magnetic flux maximum value with respect to the increasing temperature no longer exists, meaning that the permeability monotonically increases so the strength of the magnetic field in the core must be above 2.4 kA/m (see Fig. 3.4).

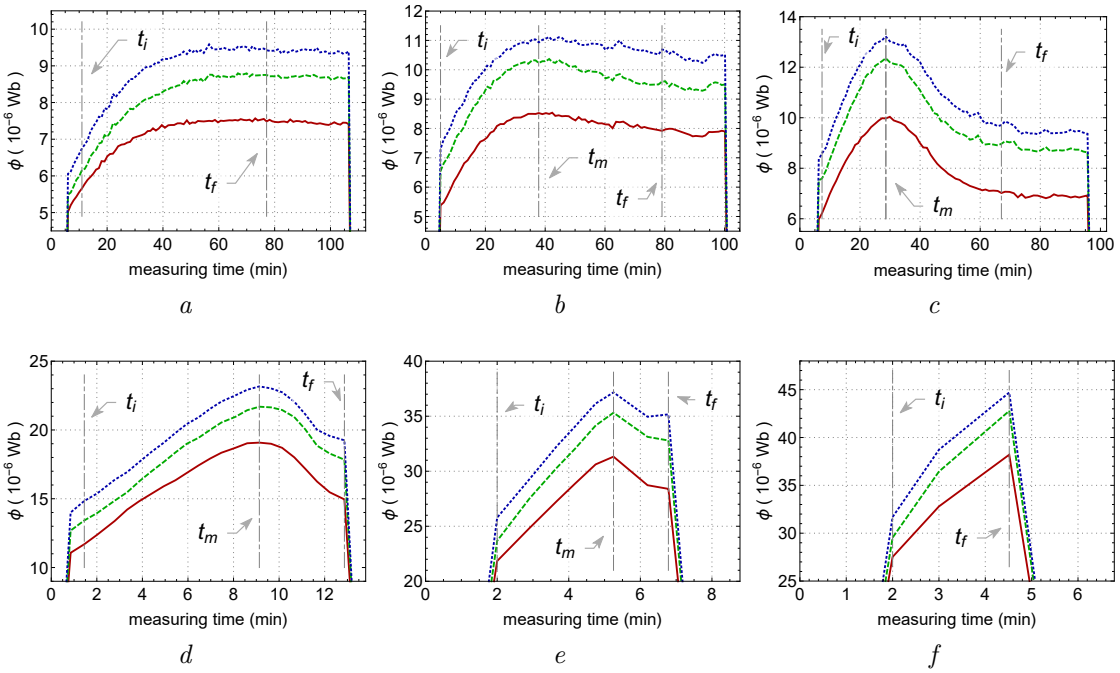

Figure 3.13: Variation of the axial magnetic flux along time, measured by search coil Sc1 (——), Sc2 (- - - -) and Sc3 (·····), with total current values of 900 A (*a*), 1000 A (*b*), 1100 A (*c*), 1600 A (*d*), 2300 A (*e*) and 2700 A (*f*).

Current density measurements

The RMS value of the current in each aluminum wire was registered every 5 seconds, using the 54 CT installed in the conductor cross-section (see Fig. 3.11), and the corresponding current density calculated, considering their cross-section value (5.64 mm^2). As an example, Fig. 3.14 shows the steady-state results for a total current of 900 A, the conductor temperature being 125.54 °C. The conductors numbered from 1 to 12 belong to the inner layer, those numbered from 13 to 30 (18 conductors) belong to the middle layer and those numbered from 31 to 54 (24 conductors) belong to the outer layer. Results show a higher current density in the middle layer caused by the transformer effect, as pointed out in [32, 59, 60], and measured in [15]. The variation of the current density among conductors of the same layer is highlighted in Fig. 3.14(b) and in Fig. 3.15, this offering a three-dimensional view, where the current distribution between layers is also clear. It must be mentioned that the measurement of the current density distribution between conductors of the same layer

had not been reported in the literature and, therefore, is one of the contributions of this work.

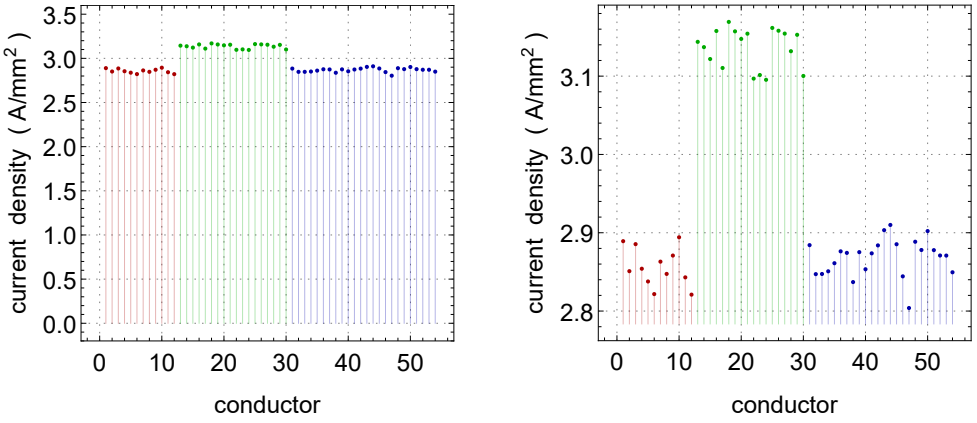

Figure 3.14: Distribution of current density among aluminum wires of inner (•), middle (•) and outer (•) layer measured for the total current of 900 A at 125.54 °C conductor temperature (a) - in detail (b).

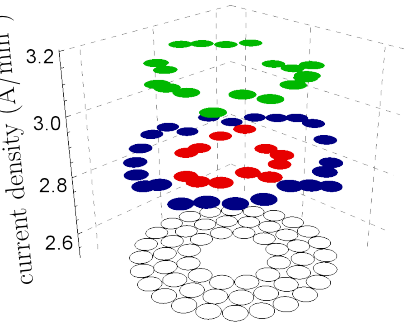

Figure 3.15: Cross-section of the conductor with the current density distribution among conductors of inner (•), middle (•) and outer (•) layer measured for the total current of 900 A at 125.54 °C conductor temperature.

It was verified, in all experimental results, that the current density variation among conductors in the same layer remains small, no matter the total current value and time/temperature. Fig. 3.16 shows the variations observed in the inner layer (conductors 1 – 12), for the three total current values at which the steady-state was reached (900, 1000 and 1100 A). The represented values were registered at the initial and final times, the corresponding conductor temperature being indicated in the graphics. In all cases, the standard deviation represents less than 1.5% of the mean value.

The current density in each aluminum layer was then calculated as the mean value of the current density in its wires. The variation along time of the current

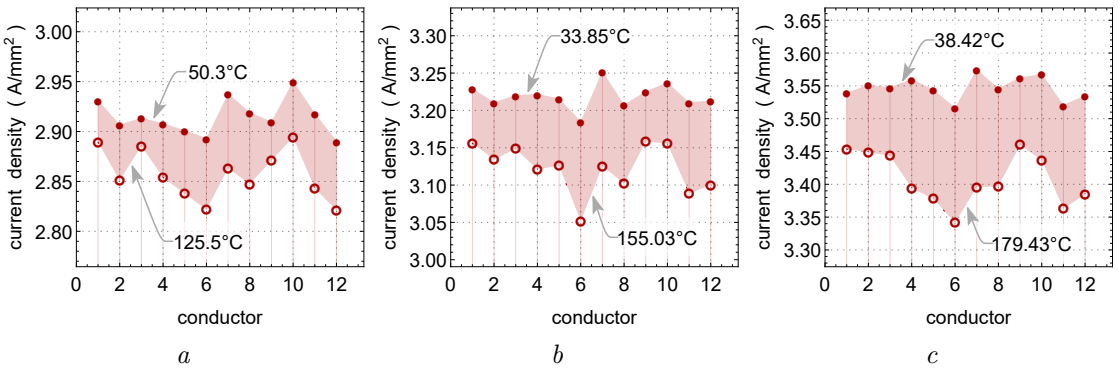

Figure 3.16: Effect of temperature on the current density distribution among conductors in the inner layer for initial (•) and final (◦) representative times, measured for total current values of 900 A (a), 1000 A (b) and 1100 A (c).

density in each aluminum layer and the mean value in the three layers were computed for a large range of total current values (up to 6 kA). Fig. 3.17 depicts results for the six total current values considered in Fig. 3.12 and Fig. 3.13. The mean value in all aluminum layers is also shown as it represents the variation of the total current value during the experiment. These variations are due to the increase of the electrical resistance with temperature and the variations of the power supply voltage, which although being corrected during the experiment by the tap changes of the supply transformers, could not be completely eliminated. This information is important, so that the variation of the current density distribution along time and thus with temperature, is correctly interpreted. The current density in each layer, the magnetic flux measured by each search coil and the corresponding temperature on the conductor surface for the 6 total current values and for the representative times (t_i, t_m and t_f) are given in Table 3.1. The variation of magnetic flux and current density in each interval is given in Table 3.2.

Results show that the current density distribution is affected by the transformer effect: a concentration of the current density in the middle layer, which increases with the intensity of the current carried by the conductor. In the total current range in which the magnetic flux variation with temperature presents a hump shape (from 1000 to 2300 A), the current density in the middle layer tends to decrease with increasing conductor temperature after the flux reaches its maximum value at t_m (see Table 3.2) and thus with the magnetic flux decrease, as a result of the transformer effect weakening. These results demonstrate the effect of the newly found permeability variation with temperature, reported in section 3.2, on the transformer effect.

For total current values from 2700 to 6000 A, the current density in the middle layer continuously decreases with increasing conductor temperature. This variation, observed at short intervals due to the quick conductor heating, occurs despite a

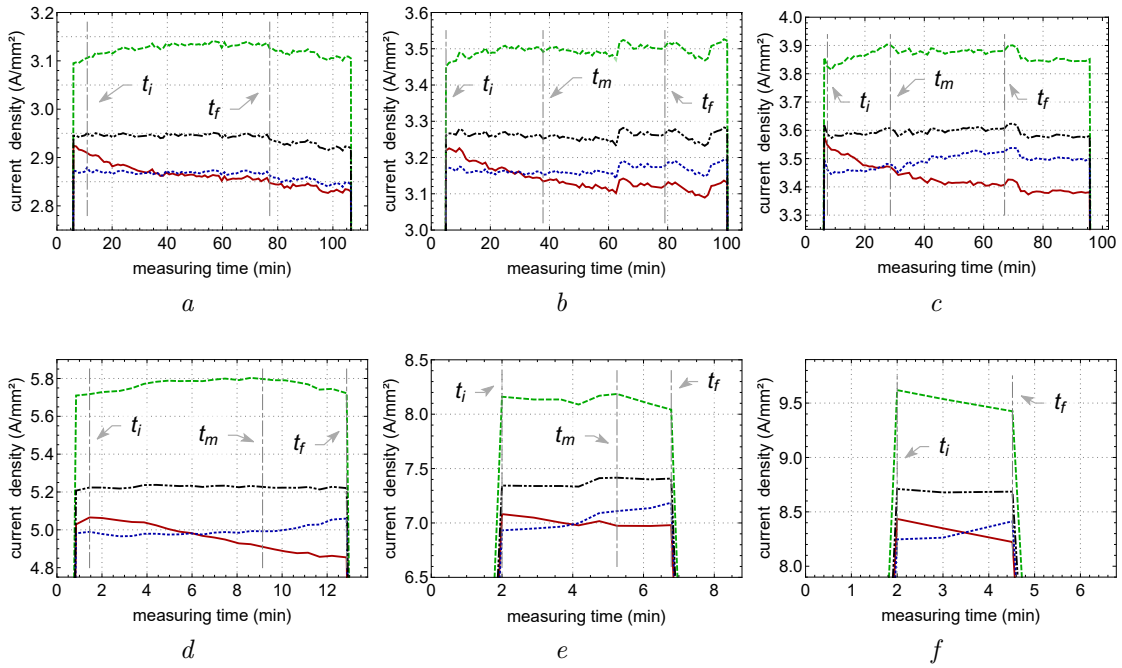

Figure 3.17: Variation of current density along time in the inner (——), middle (- - - -) and outer (·····) layers of aluminum wires, and the mean value in the three layers (-·-·-), with total current values of 900 A (a), 1000 A (b), 1100 A (c), 1600 A (d), 2300 A (e) and 2700 A (f).

constant increase in magnetic flux and can be explained by the transient internal conductor temperature, in which the highest temperatures are found in the layers with higher current density [19–21]. Indeed, the heating of the layer increases the electrical resistance of its wires and thus decreases the current density.

Further to the concentration of current density in the middle layer, a current redistribution between the inner and outer layers is also observed with increasing conductor temperature. This current redistribution, which varies with the total current value, does not correspond to the effect of the conductor heating calculated in [17]. In addition, such measurement hadn't yet been reported in the literature, thus requiring in-depth analysis.

3.3.3 Analysis of the Transformer Effect

The intensity of the transformer effect depends on the longitudinal magnetic flux in the steel core, hence on the *total current value* and the steel core *magnetic properties*, which vary with the *temperature* and *mechanical tension* [22]. The experimental results show the increase in current redistribution caused by the transformer effect with the total current value, by increasing the core magnetization (see the magnetic fluxes at the initial time of each total current in Table 3.1). The effect of the steel core temperature on the transformer effect was previously calculated by

Table 3.1: Conductor surface temperature, axial magnetic flux and current density in each aluminum layer for different values of total current and representative times.

Total current (A)	Conductor surface temperature (°C)	Magnetic flux (10^{-6} Wb)			Current density (A/mm^2)		
		Search coil			Layer		
		Sc1	Sc2	Sc3	Inner	Middle	Outer
900	50.32	5.43	5.89	6.45	2.915	3.100	2.869
	125.54	7.57	8.74	9.47	2.857	3.136	2.869
1000	33.85	5.38	6.55	7.30	3.219	3.451	3.172
	134.38	8.49	10.30	11.01	3.139	3.500	3.157
	155.03	7.92	9.59	10.69	3.122	3.506	3.177
1100	38.42	6.22	7.59	8.59	3.547	3.825	3.461
	135.27	9.97	12.35	13.22	3.470	3.901	3.479
	179.43	7.02	8.97	9.71	3.408	3.883	3.524
1600	42.97	11.70	13.42	14.84	5.065	5.717	4.984
	147.64	19.08	21.69	23.17	4.910	5.797	4.992
	187.29	14.95	17.84	19.25	4.854	5.722	5.059
2300	67.99	21.84	23.68	25.79	7.081	8.160	6.932
	168.43	31.32	35.32	37.16	6.974	8.186	7.109
	221.76	28.40	32.79	35.17	6.980	8.042	7.186
2700	76.90	27.52	29.54	31.69	8.435	9.619	8.247
	195.75	38.20	42.78	44.70	8.223	9.425	8.413

Morgan [17], but never confirmed by experimental results. According to Morgan's results, reproduced in Fig. 3.18, it would be expected that a consistent increase of the current redistribution between layers would occur, resulting in an increase of the current density in the middle layer and a decrease in the inner and outer layers. Morgan's calculations consider only the increase in the steel permeability with temperature and, consequently, the strengthening of the transformer effect. However, in the intervals where the measured magnetic flux increases with temperature (see Table 3.2), only a decrease in current density in the outer layer was observed for the total current of 1000 A. The increase in current density in this layer is observed in the other intervals, for currents higher than 1000 A. This can be explained by the existence of a radial temperature gradient, which is relevant for higher currents, and was not included in Morgan's computational study.

Table 3.2: Variation of the axial magnetic flux and current density in each layer during intervals.

Total Current (A)	Interval	Variation of Magnetic flux (10^{-6} Wb)			Variation of current density (A/mm^2)		
		Search coil			Layer		
		Sc1	Sc2	Sc3	Inner	Middle	Outer
900	$[t_i, t_f]$	2.14	2.85	3.01	-0.058	0.036	0.000
1000	$[t_i, t_m]$	3.11	3.78	3.71	-0.080	0.049	-0.015
	$[t_m, t_f]$	-0.57	-0.74	-0.32	-0.017	0.006	0.020
1100	$[t_i, t_m]$	3.75	4.76	4.63	-0.077	0.076	0.018
	$[t_m, t_f]$	-2.95	-3.38	-3.51	-0.062	-0.018	0.045
1600	$[t_i, t_m]$	7.38	8.27	8.33	-0.155	0.080	0.008
	$[t_m, t_f]$	-4.13	-3.85	-3.92	-0.056	-0.075	0.067
2300	$[t_i, t_m]$	9.48	11.64	11.37	-0.107	0.026	0.177
	$[t_m, t_f]$	-2.92	-2.53	-1.99	0.006	-0.144	0.077
2700	$[t_i, t_f]$	10.68	13.24	13.01	-0.212	-0.194	0.166

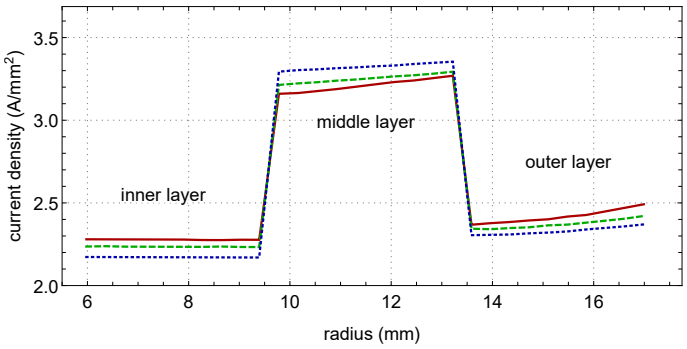

Figure 3.18: Calculated effect of temperature of the steel core on the layer's current density in a "*Grackle*" ACSR conductor at 1608 A, 60 Hz, 25 °C (——), 80 °C (- - - -), 120 °C (·····) [17].

As a matter of fact, a significant radial temperature difference between the steel core and the conductor surface exists in ACSR conductors with three or more aluminum layers at current densities above 1 A/mm^2, which increases with the total current value [27]. Differences ranging form 10 °C to 25 °C have been measured [27] and can reach up to 30 °C [38]. This radial temperature gradient should then be considered in the analysis of the results shown in Fig. 3.17.

With the steady-state radial temperature gradient, the increase in the electrical resistance of the inner layer tends to be higher than that of the outer layer, causing

the current density in the inner layer to decrease and the outer layer to increase. This redistribution of current density tends to reduce the longitudinal magnetic field intensity in the steel core. Fig. 3.17 shows the simultaneous effect of the temperature increase in the steel core and the radial temperature gradient over the current redistribution. As the total current value increases, the effect of the radial temperature gradient on the current redistribution becomes prevailing, mainly by reducing the steel core magnetization.

In order to properly model this current redistribution, the radial temperature gradient must be considered. This may be achieved by combining the electromagnetic model [15, 16] with calculations of the internal steady-state temperatures of the conductor. A new calculation model has been developed to include the radial temperature gradient in the electromagnetic model and is proposed in Chapter 4. The results obtained in an application example show the current redistribution similar to that observed experimentally, confirming the present analysis.

Chapter 4

Modeling of Steel-Cored Conductors

4.1 Introduction

This chapter presents developments in electromagnetic modeling and in the representation of the steady-state radial temperature gradient of steel-cored conductors for the calculation of their AC resistance and current distribution. These improvements are then used in application examples in which the ampacity of thermal resistant conductors is calculated for up to high currents/temperatures and compared with the mostly used ampacity calculation models.

4.2 New Electromagnetic Model - Conductor Design Optimization

This section presents a new electromagnetic model for calculating the AC resistance and current distribution of steel-cored conductors affected by the magnetization of their core. The effects of this magnetization depend on several aspects such as the current carried by the conductor and the steel magnetic properties, which can be taken into account in the equivalent circuit modeling approach, such as in [15, 16]. These models can also be used to optimize the conductors' design in order to reduce losses. However, they are not accurate at high currents when used for a conductor with a single aluminum layer [15], and their use for optimizing the conductors' design is limited to changes in the aluminum layers only [17, 37], due to their simplified representation of the steel core. These problems are overcome by refining the representation of the core in the new model, as following described.

4.2.1 Model Description

The developed model represents each layer of the conductor (including each layer of the steel core) by an equivalent circuit. In the circuits corresponding to the steel layers, the circular and longitudinal inductances resulting from the spiral current flow are represented, which had been neglected in the previous models [15, 16]. The mathematical formulation for dealing with the aluminum layers in the present thesis also differs from existing models.

It is assumed that the current density is constant in each wire and that the current follows the spiral wire path. Thus, the current produces two components of the magnetic field, one circular $\mathbf{H}\varphi$ and one longitudinal $\mathbf{H}z$, which will determine the respective circuital elements, i.e. the components of each layer's self and mutual reactances.

Flux associated to the Circular Magnetic Field

Considering the magnetic field produced by the current $\mathbf{I}_i$ flowing in a layer i, the circular component *external* to this layer, at a radial distance r from the center of the conductor, is given by

$$\mathbf{H}\varphi_{outer}(r) = \frac{\mathbf{I}_i}{2\pi r} \tag{4.1}$$

The circular component *internal* to an aluminum layer i that carries the current $\mathbf{I}_i$, in turn, is proportional to the current enclosed, as follows

$$\mathbf{H}\varphi_{inner}(r) = \frac{\mathbf{I}_i}{2\pi r}\frac{St_i(r)}{A_i}\sin\theta_i \tag{4.2}$$

where $St_i(r)$ is the fraction of the wire cross-section within the circumference of radius r, given by (D.3), see Fig. D.3 and Appendix D.2 for details. $A_i = \pi d_i^2/4$ is the area of the wire and θ_i is the stranding angle of layer i, given by

$$\theta_i = \arctan\left[\frac{\lambda_i}{\pi(D_i - d_i)}\right] \tag{4.3}$$

where D_i and λ_i are the outer diameter and lay length (pitch) of layer i, respectively, and d_i is the diameter of the wire in this layer.

The circular flux in an aluminum layer i results from the *external* circular components (4.1) produced by the steel and inner aluminum layers, and the *internal* circular component of the aluminum layer i itself (4.2). For a conductor with a steel core of n layers and one not-spiraled central wire, the circular flux in the i-th

aluminum layer per-unit length is given by

$$\begin{aligned}\boldsymbol{\phi}_i &= \mu_0 \int_{D_{i-1}/2}^{D_i/2} \mathbf{H}\varphi(r)\, dr \\ &= \frac{\mu_0}{2\pi}\left[\left(\mathbf{I}_{sc} + \sum_{q=1}^{n} \mathbf{I}_{sq} + \sum_{p=1}^{i-1} \mathbf{I}_p\right) \ln\frac{D_i}{D_{i-1}} + k_i \mathbf{I}_i\right]\end{aligned} \tag{4.4}$$

where μ_0 is the permeability of free space. D_i and D_{i-1} are the outer and inner diameter of the i-th aluminum layer, respectively. $\mathbf{I}_{sc}$, $\mathbf{I}_{sq}$ and $\mathbf{I}_p$ are the currents in the central steel wire (not-spiraled), in the q-th steel layer, and in the p-th aluminum layer, respectively. k_i is the integral given by

$$k_i = \frac{\sin\theta_i}{A_i} \int_{D_{i-1}/2}^{D_i/2} St_i(r)/r\, dr \tag{4.5}$$

which has no analytical solution and requires numerical integration.

To calculate the reactance of the aluminum layer i, it is necessary to include in equation (4.4) the fraction of the current enclosed ($St_i(r)\sin\theta_i/A_i$), as follows

$$\begin{aligned}\boldsymbol{\phi}_{i,inner} &= \mu_0 \int_{D_{i-1}/2}^{D_i/2} \mathbf{H}\varphi(r) \left(\frac{St_i(r)}{A_i}\sin\theta_i\right) dr \\ &= \frac{\mu_0}{2\pi}\left[\left(\mathbf{I}_{sc} + \sum_{q=1}^{n} \mathbf{I}_{sq} + \sum_{p=1}^{i-1} \mathbf{I}_p\right) k_i + k_{isq}\mathbf{I}_i\right]\end{aligned} \tag{4.6}$$

where k_{isq} is the integral

$$k_{isq} = \left(\frac{\sin\theta_i}{A_i}\right)^2 \int_{D_{i-1}/2}^{D_i/2} St_i^2(r)/r\, dr \tag{4.7}$$

which also requires numerical integration.

Due to the high permeability of steel, it is assumed that the *internal* circular component produced by the current in a steel layer is confined within its wires as if they were isolated from each other. This component is thus concentric to each wire and its intensity reduced (divided by the number of wires in the layer), and can therefore be neglected as in previous models [15, 16, 32, 35]. The *external* circular component (4.1) produced by the inner steel layers travels through the spiraling steel wires and, for calculating the circular flux in a steel layer, it is represented by its average value in the layer. For the i-th steel layer, the resulting circular component

of the magnetic field is given by

$$\mathbf{H}\varphi_{si} \approx \frac{1}{2\pi d_{st}} \left(\mathbf{I}_{sc} + \sum_{q=1}^{i-1} \mathbf{I}_{sq} \right) \ln \frac{D_{si}}{D_{si-1}} \tag{4.8}$$

where d_{st} is the diameter of the steel wire. D_{si} and D_{si-1} are the outer and inner diameter of the i-th steel layer. The circular magnetic flux per unit length in a steel layer i can be calculated considering the area of the longitudinal section of the steel wires only, as the permeability of the material is many times greater than that of air, as follows

$$\begin{aligned} \boldsymbol{\phi}_{si} &= \mu_0 \int_S \overline{\mu}_r(H_{si})\, \mathbf{H}\varphi_{si}\, dS \\ &= \frac{\mu_0}{2\pi} \overline{\mu}_r(H_{si}) \frac{A\ell_{si}}{d_{st}\lambda_{si}} \left(\mathbf{I}_{sc} + \sum_{q=1}^{i-1} \mathbf{I}_{sq} \right) \ln \frac{D_{si}}{D_{si-1}} \end{aligned} \tag{4.9}$$

where $\overline{\mu}_r$ is the complex relative permeability of the steel, described as a complex function of the magnetic field strength in the layer. $A\ell_{si}$ is the area of the longitudinal section of the wires in the steel layer i, its formulation being described in Appendix D.1. H_{si} is the magnetic field strength in the steel layer i, given by

$$H_{si} = \sqrt{H\varphi_{si}^2 + Hz_{si}^2} \tag{4.10}$$

where Hz_{si} is the resulting longitudinal component of the magnetic field in the i-th steel layer. For a conductor with m aluminum layers and n steel layers, the resulting longitudinal component in a steel layer i is given by

$$\mathbf{H}z_{si} = \sum_{p=1}^{m} (-1)^{m+p} \frac{\mathbf{I}_p}{\lambda_p} + \sum_{q=i}^{n} (-1)^{m+n+q} \frac{\mathbf{I}_{sq}}{\lambda_{sq}} \tag{4.11}$$

The alternation of the sign in (4.11) occurs due to the alternation in the stranding directions between layers.

To calculate the reactance of the steel layer i, the fraction of the current enclosed ($St_{si}(r) \sin\theta_{si}/A_{si}$) must be included in (4.9), as follows

$$\begin{aligned} \boldsymbol{\phi}_{si,inner} &= \mu_0 \int_S \overline{\mu}_r(H_{si})\, \mathbf{H}\varphi_{si} \left(\frac{St_{si}(r)}{A_{si}} \sin\theta_{si} \right) dS \\ &= \frac{\mu_0}{2\pi} \overline{\mu}_r(H_{si}) \frac{A\ell_{si}}{d_{st}\lambda_{si}} k_{si} \left(\mathbf{I}_{sc} + \sum_{q=1}^{i-1} \mathbf{I}_{sq} \right) \end{aligned} \tag{4.12}$$

The circular magnetic field internal to the central steel wire (not-spiraled), in

turn, is

$$\mathbf{H}\varphi_{sc}(r) = \frac{\mathbf{I}_{sc}}{2\pi(d_{st}/2)^2}\, r \tag{4.13}$$

For the calculation of the circular magnetic flux in the wire, the magnetic field can be approximated by its average value

$$\mathbf{H}\varphi_{sc} \approx \frac{\mathbf{I}_{sc}}{2\pi d_{st}} \tag{4.14}$$

and for the calculation of the reactance per unit length of the central steel wire, the fraction of the current enclosed $(2r/d_{st})^2$ is considered, as follows

$$\begin{aligned} \boldsymbol{\phi}_{sc,inner} &= \mu_0 \int_0^{dst/2} \overline{\mu}_r(H_{sc})\, \mathbf{H}\varphi_{sc}(r)(2r/d_{st})^2 dr \\ &= \frac{\mu_0}{2\pi}\overline{\mu}_r(H_{sc})\frac{\mathbf{I}_{sc}}{4} \end{aligned} \tag{4.15}$$

The reactance per unit length of an aluminum layer due to the circular magnetic flux is obtained from the inner flux of the layer (4.6) and the flux in the other aluminum layers external to it (4.4). Similarly, for a steel layer, the reactance is obtained from the inner flux of the layer (4.12) (or (4.15), for central steel wire) and the flux in the other external steel (4.9) and aluminum (4.4) layers. Reactances due to the circular magnetic field, however, are easier represented implicitly, as seen in equations (4.25)-(4.30).

Flux associated to the Longitudinal Magnetic Field

The longitudinal component of the magnetic field is assumed to be constant in the conductor cross-section, equal to that produced by a long coil having one turn per lay length (pitch). For a layer i, with lay length λ_i, the longitudinal component of the field produced by current $\mathbf{I}_i$ is given by

$$\mathbf{H}z = \pm\mathbf{I}_i/\lambda_i \tag{4.16}$$

The sign in (4.16) depends on the stranding direction of the layer, being positive for right-hand stranding direction and negative otherwise. The longitudinal magnetic flux produced by the current $\mathbf{I}_i$ is the product of $\mathbf{H}z$ by the area in which it is found, and the respective value of the complex relative permeability. The longitudinal flux produced by a steel layer i, disregarding the contribution of the flux in the air, is

given by

$$\boldsymbol{\phi} z_{si} = \mu_0 \left[\sum_{q=1}^{i} \overline{\mu}_r(H_{sq}) At_{sq} + \overline{\mu}_r(H_{sc}) A_{st} \right] \frac{\mathbf{I}_{si}}{\lambda_{si}} \tag{4.17}$$

where A_{st} is the area of the steel wire and At_{sq} is the cross-section area of the q-th steel layer, its calculation being described in Appendix D.1. H_{sc} and H_{sq} are the magnetic field strength in the central steel wire and in the q-th steel layer, respectively. The voltage induced in the layer is given by $V_{si} = j\omega\boldsymbol{\phi} z_{si}/\lambda_{si} = jX_{sisi}\mathbf{I}_{si}$, where ω is the angular frequency. The self-reactance per-unit length X_{sisi}, therefore, is given by

$$X_{sisi} = \frac{\omega\mu_0}{\lambda_{si}^2} \left[\sum_{q=1}^{i} \overline{\mu}_r(H_{sq}) At_{sq} + \overline{\mu}_r(H_{sc}) A_{st} \right] \tag{4.18}$$

Similarly, the mutual reactance per-unit length from the i-th steel to another layer p is given by

$$X_{sip} = \frac{\omega\mu_0}{\lambda_{si}\lambda_p} \left[\sum_{q=1}^{i \text{ or } p} \overline{\mu}_r(H_{sq}) At_{sq} + \overline{\mu}_r(H_{sc}) A_{st} \right] \tag{4.19}$$

Since X_{sip} is the result of the common magnetic flux between the steel layer i and layer p, the upper bound of the summation in (4.19) is the index of the innermost layer between i and p. The sign of X_{sip} is positive for layers stranded in the same direction, and negative otherwise.

The longitudinal magnetic flux produced by an aluminum layer, in turn, extends to the region outside the steel core, composed of aluminum and air. For a conductor with n steel layers, the longitudinal magnetic flux produced by the i-th aluminum layer is

$$\boldsymbol{\phi} z_i = \mu_0 \left\{ \left[(D_i - d)^2 - D_{sn}^2 \right] \frac{\pi}{4} + \sum_{q=1}^{n} \overline{\mu}_r(H_{sq}) At_{sq} + \overline{\mu}_r(H_{sc}) A_{st} \right\} \mathbf{I}_i/\lambda_i \tag{4.20}$$

where D_{sn} is the outer diameter of the steel core. The self-reactance per-unit length of the layer is

$$X_{ii} = \frac{\omega\mu_0}{\lambda_i^2} \left\{ \left[(D_i - d)^2 - D_{sn}^2 \right] \frac{\pi}{4} + \sum_{q=1}^{n} \overline{\mu}_r(H_{sq}) At_{sq} + \overline{\mu}_r(H_{sc}) A_{st} \right\} \tag{4.21}$$

Similarly, the mutual reactance per-unit length from the aluminum layers i and

p is given by

$$X_{ip} = \frac{\omega\mu_0}{\lambda_i\lambda_p}\left\{ \left[(D_{min}-d)^2 - D_{sn}^2\right]\frac{\pi}{4} + \sum_{q=1}^{n}\overline{\mu}_r(H_{sq})At_{sq} + \overline{\mu}_r(H_{sc})A_{st}\right\} \tag{4.22}$$

where D_{min} is the smallest diameter between those of aluminum layers i and p.

Electrical Resistance

The electrical resistance per unit length of each layer is calculated from the corresponding direct current value, as described below.

The resistance per-unit length of the central wire, not-spiraled, is given by

$$R_{sc} = \rho_{st}/A_{st} \tag{4.23}$$

where ρ_{st} is the steel resistivity. The resistance of a spiral layer i is calculated in the same way as the existing model [15], given by

$$R_i = \frac{\rho_i}{n_i A_i}\sqrt{1 + \left[\pi\left(D_i - d_i\right)/\lambda_i\right]^2} \tag{4.24}$$

where ρ_i is the resistivity of the layer material, A_i is the area of the wires in the layer i, and n_i is the number of its wires.

The voltage drop on the conductor outer surface $\mathbf{V}$ is then described as a function of the current flow in each layer of the conductor. For a steel-cored conductor, for example, with 3 aluminum layers, 2 steel layers and one central steel wire, the voltage drop per meter length on the conductor surface $\mathbf{V}$ is described by (4.25)-(4.30) as a function of the flow of current in the central steel wire, first, second steel layers, and the inner, middle and outer aluminum layers, respectively.

$$\begin{aligned}
\mathbf{V} =& R_{sc}\mathbf{I}_{sc} + j\frac{\omega\mu_0}{2\pi}\overline{\mu}_r(H_{sc})\frac{\mathbf{I}_{sc}}{4} \\
&+ j\frac{\omega\mu_0}{2\pi}\overline{\mu}_r(H_{s1})\frac{A_{\ell s1}}{d_{st}\lambda_{s1}}\mathbf{I}_{sc}\ln\frac{D_{s1}}{d_{st}} \\
&+ j\frac{\omega\mu_0}{2\pi}\overline{\mu}_r(H_{s2})\frac{A_{\ell s2}}{d_{st}\lambda_{s2}}\left(\mathbf{I}_{sc}+\mathbf{I}_{s1}\right)\ln\frac{D_{s2}}{D_{s1}} \\
&+ j\frac{\omega\mu_0}{2\pi}\left[\left(\mathbf{I}_{sc}+\mathbf{I}_{s1}+\mathbf{I}_{s2}\right)\ln\frac{D_1}{D_{s2}} + k_1\mathbf{I}_1\right] \\
&+ j\frac{\omega\mu_0}{2\pi}\left[\left(\mathbf{I}_{sc}+\mathbf{I}_{s1}+\mathbf{I}_{s2}+\mathbf{I}_1\right)\ln\frac{D_2}{D_1} + k_2\mathbf{I}_2\right] \\
&+ j\frac{\omega\mu_0}{2\pi}\left[\left(\mathbf{I}_{sc}+\mathbf{I}_{s1}+\mathbf{I}_{s2}+\mathbf{I}_1+\mathbf{I}_2\right)\ln\frac{D_3}{D_2} + k_3\mathbf{I}_3\right]
\end{aligned} \tag{4.25}$$

$$
\begin{aligned}
\mathbf{V} =& R_{s1}\mathbf{I}_{s1} + jX_{s1s1}\mathbf{I}_{s1} - jX_{s1s2}\mathbf{I}_{s2} \\
&+ jX_{s11}\mathbf{I}_1 - jX_{s12}\mathbf{I}_2 + jX_{s13}\mathbf{I}_3 \\
&+ j\frac{\omega\mu_0}{2\pi}\overline{\mu}_r(H_{s1})\frac{A_{\ell s1}}{d_{st}\lambda_{s1}}k_{s1}\mathbf{I}_{sc} \\
&+ j\frac{\omega\mu_0}{2\pi}\overline{\mu}_r(H_{s2})\frac{A_{\ell s2}}{d_{st}\lambda_{s2}}\left(\mathbf{I}_{sc}+\mathbf{I}_{s1}\right)\ln\frac{D_{s2}}{D_{s1}} \\
&+ j\frac{\omega\mu_0}{2\pi}\left[\left(\mathbf{I}_{sc}+\mathbf{I}_{s1}+\mathbf{I}_{s2}\right)\ln\frac{D_1}{D_{s2}} + k_1\mathbf{I}_1\right] \\
&+ j\frac{\omega\mu_0}{2\pi}\left[\left(\mathbf{I}_{sc}+\mathbf{I}_{s1}+\mathbf{I}_{s2}+\mathbf{I}_1\right)\ln\frac{D_2}{D_1} + k_2\mathbf{I}_2\right] \\
&+ j\frac{\omega\mu_0}{2\pi}\left[\left(\mathbf{I}_{sc}+\mathbf{I}_{s1}+\mathbf{I}_{s2}+\mathbf{I}_1+\mathbf{I}_2\right)\ln\frac{D_3}{D_2} + k_3\mathbf{I}_3\right]
\end{aligned}
\tag{4.26}
$$

$$
\begin{aligned}
\mathbf{V} =& R_{s2}\mathbf{I}_{s2} - jX_{s1s2}\mathbf{I}_{s1} + jX_{s2s2}\mathbf{I}_{s2} \\
&- jX_{s21}\mathbf{I}_1 + jX_{s22}\mathbf{I}_2 - jX_{s23}\mathbf{I}_3 \\
&+ j\frac{\omega\mu_0}{2\pi}\overline{\mu}_r(H_{s2})\frac{A_{\ell s2}}{d_{st}\lambda_{s2}}k_{s2}\left(\mathbf{I}_{sc}+\mathbf{I}_{s1}\right) \\
&+ j\frac{\omega\mu_0}{2\pi}\left[\left(\mathbf{I}_{sc}+\mathbf{I}_{s1}+\mathbf{I}_{s2}\right)\ln\frac{D_1}{D_{s2}} + k_1\mathbf{I}_1\right] \\
&+ j\frac{\omega\mu_0}{2\pi}\left[\left(\mathbf{I}_{sc}+\mathbf{I}_{s1}+\mathbf{I}_{s2}+\mathbf{I}_1\right)\ln\frac{D_2}{D_1} + k_2\mathbf{I}_2\right] \\
&+ j\frac{\omega\mu_0}{2\pi}\left[\left(\mathbf{I}_{sc}+\mathbf{I}_{s1}+\mathbf{I}_{s2}+\mathbf{I}_1+\mathbf{I}_2\right)\ln\frac{D_3}{D_2} + k_3\mathbf{I}_3\right]
\end{aligned}
\tag{4.27}
$$

$$
\begin{aligned}
\mathbf{V} =& R_1\mathbf{I}_1 + jX_{s11}\mathbf{I}_{s1} - jX_{s21}\mathbf{I}_{s2} \\
&+ jX_{11}\mathbf{I}_1 - jX_{12}\mathbf{I}_2 + jX_{13}\mathbf{I}_3 \\
&+ j\frac{\omega\mu_0}{2\pi}\left[\left(\mathbf{I}_{sc}+\mathbf{I}_{s1}+\mathbf{I}_{s2}\right)k_1 + k_{1sq}\mathbf{I}_1\right] \\
&+ j\frac{\omega\mu_0}{2\pi}\left[\left(\mathbf{I}_{sc}+\mathbf{I}_{s1}+\mathbf{I}_{s2}+\mathbf{I}_1\right)\ln\frac{D_2}{D_1} + k_2\mathbf{I}_2\right] \\
&+ j\frac{\omega\mu_0}{2\pi}\left[\left(\mathbf{I}_{sc}+\mathbf{I}_{s1}+\mathbf{I}_{s2}+\mathbf{I}_1+\mathbf{I}_2\right)\ln\frac{D_3}{D_2} + k_3\mathbf{I}_3\right]
\end{aligned}
\tag{4.28}
$$

$$
\begin{aligned}
\mathbf{V} =& R_2\mathbf{I}_2 - jX_{s12}\mathbf{I}_{s1} + jX_{s22}\mathbf{I}_{s2} \\
&- jX_{12}\mathbf{I}_1 + jX_{22}\mathbf{I}_2 - jX_{23}\mathbf{I}_3 \\
&+ j\frac{\omega\mu_0}{2\pi}\left[\left(\mathbf{I}_{sc}+\mathbf{I}_{s1}+\mathbf{I}_{s2}+\mathbf{I}_1\right)k_2 + k_{2sq}\mathbf{I}_2\right] \\
&+ j\frac{\omega\mu_0}{2\pi}\left[\left(\mathbf{I}_{sc}+\mathbf{I}_{s1}+\mathbf{I}_{s2}+\mathbf{I}_1+\mathbf{I}_2\right)\ln\frac{D_3}{D_2} + k_3\mathbf{I}_3\right]
\end{aligned}
\tag{4.29}
$$

$$\begin{aligned}\mathbf{V} =& R_3\mathbf{I}_3 + jX_{s13}\mathbf{I}_{s1} - jX_{s23}\mathbf{I}_{s2} \\ &+ jX_{13}\mathbf{I}_1 - jX_{23}\mathbf{I}_2 + jX_{33}\mathbf{I}_3 \\ &+ j\frac{\omega\mu_0}{2\pi}\left[\left(\mathbf{I}_{sc} + \mathbf{I}_{s1} + \mathbf{I}_{s2} + \mathbf{I}_1 + \mathbf{I}_2\right)k_3 + k_{3sq}\mathbf{I}_3\right]\end{aligned} \tag{4.30}$$

where the subscripts sc, $s1$ and $s2$ correspond to the central steel wire, first and second steel layer, respectively. Subscripts 1, 2 and 3 corresponds to the inner, middle and outer aluminum layers, respectively.

In addition to equations (4.25) to (4.30), the total current carried by the conductor I_{total} must be equal the sum of the currents in each layer

$$\mathbf{I}_{sc} + \mathbf{I}_{s1} + \mathbf{I}_{s2} + \mathbf{I}_1 + \mathbf{I}_2 + \mathbf{I}_3 = I_{total} \tag{4.31}$$

where I_{total} is used as a reference, being assumed with phase zero.

The solution of the set of equations from (4.25) to (4.31) gives the current distribution and the voltage drop on the surface of the conductor $\mathbf{V}$. The conductor's AC resistance R_{ac} is found by

$$R_{ac} = Re\left(\mathbf{V}/I_{total}\right) \tag{4.32}$$

4.2.2 Application Example and Validation

In order to compare the present model with the one by Barrett *et al.* [15], the experimental data used to validate the latter was used. The data covers the AC/DC resistance ratio of an ACSR "*Grackle*" conductor for a wide current range and the complex permeability of its steel core. This conductor has three aluminum layers and a steel core with two layers and one central wire. Further details of the conductor are given in Appendix A.2. Experimental results obtained on the "*Grackle*" conductor with its inner aluminum layer only (obtained by removing its two outer aluminum layers) were also used. In the latter case, the magnetization of the core and its effect on the conductor resistance are higher than in the conductor with three aluminum layers. The values of the AC/DC resistance ratio for different total current values, measured in [15] and calculated using the developed model and the one proposed in [15] are shown in Fig. 4.1. For the calculation using the developed model, the lay length (pitch) of the internal steel layer was assumed to be 170 mm, which corresponds to the preferred lay ratio (ratio of the layer lay length to its outer diameter) value of this conductor based on American Society for Testing and Materials (ASTM) standard B232. This parameter is not given in [15].

Fig. 4.1(a) shows that the results obtained by both models are very similar and in agreement with the measured values for the three-layer "*Grackle*" conductor. Nevertheless, a slightly better agreement is obtained by the developed model for total

current values above 1200 A. In the case of the conductor with its inner aluminum layer only, see Fig. 4.1(b), the difference between results obtained by the two models is significant for total current values above 400 A, and only the results obtained by the new model remain in agreement with the measured values in the whole current range. The calculations are limited to the total current of 900 A because above this value the magnetic field are beyond the range in which the measured steel core permeability is available [15].

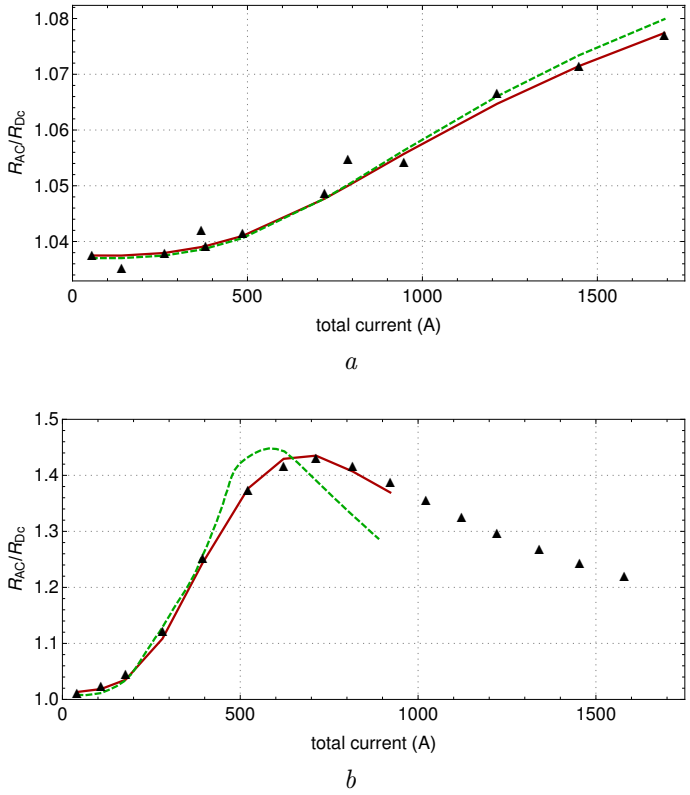

Figure 4.1: Variation of the AC/DC resistance ratio with the total current value of an ACSR "*Grackle*" conductor with three aluminum layers (a) and of this conductor with the inner aluminum layer only (b), measured (▲) [15], calculated using the new model (——) and the model by Barrett in [15] (- - - -).

The difference between results can be attributed to the redistribution of the current in the steel layers and to the reduction of the core magnetization caused by the magnetic field produced in the these layers, which are only represented in the developed model.

Indeed, since the steel layers encircle, even partially, the longitudinal magnetic flux in the core, these layers are also affected by the transformer effect and a current redistribution similar to which occurs in the aluminum layers should be expected. The current in steel layers stranded in the same direction as that of the middle aluminum layer should then increase and in the other layers decrease. This is observed in the results obtained by the developed model, depicted in Fig. 4.2. Results

show a concentration of current density in the outer steel layer, which is stranded in the same direction as that of the middle aluminum layer, and this concentration increases with the total current value. In the case of the conductor with its inner aluminum layer only (see Fig. 4.2(b)), the current concentration is higher than that of the three-layer "*Grackle*" conductor, due to the higher magnetization of its steel core.

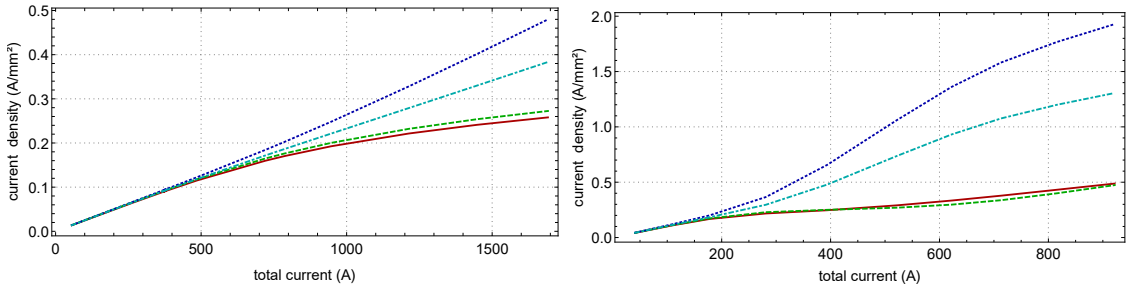

a *b*

Figure 4.2: Variation of current density with the total current value, for an ACSR "*Grackle*" conductor with three aluminum layers (*a*) and with the inner aluminum layer only (*b*), calculated using the developed model, in the central steel wire (——), inner steel layer (- - - -), outer steel layer (·····), and the mean value in the steel core (- · - · -).

The concentration of current in the outer steel layer causes the magnetic field produced in the layer to become more significant than expected and than that produced in the other steel layers. The longitudinal component produced by the outer steel layer, in turn, is opposed to the core magnetization and reduce the resulting longitudinal component in all steel layers. This reduction is not considered by the model proposed in [15], which assumes the longitudinal component in the core equal to that in the inner aluminum layer. Fig. 4.3 shows the values of the resulting longitudinal component in the steel core and in the inner aluminum layer obtained by both models. As Fig. 4.3 shows, the magnetic field in the steel layers calculated using the developed model ($\mathbf{H}z_{s2}$ and $\mathbf{H}z_{s1}$) are lower than the values in the inner aluminum layer ($\mathbf{H}z_1$), and the difference increases with the total current value due to the increase in the current redistribution in the steel layers seen in Fig. 4.2. This difference is greater for the conductor with the inner aluminum layer only (see Fig. 4.3(b)) due to the greater current redistribution. The difference between the resulting magnetic fields in the steel core calculated by both models results into the difference of the calculated AC/DC resistance ratio.

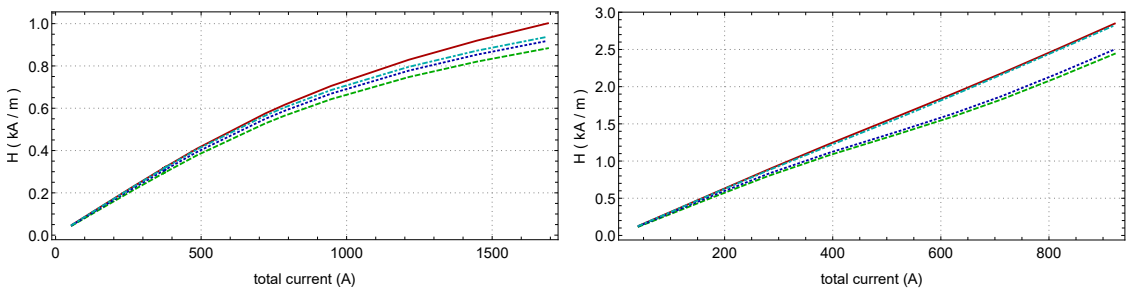

a *b*

Figure 4.3: Variation of the resulting longitudinal component of the magnetic field with the total current value, for an ACSR "*Grackle*" conductor with three aluminum layers (*a*) and with the inner aluminum layer only (*b*), calculated using the developed model in the inner aluminum layer ($\mathbf{H}z_1$) (——), in the outer steel layer ($\mathbf{H}z_{s2}$) (- - - -) and in the inner steel layer ($\mathbf{H}z_{s1}$) (·····), and calculated using the model proposed in [15] in the whole steel core ($\mathbf{H}z$) (-·-·-·).

4.2.3 Improving Conductor Design to Reduce Losses

"*Grackle*" conductor (three aluminum layers)

Low-loss "*Grackle*" conductors were proposed in [17, 37], by modifying the lay length (pitch) of their aluminum layers. The variation of the AC/DC resistance ratio with the total current value, of the original and modified conductors is depicted in Fig. 4.4. Results show that it was possible to significantly reduce the conductor resistance and its increase with the total current value. However, in the design of stranded conductors, the lay length (pitch) of each layer must be such that its lay ratio (ratio of the layer lay length to its outer diameter) is within a range of standard values and shall not greater than the lay ratio of the layer immediately beneath it. While the low-loss conductor proposed in [37] did not meet the first specification, the one proposed in [17] did not meet the second one.

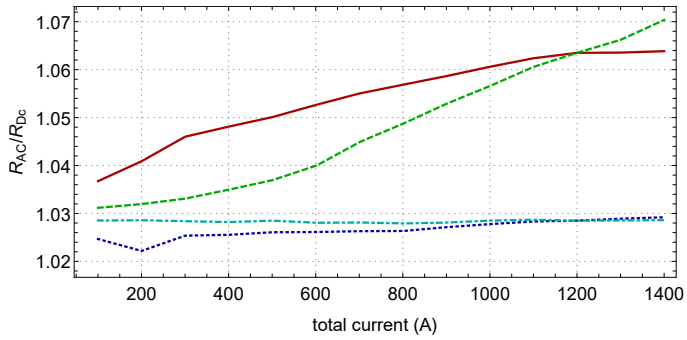

Figure 4.4: Variation of the AC/DC resistance ratio with the total current value of a "*Grackle*" conductor at 20 °C, measured in [37] (——), calculated in [17] (- - - -), and of the low-loss "*Grackle*" conductor proposed in [37] (·····) and in [17] (-·-·-·).

Following, two alternative low-loss "*Grackle*" conductors are proposed, respect-

ing the standard IEC 61089: "Low-loss A", which corresponds to improving the aluminum layers design only, and "Low-loss B" obtained by improving both the aluminum and steel core layers. In this case, further to the pitch, the possibility of changing the number of steel layers, while keeping the steel cross-sectional area, was also considered.

Results are shown in Fig. 4.5 and the lay ratio of each layer in the original and modified conductor are given in Table 4.1. As results for "Low-loss A" show, the resistance could not be reduced as much as in previous studies, due to the restriction of the lay length (pitch) values imposed by the standard. However, it is shown that further reduction can be obtained by acting on the steel core, given its impact on reducing the magnetization of the core seen in section 4.2.2. Optimized results were obtained for a steel core of a six-wire layer and central wire. Having a smaller number of steel wires (six instead of nineteen), this conductor has higher currents in its layers than the original one for the same total current value. Higher currents in the outer steel layers, in turn, further reduce the longitudinal component in the steel core. It is important to note that the results of the modified steel core conductor can only be calculated using the new model.

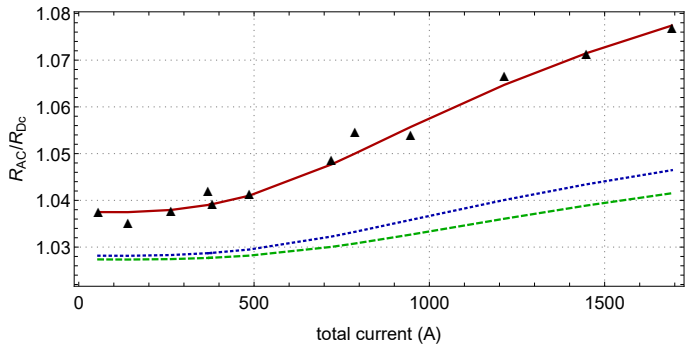

Figure 4.5: Variation of the AC/DC resistance ratio with the total current value of the ACSR "*Grackle*" conductor, measured at 20 °C (▲) [15], and calculated values of the original conductor (——), low-loss conductor obtained by modifying the aluminum layers only "Low-loss A" (·····) and modifying both aluminum and steel layers "Low-loss B" (- - - -).

Modified "*Grackle*" conductor (one aluminum layer)

In order to illustrate the case of conductors with a single aluminum layer, which have greater core magnetization, the "*Grackle*" conductor with its inner aluminum layer only, tested by Barrett, was considered. It must be noticed that the lay length (pitch) of the aluminum layer is already higher than the standard maximum value, so it was kept unchanged. In this context, the loss reduction can only be obtained by modifying the steel core. Results corresponding to a steel core similar to case "Low-loss B" are shown in Fig. 4.6. It is plain that the effect of modifying the steel

Table 4.1: Lay Ratio of the original conductor and the designed low-loss conductors.

Conductor	Lay ratio				
	Steel wire layers		Aluminum wire layers		
	6 wires	12 wires	Inner	Middle	Outer
Original, 3L	NG	16.58	15.43	13.83	12.09
Low-loss A, 3L	25.00	16.58	16.00	10.00	10.00
Low-loss B, 3L	16.00	–	16.00	10.00	10.00
Low-loss, 1L	16.00	–	15.43	–	–

NG = Not Given
3L = Three aluminum layers
1L = Single aluminum layer

core design is more pronounced than for three-aluminum layers. Again, these results can only be calculated by the new model.

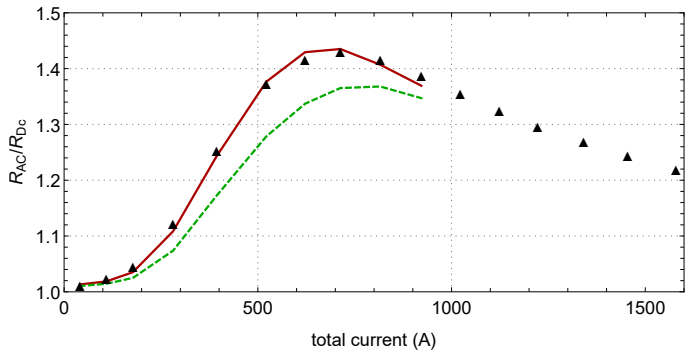

Figure 4.6: Variation of the AC/DC resistance ratio with the total current value of the ACSR "*Grackle*" conductor with its inner aluminum layer only, measured at 20 °C (▲) [15], and calculated values of the original conductor (——), and low-loss conductor (-----) (both obtained using the new model).

4.3 Including Radial Temperature Gradient

4.3.1 Motivation

The experimental results presented in section 3.3 show a current redistribution between the internal and external aluminum layers of the "*Duck*" conductor during its heating for current values above 1000 A. This redistribution increases with the total current value and was attributed to the presence of the steady-state radial temperature gradient, which is significant in ACSR conductors with three or more aluminum layers at current densities above 1 A/mm^2 [27]. To analyze the effect of

this temperature gradient, it must be considered in electromagnetic modeling.

This section presents a calculation algorithm in which the new electromagnetic model is combined with the calculation of the steady-state radial temperature gradient for steel-cored conductors with three aluminum layers. Then, the effect of this temperature gradient on the current distribution and the conductor resistance is analyzed in application examples.

4.3.2 Algorithm Description

In order to properly calculate the conductor AC resistance and its current distribution considering the steady-state radial temperature gradient, an iterative procedure must be carried out, as the temperature gradient depends on the conductor AC resistance and vice versa.

In the developed procedure, the conductor AC resistance and current distribution is calculated using the new electromagnetic model, presented in section 4.2, considering the effect of temperature on the resistance of each layer and on the permeability of the steel core. The radial temperature difference is then calculated from the obtained AC resistance, and the temperature in each aluminum layer of the conductor is calculated. Then, the calculations of the conductor resistance and temperatures are repeated until convergence occurs.

The calculation is carried out for a given total current value I_{total} and a convergence tolerance ε. Five different temperatures are considered along the conductor radius, as shown in Fig. 4.7, and the temperature on the conductor surface T_s or in the steel core T_c is fixed at a temperature value T_f. The algorithm flowchart is shown in Fig. 4.8 and its steps are described below:

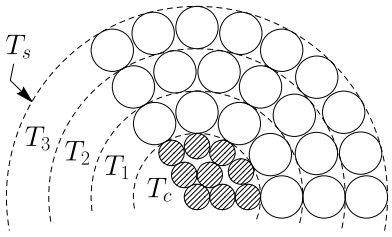

Figure 4.7: Different temperatures along the conductor radius considered in the calculation algorithm.

1. Set $R_{ac}^{(0)} = 0$, $T_c^{(0)} = T_1^{(0)} = T_2^{(0)} = T_3^{(0)} = T_s^{(0)} = T_f$, where T_1, T_2 and T_3 are the temperature in the inner, middle and outer aluminum layers, respectively. The iteration index k is set to 0.

2. Correct the resistance of each layer (given by (4.23) or (4.24)) considering its respective temperature. For a layer i, its resistance corrected to a temperature

$T_i^{(k)}$ is given by

$$R_{i,T_i} = R_i \left[1 + \alpha_i \left(T_i^{(k)} - 20\right)\right] \tag{4.33}$$

where R_i is the electrical resistance per unit length of the layer i at 20 °C, and α_i is the temperature coefficient of resistivity of the layer material.

3. Solve the set of equations of the developed electromagnetic model, from (4.25) to (4.31), considering the steel core permeability at temperature $T_c^{(k)}$ and each layer resistance calculated in the previous step, then calculate $R_{ac}^{(k+1)}$ (4.32).

4. If $\left|\dfrac{R_{ac}^{(k+1)} - R_{ac}^{(k)}}{R_{ac}^{(k+1)}}\right| \leq \varepsilon$ than stop.

5. Set $k = k + 1$. Calculate the radial temperature gradient [61] as follows

$$\Delta T^{(k)} = T_c^{(k)} - T_s^{(k)} = \frac{R_{ac}^{(k)} I_{total}^2}{2\pi k_{th}} \left(\frac{1}{2} - \frac{D_c^2}{D_s^2 - D_c^2} \ln \frac{D_s}{D_c}\right) \tag{4.34}$$

where k_{th} is the effective thermal conductivity of the aluminum layers. D_s and D_c are the outer diameter of the conductor and its core, respectively.

6. Since T_c or T_s is fixed, the non-fixed term is calculated from $\Delta T^{(k)}$ in (4.34). The temperature in the aluminum layers is then calculated. The temperature in the i-th layer is given by

$$T_i^{(k)} = T_c^{(k)} - \Delta T^{(k)} \frac{D_i - d - D_s}{D_s - D_c} \tag{4.35}$$

where d is the diameter of the aluminum wire.

7. Repeat steps 2–6 until a specified number of iterations has been reached.

4.3.3 Application Example

Effect of radial temperature gradient on current density distribution

In order to analyze if the current redistribution observed experimentally in section 3.3 can be represented and expected for other steel-cored conductors, the calculation algorithm described above was used to calculate the initial and final current density distribution in a "*Grackle*" conductor considering its heating with a constant total current value of 1608 A, at 60 Hz, for which the current density was measured at 20 °C [15], and the effect of the temperature increase was calculated [17] (see Fig. 3.18). The initial conductor temperature is assumed to be 25 °C, uniform,

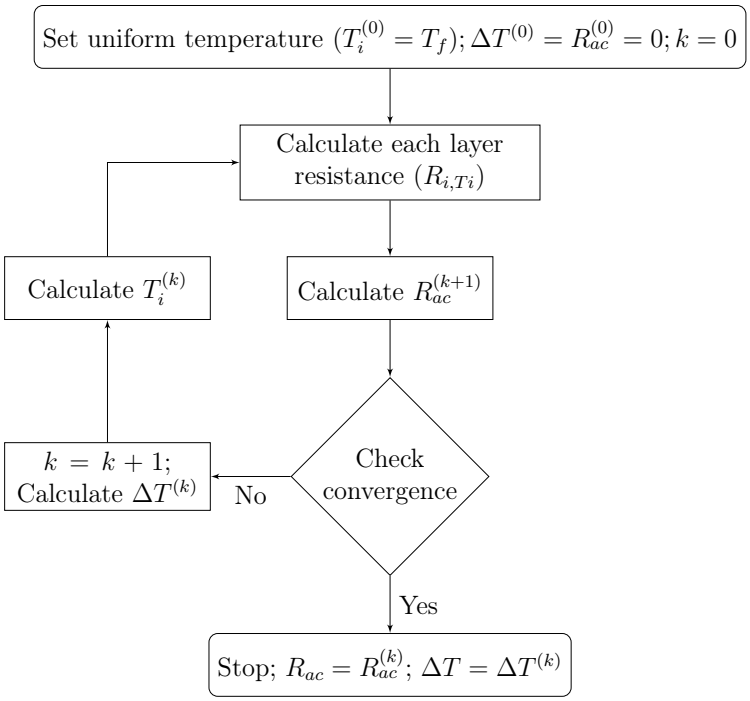

Figure 4.8: Algorithm flowchart.

equal to the room temperature and the final temperature in the steel core to be 80 °C. Details of the conductor are given in Appendix A.2.

The final current density distribution is calculated considering both the uniform radial conductor temperature, as considered in literature [17], and the radial temperature gradient. In the latter case, the calculation was performed in *Wolfram Mathematica* software using a 2.5 GHz, Core i5-7300HQ computer with 32 GB of RAM, taking just 0.26 seconds and 5 iterations, considering the convergence tolerance of 10^{-3} %. The complex permeability of the steel core at temperatures from 25 °C to 120 °C, at zero mechanical stress [22], was used. The effective thermal conductivity of 0.62 W/m °C was assumed, which is obtained from an ACSR conductor under low stress, in an indoor facility [62].

The calculated current density distributions are given in Table 4.2 and depicted in Fig. 4.9 along with the values measured at 20 °C [15], showing the consistency of the used model. The difference between the final current density distributions calculated considering or disregarding the radial temperature gradient is seen in the inner and outer aluminum layers of the conductor. As expected, the current density in the inner layer is reduced and in the outer layer is increased by considering the temperature gradient. The difference between the final temperatures of each layer due to the temperature gradient leads to different values of their DC electrical resistance increase, which are temperature dependent, thus resulting into a different current density distribution. In this example, the computed DC electrical resistance of each layer, given in Table 4.3, increases by 22% considering the uniform radial conductor

temperature. Assuming the temperature gradient, the electrical resistance increases by 21%, 19% and 17% for the inner, middle and outer layers, respectively.

It is important to note that the current density in the outer layer, calculated considering the temperature gradient, is even higher than the initial current density in the same layer, at 25 °C. This variation is similar to what was experimentally observed and opposite to the expected variation considering the uniform conductor temperature, showing the importance of combining the electromagnetic model with the thermal model of the conductor. The effect of the radial temperature gradient on the conductor resistance is following analyzed.

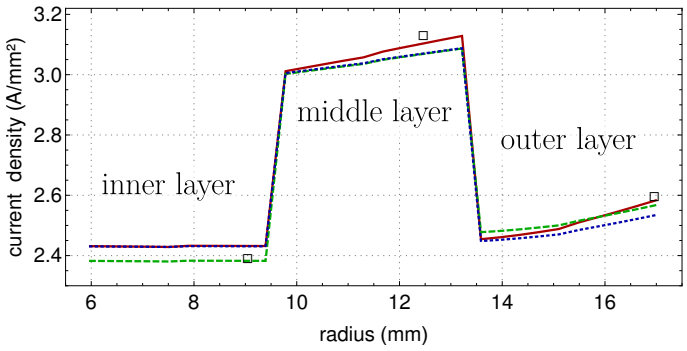

Figure 4.9: Radial distribution of current density in an ACSR "*Grackle*" conductor at 1608 A, 60 Hz, 20 °C (▫), calculated at 25 °C (——), and 80 °C, considering radial temperature gradient (- - - -) and the uniform radial conductor temperature (·····).

Table 4.2: Calculated initial and final current density distribution in an ACSR "*Grackle*" heated with a constant total current value of 1608 A, 60 Hz.

Steel Core Temperature (°C)	Current Density (A/mm²)			Magnetic Field Strength (A/m)		Magnetic Flux in the core (10^{-6} Wb)
	Aluminum Layers			Steel Layers		
	Inner	Middle	Outer	Inner	Outer	
25 (U)	2.429	3.057	2.488	951.1	914.2	11.69
80 (N)	2.380	3.036	2.500	963.0	925.5	12.20
80 (U)	2.429	3.038	2.470	964.1	925.6	12.22

U = Uniform radial conductor temperature
N = Non-Uniform radial conductor temperature (ΔT = 14.5 °C)

Effect of radial temperature gradient on AC resistance

To analyze the effect of the steady-state radial temperature gradient on the AC resistance, the calculation on the "*Grackle*" conductor using the developed algorithm was extended to a wide range of total current values, considering both the uniform

Table 4.3: Calculated initial and final current density distribution in an ACSR "*Grackle*" heated with a constant total current value of 1608 A, 60 Hz.

Steel Core Temperature (°C)	DC Resistance ($\mu\Omega$/m)		
	Aluminum Layers		
	Inner	Middle	Outer
25 (U)	216.9	145.4	111.9
80 (N)	262.1	172.9	131.0
80 (U)	264.2	177.1	136.3

U = Uniform radial conductor temperature
N = Non-Uniform radial conductor temperature (ΔT = 14.5 °C)

radial conductor temperature and the radial temperature gradient, for several values of effective thermal conductivity within the range found in the literature (from 0.5 to 4.0 W/(m°C)) [63]. Lower values of thermal conductivity lead to higher temperature gradients.

Results of the AC resistance and the radial temperature difference ΔT obtained for different fixed temperature values in the steel core T_c and on the conductor surface T_s are shown in Fig. 4.10 and Fig. 4.11, respectively. The current density on the upper axis of the figures corresponds to the value of the total current divided by the conductor total aluminum area (603 mm^2). Results show an increase in the radial temperature difference with the total current value and with the decrease in the effective thermal conductivity value, as expected (see Fig. 4.10(c), 4.10(d)), 4.11(c), and 4.11(d)). Furthermore, the radial temperature difference value is less than 5 °C for current densities less than 1 A/mm^2, and less than 25 °C for higher current densities, and therefore, it is in agreement with the measured values for conventional ACSR conductors reported in the literature [27].

In the case of the calculation considering a fixed temperature value T_c in the steel core, the value of the temperature in the outer layers is lower than T_c, resulting from the temperature gradient ΔT. Since the resistance of each layer increases with temperature, the resistance of the conductor with a uniform temperature value T_c is higher than that of the same conductor with the temperature value T_c in its core and lower temperature values in the outer layers. The higher the gradient, the lower the conductor resistance, as shown in Fig. 4.10.

In the case of the calculation considering a fixed temperature value T_s on the conductor surface, the opposite occurs. The temperature value in the inner layers is greater than T_s, resulting from the temperature gradient ΔT. The resistance of

the conductor with a uniform temperature value T_s is lower than that of the same conductor with the temperature gradient, as shown in Fig. 4.11.

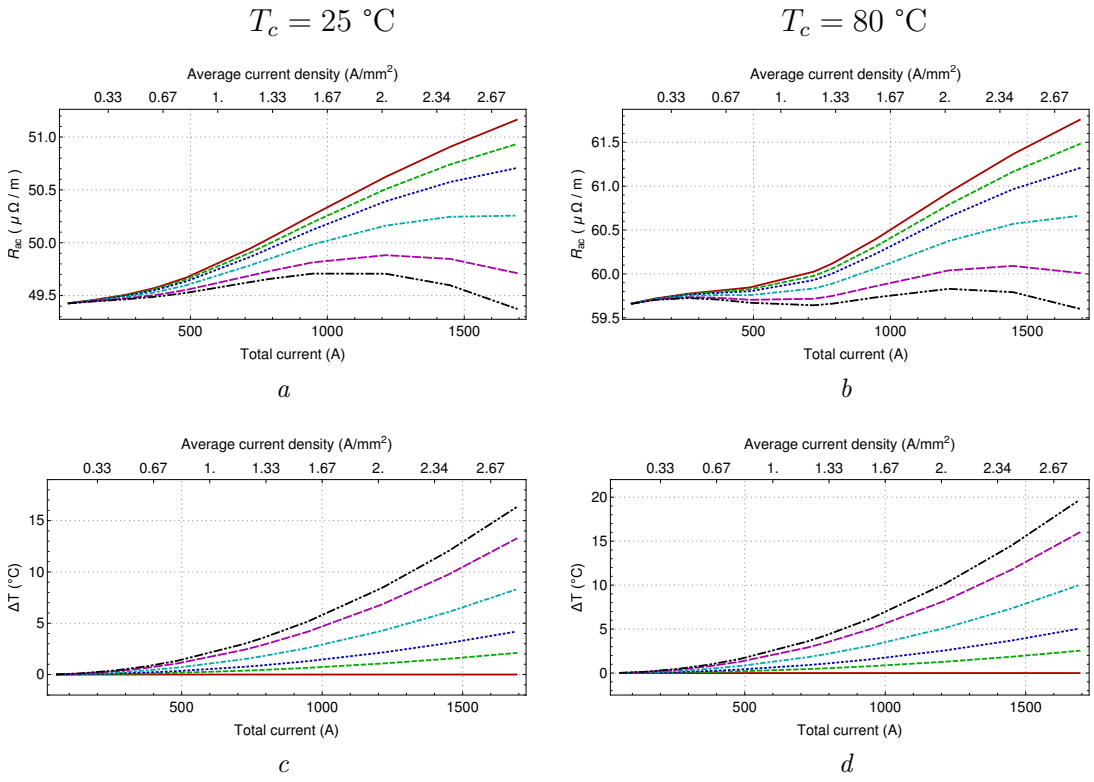

Figure 4.10: Calculated variation of AC resistance and radial temperature gradient ΔT with the total current value of an ACSR "*Grackle*" conductor, for steel core temperature $T_c = 25$ °C (a) and (c), and $T_c = 80$ °C (b) and (d), considering uniform radial temperature (——) and effective thermal conductivity of 4 W/(m°C) (-----), 2 W/(m°C) (·····), 1 W/(m°C) (-·---), 0.62 W/(m°C) (– – –), and 0.5 W/(m°C) (-·-·-).

Furthermore, it was seen in the previous application example (see Fig. 4.9), that the current redistribution caused by the temperature gradient had a negligible effect on the magnetization of the steel core, i.e., the difference between the magnetic flux in the core calculated considering and disregarding the temperature gradient was negligible, see Table 4.2. In order to verify if the temperature gradient could not affect the core magnetization, the magnetic flux in the core was calculated for several other cases.

It was then found that the effect of the temperature gradient on the core magnetization is negligible when considering a fixed temperature in the steel core, but not when considering a fixed temperature on the conductor surface. Fig. 4.12 shows the magnetic flux in the core and the temperature gradient calculated considering different thermal conductivities and for conductor surface temperature values of 60 °C and 100 °C. For the same total current value, higher magnetic fluxes are obtained for higher temperature gradients. This is due to the higher temperature values in the steel core resulting from the gradient and the permeability dependence on tem-

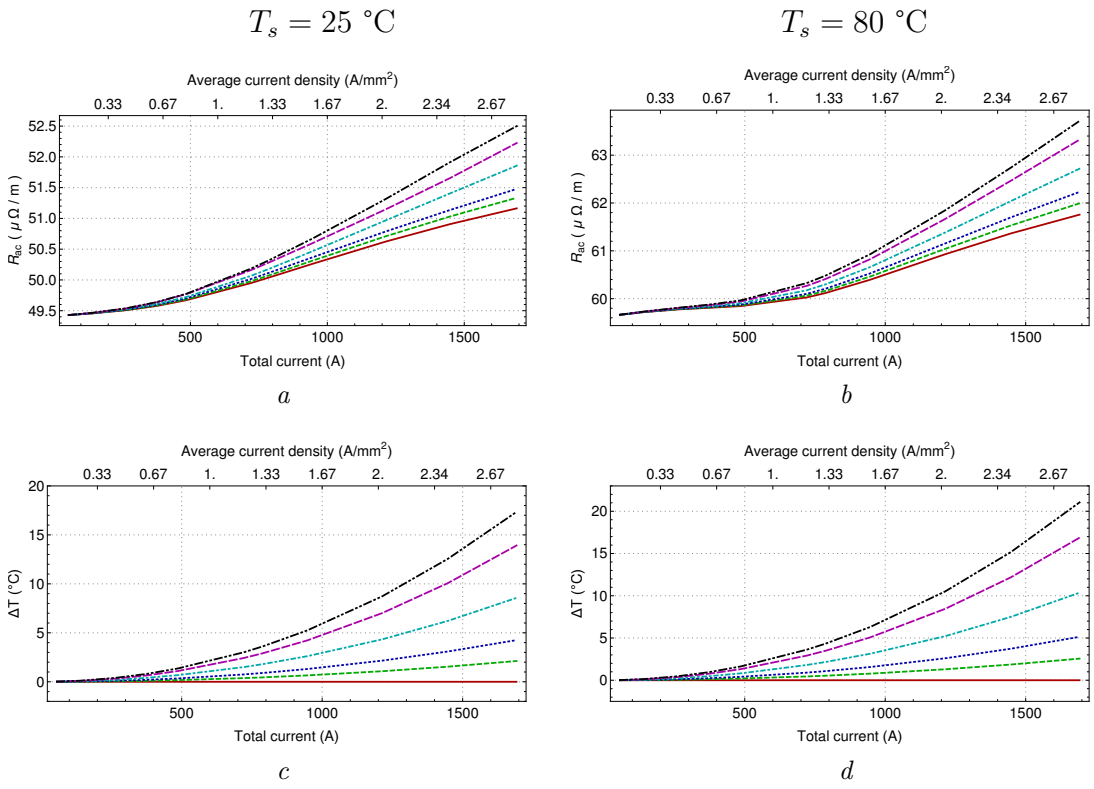

Figure 4.11: Calculated variation of AC resistance and radial temperature gradient ΔT with the total current value of an ACSR "*Grackle*" conductor, for conductor surface temperature $T_s = 25$ °C (a) and (c), and $T_s = 80$ °C (b) and (d), considering uniform radial temperature (——) and effective thermal conductivity of 4 W/(m°C) (- - - -), 2 W/(m°C) (·····), 1 W/(m°C) (-·-·-), 0.62 W/(m°C) (- - -), and 0.5 W/(m°C) (-···-).

perature. As the total current value increases, so does the temperature gradient and then the difference between the calculated fluxes. In these cases, therefore, there is an increase in the conductor AC resistance with the magnetization of the steel core and not only with the increase in the layers resistance with temperature.

4.4 Improved Prediction of Transmission Line Ampacity

As seen in section 2.4, the *equivalent circuit* model stands out among the others used in calculating the ampacity of conventional steel-cored conductors due to its accuracy. However, it was then shown that calculations using this model for high current/temperature conditions, which can be reached by increasing the current capacity of overhead lines, would require further investigations and developments, which were carried out in this thesis:

- A new electromagnetic model, capable of accurately calculate the resistance of

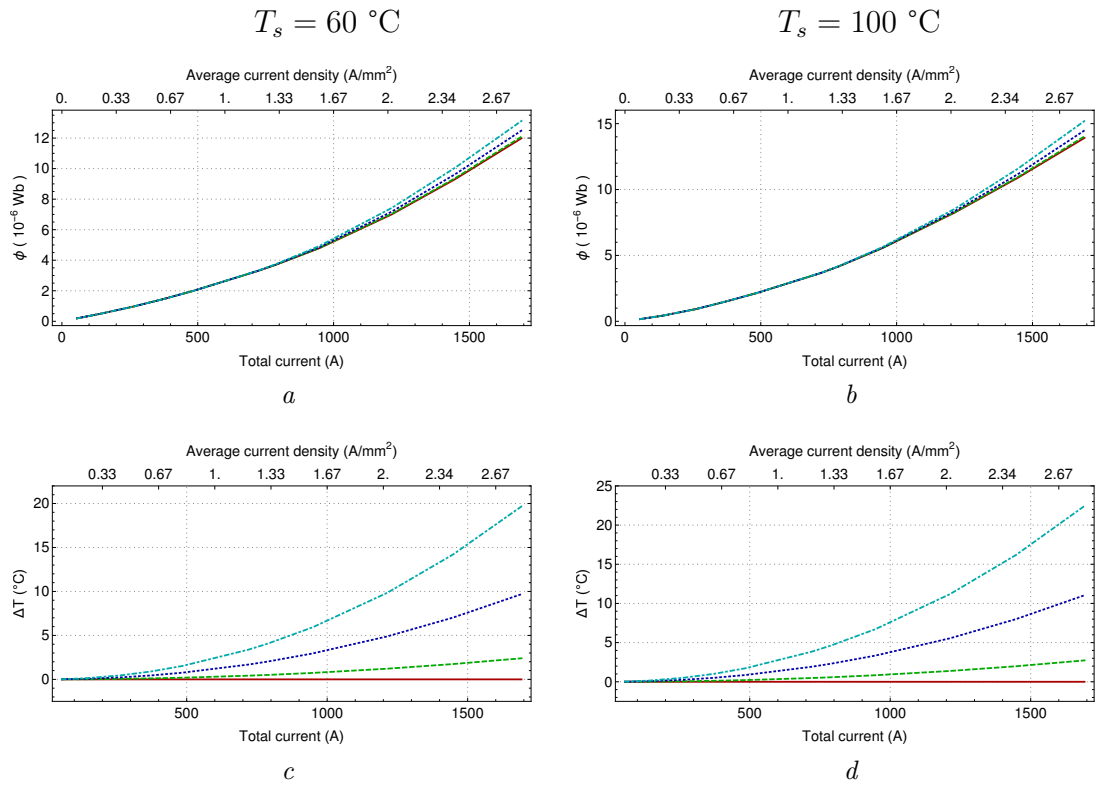

Figure 4.12: Calculated variation of the magnetic flux in the core and radial temperature gradient ΔT with the total current value of an ACSR "*Grackle*" conductor, for conductor surface temperature $T_s = 60$ °C (a) and (c), and $T_s = 100$ °C (b) and (d), considering uniform radial temperature (——) and effective thermal conductivity of 4 W/m °C (- - - -), 1 W/m °C (·····), and 0.5 W/m °C (-·-·-).

steel-cored conductors with one or three aluminum layers up to high current values, proposed in section 4.2;

- A calculation method to consider the steady-state temperature gradient, presented in section 4.3;

- The permeability of an ACSR conductor steel core measured up to a temperature of 230 °C, shown in section 3.2.

To quantify the impact of including these advances in the calculation of conductor ampacity at higher current and temperatures, the ampacity of two thermal resistant aluminum conductors, steel-reinforced (T-ACSR) was calculated: (12/7) "*Guinea*" conductor, of only a single aluminum layer, and (54/19) "*Grackle*" conductor, of three aluminum layers. These conductors can operate up to 150 °C and therefore carry higher current values than conventional ACSR conductors, which can operate up to 90 °C [64].

The AC resistance of these conductors was calculated using the ampacity calculation methodologies of CIGRÉ, IEEE, and the one based on the equivalent circuit

model, proposed in section 2.4. In the latter case, it was used both the equivalent circuit model by Barrett (presented in section 2.3.2) and the model developed in this thesis with the algorithm for including the steady-state radial temperature gradient. For the calculation at higher temperatures, the permeability of the steel core of the ACSR "*Duck*" conductor, measured in section 3.2, was considered. The functions representing the variation of the complex relative permeability with the magnetic field strength for each measured temperature are given in Appendix E.

The ampacity of the conductors was calculated for the following four scenarios: maximum conductor surface temperature of 75 °C and 150 °C, and wind speeds of 0.5 and 1.5 m/s for each temperature. The two scenarios of the maximum temperature of 75 °C correspond to the operating limits of conventional conductors, and the scenarios of maximum temperature of 150 °C correspond to the limits of thermal resistant conductors. It was assumed for the four scenarios the solar radiation of $1000,0$ W/m^2, ambient temperature of 30 °C, average height of line of 650 m, coefficient of emissivity and absorption of the conductor of 0.5.

4.4.1 T-ACSR "*Guinea*" Conductor (one aluminum layer)

The "*Guinea*" conductor analyzed below has one layer of 12 aluminum alloy thermal resistant wires and a steel core of 7 galvanized steel wires. Further details of the conductor are given in Appendix A.3.

The variation of the AC/DC resistance ratio with the total current value, obtained using the equivalent circuit models and the CIGRÉ methodology is shown in Fig. 4.13. The equivalent circuit model proposed by Barrett and developed in this thesis are hereinafter referred to as Eq.Circ.-A and Eq.Circ.-B, respectively. The temperature gradient is disregarded due to the small diameter of the conductor. The AC/DC resistance ratio according to the CIGRÉ methodology was obtained from the DC/AC ampacity conversion, as described in Appendix F.

Results show that the AC/DC resistance ratio values obtained using the equivalent circuit model by Barrett are higher than those obtained using the one developed in this thesis for total current values above 120 A and $T_s = 75$ °C and for current values above 110 A and $T_s = 150$ °C. This occurs because the model by Barrett does not represent the reduction of the core magnetization caused by the magnetic field produced in the steel layers. A similar discrepancy in results was found in section 4.2.2, for the modified "*Grackle*" conductor, with only one aluminum layer. The use of Barrett's model, therefore, tends to overestimate the AC resistance of steel-cored conductors with a single aluminum layer.

The AC/DC resistance ratio obtained considering the conversion of the ampacity proposed by the CIGRÉ methodology, in turn, represents the increase in resistance

with the current carried only up to the current value of 300 A, remaining constant for higher current values. As discussed in section2.4.6, these DC/AC conversions correspond to a specific case (a specific conductor, under certain operating conditions), and may not represent the variation of the analyzed conductor. Fig. 4.13 shows that this AC/DC resistance ratio is close to that obtained by the equivalent circuit models only up to 210 A for T_s = 75 °C and up to 130 A for T_s = 150 °C. Above these values, the variation of the AC/DC resistance ratio with the total current value is much lower than that obtained by other models, remaining constant for current values greater than 300 A and, therefore, clearly inaccurate.

Following the IEEE methodology, tabulated values of conductor resistance provided by a manufacturer [64] were considered, as follows: $R_{dc,20°C}$ = 367 $\mu\Omega$/m, $R_{ac,75°C}$ = 447 $\mu\Omega$/m, and $R_{ac,150°C}$ = 557 $\mu\Omega$/m. Corresponding to the AC/DC resistance ratio of 0.997 at 75 °C and 0.995 at 150 °C. It is important to highlight that using such tabulated values, it is assumed a constant resistance value over the entire current range. However, Fig. 4.13 shows how strongly the AC resistance varies with the total current value and, therefore, assuming a constant value is not an appropriate approach.

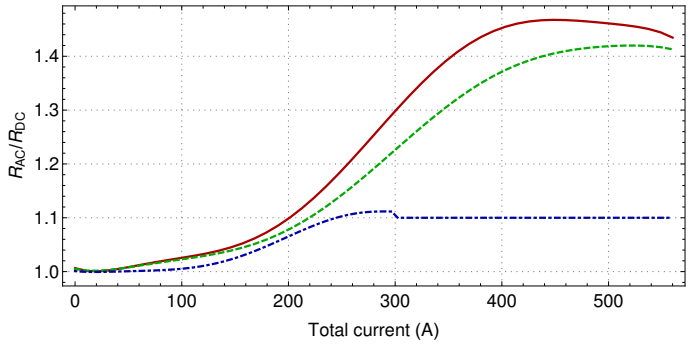

a

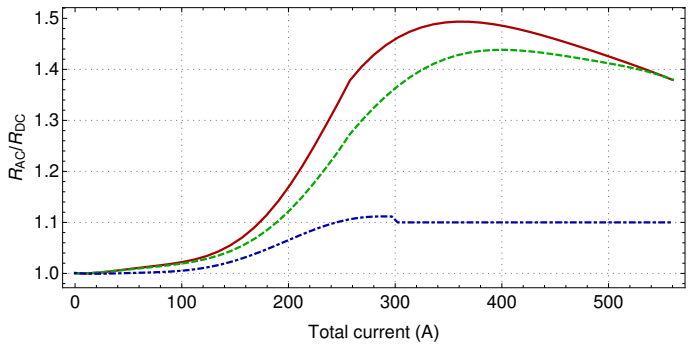

b

Figure 4.13: Variation of the AC/DC resistance ratio with the total current value of an T-ACSR "*Guinea*" conductor calculated using the methodology of CIGRÉ (·····), and equivalent circuit model proposed by Barrett in [15] (——), and developed in this thesis (- - - -), for the temperature on the conductor surface of 75 °C (*a*) and 150 °C (*b*).

The calculated ampacities are given in Table 4.4. The deviation of each method in relation to the equivalent circuit model developed in this thesis (Eq.Circ.-B), which proved to have good accuracy over a wide current range, is given in Table 4.5. Results show that the ampacity calculated with the IEEE methodology is always higher than the others. This is caused by the use of tabulated values of the conductor AC resistance, which do not vary with the current carried and are lower than the values calculated by other methodologies. The opposite is seen in the ampacity obtained using the equivalent circuit proposed by Barrett (Eq.Circ.-A), by which the highest resistance values among the other models are obtained. The calculated ampacities using the CIGRÉ methodology and those based on the equivalent circuit model are close only for the temperature of 75 °C and low wind intensity, since in this case, the conductor ampacity is less than 300 A, and the AC/DC resistance ratios obtained by the models are very close to each other (see Fig. 4.13(a)). For a greater intensity of wind and temperature, for which there is a greater ampacity, there is also a greater divergence of values, due to the difference in AC/DC resistance ratios obtained by the models.

It should be highlighted the large discrepancy obtained using the methodology of CIGRÉ and IEEE, reaching the high values of 65.0 A and 92.5 A, respectively, for the temperature of 150 °C and wind intensity of 1.5 m/s. Even at a temperature of 75 °C and a wind intensity of 1.5 m/s, which corresponds to the operating limit of conventional conductors, the deviations found are significant. These high values mean that the use of these methods overestimates the operational capacity of the line, strongly increasing the risk of accidents caused by overheating.

Table 4.4: Ampacity of the T-ACSR "*Guinea*" conductor, calculated for different scenarios

T(°C)	v (m/s)	Ampacity (A)			
		CIGRÉ	IEEE	Eq.Circ.-A	Eq.Circ.-B
75	0.5	267.7	282.2	257.0	261.6
	1.5	346.4	363.9	315.0	323.0
150	0.5	435.9	458.1	374.2	381.5
	1.5	541.3	568.9	472.4	476.4

4.4.2 T-ACSR "*Grackle*" Conductor (three aluminum layers)

The T-ACSR "*Grackle*" conductor analyzed below has the same physical dimensions as the ACSR "*Grackle*" conductor previously studied in section 4.3.3 and

Table 4.5: Ampacity deviation of the T-ACSR "*Guinea*" conductor, in relation to Eq.Circ.-B, for different scenarios

T(°C)	v (m/s)	Deviation of Ampacity (A)		
		CIGRÉ	IEEE	Eq.Circ.-A
75	0.5	6.1	20.7	−4.6
	1.5	23.5	40.9	−8.0
150	0.5	54.5	76.7	−7.3
	1.5	65.0	92.5	−4.0

described in Appendix A.2. The electrical characteristics of its steel and aluminum wires, however, differ from the conventional ACSR "*Grackle*" conductor. The electrical resistivity of the steel and aluminum wires of the T-ACSR conductor at 20 °C, following [64], are 0.19157 Ω mm^2/m and 0.028736 Ω mm^2/m, respectively.

The conductor AC resistance was calculated using the methodologies of CIGRÉ [28], IEEE with multiplier factors proposed in [25] and [14], referred to below by IEEE-A and IEEE-B, respectively, and using the equivalent circuit model proposed by Barrett (Eq.Circ.-A) and the one developed in this thesis (Eq.Circ.-B). In the latter case, it was considered the radial temperature gradient and the effective thermal conductivity of 0.6 W/m °C, which was used in the application example in section 4.3.3. The calculation was performed considering a fixed temperature T_s on the conductor surface. The variations of the AC/DC resistance ratio with the total current value, obtained for temperatures T_s of 75 °C and 150 °C, are shown in Fig. 4.14.

Results show a stronger increase in resistance with the total current value when considering the temperature gradient in the equivalent circuit model (Eq.Circ.-B), as seen in Fig. 4.11. The result obtained using the Eq.Circ.-A model is very close to that using the CIGRÉ methodology but, as stated before, the curve used by the latter represents a specific case (ACSR "*Zebra*" conductor, at 50 Hz and unknown temperature). In this example, the curve coincided with the results obtained by the Eq.Circ.-A model but not in the other cases analyzed in this thesis (see Fig. 2.13 and Fig. 2.14). The resistance values calculated by the IEEE-A method are higher than those obtained by the other methods in almost any current range analyzed, thus confirming its conservative characteristic, since higher resistance values correspond to lower ampacities. Only at high values of total current (above 2000 A for T_s = 75 °C and above 1500 A for T_s = 150 A), the results obtained by the IEEE-A model are overcome by those of the Eq.Circ.-B, which has a strong increase in resistance

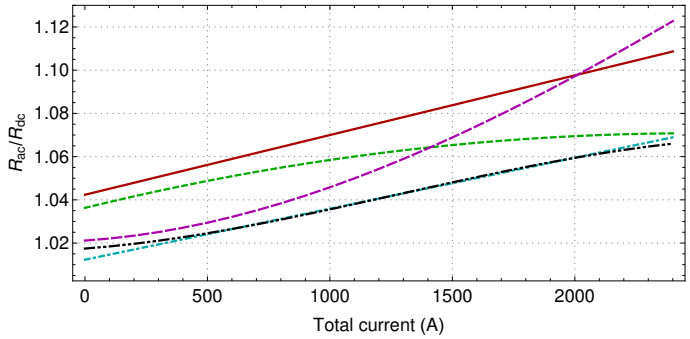

a

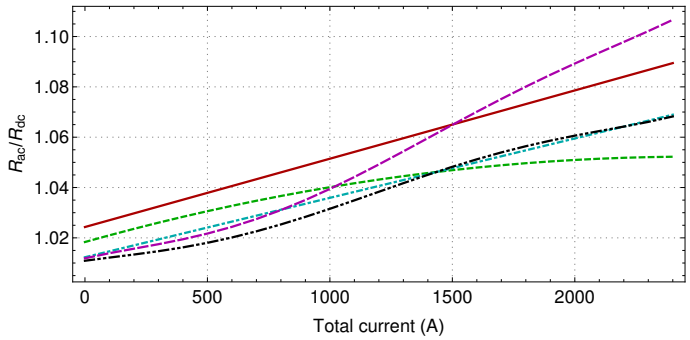

b

Figure 4.14: Variation of the AC/DC resistance ratio with the total current value of a T-ACSR "*Grackle*" conductor calculated using the methodology of CIGRÉ (------), IEEE-A (——), IEEE-B (-----) and equivalent circuit model proposed by Barrett in [15] (-·-·-), and developed in this thesis (– – –) for the conductor surface temperature of 75 °C (*a*) and 150 °C (*b*).

due to the temperature gradient.

Furthermore, it should be noted that the AC/DC resistance ratio curves obtained using the IEEE methodology depend on the conductor nominal area (determining the slope of the curve) and the tabulated resistance values (determining the vertical position), and that the latter may vary significantly from manufacturer to manufacturer. Values from different technical catalogs were tested and most of them provided extremely high AC/DC resistance ratios, resulting in the shift of the curves to values far from those obtained from other models and could not be used in the IEEE methodology.

The ampacity values and temperature gradients calculated for each scenario are shown in Table 4.6. The deviation of each method in relation to the equivalent circuit model developed in this thesis (Eq.Circ-B), which considers the radial temperature gradient, is given in Table 4.7. Results show that, for the temperature on the conductor surface of 75 °C, which corresponds to the operating limit of conventional conductors, no significant deviations were found, due to the proximity of the AC/DC resistance ratios obtained by the models (see Fig. 4.14(a)). The results obtained by the IEEE methodology in this scenario are more conservative, as seen in the

application example presented in section 2.4.6.

For $T_s = 150$ °C, however, the ampacity values obtained by the Eq.Circ.-B model become smaller than the others. This occurs due to the increase in the conductor's ampacity with increasing temperature, moving to a range of current values in which the resistance obtained using the Eq.Circ.-B are higher than the others. In this scenario, there is a relevant change to be highlighted: the IEEE method is no longer conservative and, furthermore, IEEE-B becomes the largest. In addition, the differences between results obtained by Eq.Circ.-B with Eq.Circ-A become significant, due to the greater increase in resistance with the total current value obtained by Eq.Circ-B by considering the temperature gradient.

Although the ampacity deviations obtained are not as significant as in the case of the "*Guinea*" conductor, the results show the importance of considering the temperature gradient, in order to avoid overestimation of the line ampacity and to reduce the risk of accidents due to its overheating.

Table 4.6: Ampacity of the T-ACSR "*Grackle*" conductor, calculated for different scenarios

T_s (°C)	v (m/s)	Ampacity (A)					ΔT (°C)
		CIGRÉ	IEEE-A	IEEE-B	Eq.Circ.-A	Eq.Cir.-B	
75	0.5	930.7	916.0	920.6	930.8	926.8	5.0
	1.5	1190.0	1170.9	1178.3	1190.1	1182.6	8.2
150	0.5	1570.6	1558.1	1572.1	1570.1	1557.1	18.0
	1.5	1908.2	1892.3	1914.8	1907.3	1884.9	26.8

Table 4.7: Deviation of the ampacity of the T-ACSR "*Grackle*" conductor, in relation to Eq.Circ.-B, for different scenarios

T_s (°C)	v (m/s)	Ampacity (A)			
		CIGRÉ	IEEE-A	IEEE-B	Eq.Circ.-A
75	0.5	3.9	−10.8	−6.2	4.0
	1.5	7.4	−11.7	−4.3	7.5
150	0.5	13.5	0.9	15.0	13.0
	1.5	23.3	7.4	29.9	22.4

Chapter 5

Conclusions

This thesis presents a study on the effects of the core magnetization of steel-cored conductors on their resistance and current distribution, on their calculation models, and the use of these models in evaluating the ampacity of such conductors, especially with regard to the possibility of increasing their current carrying capacity. The steel core is magnetized when the conductor has an odd number of aluminum layers, resulting in losses due to hysteresis and eddy currents, affecting the conductor AC resistance. If the conductor has three aluminum layers, magnetization of the core also causes a redistribution of current between its aluminum layers, known as the *transformer effect*, which affects the conductor transient internal temperature and its AC resistance. The intensity of the core magnetization depends on the current carried by the conductor, as well as on the frequency, and the steel core permeability, which varies with tensile stress and temperature.

Despite the complexity of the phenomenon, the effect of steel core magnetization on the three-layer conductor resistance is traditionally accounted for in a simplified way, using *multiplying factors* only, depending on the value of the current carried by the conductor. This approach is used in the two main methodologies for calculating the ampacity of overhead lines (from CIGRÉ and IEEE). However, the AC resistance variation and current redistribution caused by the steel core magnetization can be calculated using an *equivalent circuit* modeling approach, which allows to consider the different factors affecting the phenomenon. Such modeling can also be used to optimize the conductors' design in order to reduce their losses related to the core magnetization.

In the chapter 2, the use of an *equivalent circuit* model was proposed in the ampacity calculation of steel-cored conductors, and then an application example was performed, in which the ampacity of a three-layer ACSR "*Grackle*" conductor was calculated using the proposed model and compared with those used in the main methodologies for ampacity calculation (CIGRÉ and IEEE) and in the current Brazilian methodology. The results showed that the Brazilian calculation standard

does not represent the increase in the conductor resistance with the carried current, which is caused by the core magnetization. Overestimating the line ampacity results into greater risks when using the Brazilian standard. The methodology proposed by CIGRÉ, in turn, represents the resistance variation of a specific conductor (ACSR "*Zebra*" at 50 Hz), and should be used only for this case. The IEEE methodology admits two different multiplier factors, the factor from [50] being conservative (providing higher resistance values) and the other, from [14], obtaining results closer to those calculated by the *equivalent circuit* model, which stands out among the other models for its accuracy and for being able to consider the various aspects that affect the steel core magnetization. The method used in the IEEE methodology is, therefore, a satisfactory option in the absence of further details of the conductor and its steel core.

The use of an *equivalent circuit* model requires further knowledge of the conductor's characteristics and the magnetic properties of its steel core for any temperature and tensile stress within the range of possible operating conditions. Although the magnetic properties of this type of steel are known up to 150 °C, which even exceeds the maximum emergency overload temperatures of conventional conductors, steel-cored conductors with annealed aluminum wires may operate at a temperature up to 200 °C and therefore the magnetic properties in this higher temperature range need to be investigated. Therefore, an experimental work was carried out to investigate the properties of the steel core of an ACSR "*Duck*" conductor at temperatures from 40 to 230 °C.

Furthermore, to the best of the author's knowledge, in the only report found in the literature in which the current redistribution due to the steel core magnetization was experimentally observed, only the current density on the surface of a randomly selected wire of each layer was measured, each wire of the conductor was unwrapped for the probes installation and the conductor heating was avoided. The effect of increasing temperature on current density redistribution was not measured but only calculated in [17]. An experimental arrangement was then developed for the simultaneous measurement of the current in each of the aluminum wires of a three-layer ACSR "*Duck*" conductor, modifying it by only 5.7% of its length and observing the effect of the conductor heating until the temperature on its surface reached 200 °C.

The experimental study were presented in chapter 3. The results obtained on the steel core showed two distinct behaviors of its magnetic properties with increasing temperature: one up to 130 °C and another above 160 °C. While results at temperatures up to 130 °C are similar to those found in previous studies, the change in the magnetic properties behavior above 160 °C results into an unexpected hump-shaped variation of the permeability with temperature, in a range of magnetic field strength

from 1.0 to 2.4 kA/m, with maximum permeability values occurring at a temperature from 150 °C to 170 °C. The presence of these maximum permeability values in the steel used in conductor cores has not been reported before but they are also found in other magnetic materials such as ferrites, occurring when the anisotropy of the material goes through zero.

Results on the ACSR "*Duck*" conductor showed that the variation of current density among conductors of the same layer is small, with the standard deviation being less than 1.5% of the layer mean value for all total current values and temperatures analyzed. The concentration of current density in the middle layer due to the transformer effect was also observed, increasing with the total current value as expected. The total current being held constant, the current density distribution was modified during the conductor heating due to the increase of the internal magnetic flux with the temperature and the presence of a radial temperature difference between the steel core and the conductor surface. This radial temperature gradient is expected at high current density but has not been considered in previous computational models. The effect of the temperature gradient on the current density distribution is more pronounced than that of the magnetic flux increase with the temperature and therefore must be considered. Results also showed that, for total current intensities from 1000 A up to 2300 A, the variation of the magnetic flux in the core with increasing conductor temperature also presents a hump shape, with a maximum value occurring at increasing temperatures with the increase of the total current value, similar to the permeability behavior observed experimentally. The decrease in magnetic flux after reaching its maximum value, in turn, weakens the transformer effect, modifying the expected variation of current density distribution with increasing conductor temperature.

Chapter 4 presented a new electromagnetic model for calculating the AC resistance and current distribution of steel-cored conductors. The model was developed in order to refine the representation of the steel core and overcome the limitations observed in the existing models, which are not accurate at high currents when used for conductors with a single aluminum layer, and their use for optimizing the conductors' design is limited to changes in the aluminum layers only. Experimental data from a steel-cored conductor with three and a single aluminum layer were used to validate and compare the new model with previous ones, and its accuracy was verified over the whole current range for both conductors. Results showed that the magnetic field produced in the steel layers can contribute to the reduction of the core magnetization. This is only represented in the new model and is the cause of the discrepancy previously observed for the conductor with a single aluminum layer. Furthermore, it was shown that the new model can be used to investigate further reduction of the losses (both in single and three aluminum layer conductors)

by changing the design of the steel core, while keeping the steel cross-section area. This reduction is even more important for conductors with a single aluminum layer since they have higher losses due to the core magnetization.

A calculation algorithm to include the steady-state radial temperature gradient in the new electromagnetic model was also presented in chapter 4. The effect of this temperature gradient on the current distribution and AC resistance of steel-cored conductors was then analyzed in application examples. Results showed a current redistribution similar to that observed experimentally when considering the radial temperature gradient in the calculations, confirming the analysis of experimental results. Results also showed that when considering a given temperature value on the conductor surface, which should be considered for the ampacity calculations, the increase in resistance with the total current value is stronger with the temperature gradient, due to the greater heating of the inner layers and the consequent increase in each layer resistance. It was seen that in this case, there is also the strengthening of the core magnetization with the temperature gradient, caused by the increase of temperature in the steel core and the dependence of the steel permeability on temperature.

Chapter 4 then presented application examples in which the ampacity of thermal resistant aluminum conductors, steel reinforced (T-ACSR) are calculated up to high currents/temperatures using the measured variation of steel core permeability up to 230 °C, the new electromagnetic model and its calculation considering the steady-state radial temperature gradient, and compared with those used in the CIGRÉ and IEEE methodologies, and with the one based on the existing *equivalent circuit* model. In the case of the T-ACSR conductor with a single aluminum layer, results showed that the line's ampacity tends to be underestimated using the existing *equivalent circuit* model and severely overestimated by the IEEE and CIGRÉ methodology even for conventional conductor operating limits. The electromagnetic model developed in this thesis, in turn, offers more reliable ampacity predictions, as it shows good accuracy with experimental results up to high current values. The high discrepancy obtained using the IEEE and CIGRÉ methodologies is no longer observed for the case of the T-ACSR conductor with three aluminum layers. However, it was seen with the improved model that the temperature gradient, in this case, causes the conductor resistance to increase more intensely with the total current value than that obtained with the other models, which therefore tend to overestimate the line's ampacity for the high operating limit reached by improved current capacity conductors, such as the analyzed T-ACSR.

5.1 Future Work

Considering the study conducted in this thesis and its outcomes, the following future works are proposed:

- Measure the magnetic properties of steel cores of other mechanical strength (high, extra, and ultra-high-strength), which have a different chemical composition than the one studied in this thesis (of regular strength), for the same expanded temperature range analyzed.
- Develop a calculation algorithm to include the conductor internal transient temperature in the electromagnetic model.
- Compare the temperature on the surface of steel-cored conductors calculated using the different AC resistance calculation models with measured values or monitoring data.
- Develop a method for estimating conductor physical parameters and magnetic characteristics of steel core using measurement or monitoring data.
- Estimate electrical parameters of overhead lines with steel-cored conductors using monitoring data and analyze their agreement with results obtained by the calculation models.

References

[1] KIM, S. D., MORCOS, M. M. "An Application of Dynamic Thermal Line Rating Control System to Up-Rate the Ampacity of Overhead Transmission Lines", *IEEE Transactions on Power Delivery*, v. 28, n. 2, pp. 1231–1232, apr 2013. doi: 10.1109/tpwrd.2012.2234940.

[2] BLACK, C. R., CHISHOLM, W. A. "Key Considerations for the Selection of Dynamic Thermal Line Rating Systems", *IEEE Transactions on Power Delivery*, v. 30, n. 5, pp. 2154–2162, oct 2015. doi: 10.1109/tpwrd.2014.2376275.

[3] MICHIORRI, A., NGUYEN, H.-M., ALESSANDRINI, S., et al. "Forecasting for dynamic line rating", *Renewable and Sustainable Energy Reviews*, v. 52, pp. 1713–1730, dec 2015. doi: 10.1016/j.rser.2015.07.134.

[4] WALLNERSTROM, C. J., HUANG, Y., SODER, L. "Impact From Dynamic Line Rating on Wind Power Integration", *IEEE Transactions on Smart Grid*, v. 6, n. 1, pp. 343–350, jan 2015. doi: 10.1109/tsg.2014.2341353.

[5] DOUGLASS, D., CHISHOLM, W., DAVIDSON, G., et al. "Real-Time Overhead Transmission-Line Monitoring for Dynamic Rating", *IEEE Transactions on Power Delivery*, v. 31, n. 3, pp. 921–927, jun 2016. doi: 10.1109/tpwrd.2014.2383915.

[6] DAWSON, L., KNIGHT, A. M. "Applicability of Dynamic Thermal Line Rating for Long Lines", *IEEE Transactions on Power Delivery*, v. 33, n. 2, pp. 719–727, apr 2018. doi: 10.1109/tpwrd.2017.2691671.

[7] DAVIS, M. "A new thermal rating approach: The real time thermal rating system for strategic overhead conductor transmission lines – Part I: General description and justification of the real time thermal rating system", *IEEE Transactions on Power Apparatus and Systems*, v. 96, n. 3, pp. 803–809, may 1977. doi: 10.1109/t-pas.1977.32393.

[8] SWATEK, D. R. “An expected per-unit rating for overhead transmission lines”, *International Journal of Electrical Power & Energy Systems*, v. 26, n. 4, pp. 241–247, may 2004. doi: 10.1016/j.ijepes.2003.10.003.

[9] KHAKI, M., MUSILEK, P., HECKENBERGEROVA, J., et al. “Electric power system cost/loss optimization using Dynamic Thermal Rating and linear programming”. In: *2010 IEEE Electrical Power & Energy Conference*. IEEE, aug 2010. doi: 10.1109/epec.2010.5697195.

[10] ADAMS, H. “Steel Supported Aluminum Conductors (SSAC) for Overhead Transmission Lines”, *IEEE Transactions on Power Apparatus and Systems*, v. PAS-93, n. 5, pp. 1700–1705, sep 1974. doi: 10.1109/tpas.1974.293903.

[11] THRASH, F. “ACSS/TW-an improved conductor for upgrading existing lines or new construction”. In: *1999 IEEE Transmission and Distribution Conference (Cat. No. 99CH36333)*, v. 2, pp. 852–857 vol.2. IEEE, 1999. doi: 10.1109/tdc.1999.756161.

[12] ALAWAR, A., BOSZE, E., NUTT, S. “A Composite Core Conductor for Low Sag at High Temperatures”, *IEEE Transactions on Power Delivery*, v. 20, n. 3, pp. 2193–2199, jul 2005. doi: 10.1109/tpwrd.2005.848736.

[13] TAMM, C. “Application dynamics of high temperature conductors in suspension clamps”. In: *2003 IEEE PES Transmission and Distribution Conference and Exposition (IEEE Cat. No.03CH37495)*. IEEE. doi: 10.1109/tdc.2003.1335046.

[14] *Aluminum Electrical Conductor Handbook*, 3rd ed. The Aluminum Association, New York, 1989.

[15] BARRETT, J. S., NIGOL, O., FEHERVARI, C. J., et al. “A New Model of AC Resistance in ACSR Conductors”, *IEEE Transactions on Power Delivery*, v. 1, n. 2, pp. 198–208, 1986. doi: 10.1109/tpwrd.1986.4307951.

[16] MORGAN, FINDLAY, ZHANG, B. “Distribution of current density in ACSR conductors”. In: *Proceedings of Canadian Conference on Electrical and Computer Engineering CCECE-94*. IEEE, 1994. doi: 10.1109/ccece.1994.405636.

[17] MORGAN, V., ZHANG, B., FINDLAY, R. “Effect of magnetic induction in a steel-cored conductor on current distribution, resistance and power loss”, *IEEE Transactions on Power Delivery*, v. 12, n. 3, pp. 1299–1308, jul 1997. doi: 10.1109/61.637007.

[18] MORGAN, V. T. "The Current Distribution, Resistance and Internal Inductance of Linear Power System Conductors—A Review of Explicit Equations", *IEEE Transactions on Power Delivery*, v. 28, n. 3, pp. 1252–1262, jul 2013. doi: 10.1109/tpwrd.2012.2213617.

[19] ABSI SALAS, F. M., ORLANDE, H. R. B., DOMINGUES, L. A. M. C. "Thermal Characterization of a Transmission Line Cable". In: *4th Inverse Problems, Design and Optimization Symposium - IPDO-2013*, Albi, France, 2013.

[20] ABSI SALAS, F. M., ORLANDE, H. R. B., DOMINGUES, L. A. M. C. "Parameter Estimation in Heat Transfer through an Overhead Power Cable by Using the Markov Chain Monte Carlo Method", *High Temperatures – High Pressures*, v. 44, n. 4, pp. 317–336, jul. 2015.

[21] ABSI SALAS, F. M., ORLANDE, H. R. B., DOMINGUES, L. A. M. C. "Temperature Measurements in an Overhead Electric Power Cable". In: *8th World Conference on Experimental Heat Transfer, Fluid Mechanics and Thermodynamics*, Lisbon, Portugal, 2013.

[22] MORGAN, V., ZHANG, B., FINDLAY, D. "Effects of temperature and tensile stress on the magnetic properties of a steel core from an ACSR conductor", *IEEE Transactions on Power Delivery*, v. 11, n. 4, pp. 1907–1913, 1996. doi: 10.1109/61.544275.

[23] MORGAN, V., FINDLAY, R. "The effect of frequency on the resistance and internal inductance of bare ACSR conductors", *IEEE Transactions on Power Delivery*, v. 6, n. 3, pp. 1319–1326, jul 1991. doi: 10.1109/61.85881.

[24] MORGAN, V. "Effects of alternating and direct current, power frequency, temperature, and tension on the electrical parameters of acsr conductors", *IEEE Transactions on Power Delivery*, v. 18, n. 3, pp. 859–866, jul 2003. doi: 10.1109/tpwrd.2003.813601.

[25] HOWINGTON, B. S., RATHBUN, L. S., DOUGLASS, D. A. "AC Resistance of ACSR - Magnetic and Temperature Effects Prepared by a Task Force of the Working Group on Calculation of Bare Overhead Conductor Temperatures", *IEEE Power Engineering Review*, v. PER-5, n. 6, pp. 67–68, jun 1985. doi: 10.1109/mper.1985.5526666.

[26] *AC Transmission Line Reference Book: 200 kV and Above*, 3rd ed. Electric Power Research Institute, Palo Alto, CA, USA, 2005.

[27] "IEEE Standard for Calculating the Current-Temperature Relationship of Bare Overhead Conductors". IEEE Std 738–2012, 2013. pp.1–72.

[28] CIGRÉ WG 22.12. *The thermal behaviour of overhead conductors. Sections 1 and 2.* ELECTRA, No. 144, out. 1992.

[29] AGÊNCIA NACIONAL DE ENERGIA ELÉTRICA (ANEEL). Nota Técnica SRT 38/2005, nov. 2005.

[30] DOUBLE, E. "Distribution of tensile load in relation to temperature and sag of steel-cored aluminium conductors", *Journal of the Institution of Electrical Engineers - Part I: General*, v. 92, n. 58, pp. 399–400, oct 1945. doi: 10.1049/ji-1.1945.0107.

[31] MATSCH, L. W., LEWIS, W. A. "The Magnetic Properties of ACSR Core Wire", *Transactions of the American Institute of Electrical Engineers. Part III: Power Apparatus and Systems*, v. 77, n. 3, pp. 1178–1189, apr 1958. doi: 10.1109/aieepas.1958.4500121.

[32] MORGAN, V., PRICE, C. "Magnetic properties in axial 50 Hz fields of steel core wire for overhead-line conductors", *Proceedings of the Institution of Electrical Engineers*, v. 116, n. 10, pp. 1681, 1969. doi: 10.1049/piee.1969.0305.

[33] RIAZ, H. "Magnetic Properties of ACSR core wire over an extended temperature range". In: *Proc. Inter. Electrical and Electronics Conf.*, pp. 682–685, 1983.

[34] ASTM B856–18. "Standard Specification for Concentric-Lay-Stranded Aluminum Conductors, Coated Steel Supported (ACSS)". ASTM International, 2018.

[35] LEWIS, W. A., TUTTLE, P. D. "The Resistance and Reactance of Aluminum Conductors, Steel Reinforced", *Transactions of the American Institute of Electrical Engineers. Part III: Power Apparatus and Systems*, v. 77, n. 3, pp. 1189–1214, apr 1958. doi: 10.1109/aieepas.1958.4500122.

[36] MORGAN, V. "Electrical characteristics of steel-cored aluminium conductors", *Proceedings of the Institution of Electrical Engineers*, v. 112, n. 2, pp. 325, 1965. doi: 10.1049/piee.1965.0051.

[37] BARRETT, J. "Optimization of conductor design", *IEEE Transactions on Power Delivery*, v. 4, n. 1, pp. 453–464, 1989. doi: 10.1109/61.19236.

[38] DOUGLASS, D. A. "Radial and Axial Temperate Gradients in Bare Stranded Conductor", *IEEE Transactions on Power Delivery*, v. 1, n. 2, pp. 7–15, 1986. doi: 10.1109/tpwrd.1986.4307928.

[39] DWIGHT, H. B. "Skin effect and proximity effect in tubular conductors", *Journal of the American Institute of Electrical Engineers*, v. 41, n. 3, pp. 203–209, mar 1922. doi: 10.1109/joaiee.1922.6593266.

[40] MANNEBACK, C. "An Integral Equation for Skin Effect in Parallel Conductors", *Journal of Mathematics and Physics*, v. 1, n. 3, pp. 123–146, apr 1922. doi: 10.1002/sapm192213123.

[41] ARNOLD, A. "Proximity effect in solid and hollow round conductors", *Journal of the Institution of Electrical Engineers - Part I: General*, v. 88, n. 9, pp. 343–344, sep 1941. doi: 10.1049/ji-1.1941.0077.

[42] SCHELKUNOFF, S. A. "The Electromagnetic Theory of Coaxial Transmission Lines and Cylindrical Shields", *Bell System Technical Journal*, v. 13, n. 4, pp. 532–579, oct 1934. doi: 10.1002/j.1538-7305.1934.tb00679.x.

[43] FINDLAY, R., LIU, F. "Experiments on Single Layer ACSR Conductors". In: *2006 12th Biennial IEEE Conference on Electromagnetic Field Computation*. IEEE. doi: 10.1109/cefc-06.2006.1633096.

[44] MEYBERG, R. A. *Identificação da Distribuição de Corrente Interna de Cabos Condutores com Alma de Aço*. Dissertação de mestrado, Universidade Federal do Rio de Janeiro, COPPE/UFRJ, Rio de Janeiro, RJ, Brasil, 2016.

[45] S. V. KULKARNI, S. A. K. *Transformer Engineering: Design, Technology, and Diagnostics, Second Edition*. CRC PR INC, 2012. ISBN: 1439853770.

[46] ZHAO, H., RAGUSA, C., APPINO, C., et al. "Energy Losses in Soft Magnetic Materials Under Symmetric and Asymmetric Induction Waveforms", *IEEE Transactions on Power Electronics*, v. 34, n. 3, pp. 2655–2665, mar 2019. doi: 10.1109/tpel.2018.2837657.

[47] FIORILLO, F. "Measurements of magnetic materials", *Metrologia*, v. 47, n. 2, pp. S114–S142, mar 2010. doi: 10.1088/0026-1394/47/2/s11.

[48] BERTOTTI, G., MAYERGOYZ, I. D. *The science of hysteresis: Hysteresis in materials*, v. 3. Gulf Professional Publishing, 2006.

[49] ZABORSZKY, J. "Skin and Spiraling Effect in Stranded Conductors [includes discussion]", *Transactions of the American Institute of Electrical Engineers. Part III: Power Apparatus and Systems*, v. 72, n. 2, jan 1953. doi: 10.1109/aieepas.1953.4498672.

[50] THRASH, R. *Overhead conductor manual*. Carrollton, Ga, Southwire, 2007. ISBN: 0979142709.

[51] PRICE, C. F., GIBBON, R. R. "Statistical approach to thermal rating of overhead lines for power transmission and distribution", *IEE Proceedings C - Generation, Transmission and Distribution*, v. 130, n. 5, pp. 245–256, set. 1983. ISSN: 0143-7046. doi: 10.1049/ip-c.1983.0047.

[52] AGÊNCIA NACIONAL DE ENERGIA ELÉTRICA (ANEEL). Resolução Normativa 191/2005, Agência Nacional de Energia Elétrica - ANEEL, dez. 2005.

[53] WOHLFARTH, E. P., BUSCHOW, K. H. J. *Handbook of magnetic materials*, v. 2. Elsevier, 1986.

[54] SIMSA, Z., ZOUNOVA, F., BRABERS, V. "Magnetic permeability behaviour in single crystal Mn-ferrites", *IEEE Transactions on Magnetics*, v. 24, n. 2, pp. 1841–1843, mar 1988. doi: 10.1109/20.11620.

[55] ROESS, E. "Soft magnetic ferrites and applications in telecommunication and power converters", *IEEE Transactions on Magnetics*, v. 18, n. 6, pp. 1529–1534, nov 1982. doi: 10.1109/tmag.1982.1062068.

[56] LÓPEZ-FERNÁNDEZ, X. M., ERTAN, H. B., TUROWSKI, J. *Transformers: analysis, design, and measurement*. CRC Press, 2012.

[57] AMORIM, H. P., CARVALHO, A. T. D., RODRIGUES, T. B., et al. "On-site measurements of Partial Discharges through tap of the bushings – Brazilian experience in power transformers". In: *2013 IEEE International Conference on Solid Dielectrics (ICSD)*. IEEE, jun 2013. doi: 10.1109/icsd.2013.6619767.

[58] CARVALHO, A. T., AMORIM, H. P., CUNHA, C. F. C., et al. "Virtual instrumentation for Partial Discharge monitoring". In: *2017 IEEE Electrical Insulation Conference (EIC)*. IEEE, jun 2017. doi: 10.1109/eic.2017.8004640.

[59] FINDLAY, R. D., RIAZ, H. "An Analysis of the Jarvis Crossing AACSR Conductor". In: *IEEE Winter Power Meeting*, 1972.

[60] FINDLAY, R. D. "Analysis of Two Layer Aluminum Conductor Steel Reinforced". In: *IEEE Winter Power Meeting*, 1973.

[61] MORGAN, V. "The thermal rating of overhead-line conductors Part I. The steady-state thermal model", *Electric Power Systems Research*, v. 5, n. 2, pp. 119–139, jun 1982. doi: 10.1016/0378-7796(82)90033-5.

[62] FOSS, S. D., LIN, S. H., CARBERRY, R. "Significance of the Conductor Radial Temperature Gradient within a Dynamic Line Rating Methodology", *IEEE Transactions on Power Delivery*, v. 2, n. 2, pp. 502–511, 1987. doi: 10.1109/tpwrd.1987.4308134.

[63] CIGRÉ WG B2.12. "Thermal Behaviour of Overhead Conductors". Technical Brochure 207, Aug. 2002.

[64] ALUBAR. "Aluminum Electrical Conductors". Technical Catalogue, 2015. Disponível em: <`https://alubar.net.br/img/site/arquivo/Cat_Tec_Alubar_Aluminio_2015.pdf`>.

[65] ASTM B232/B232M–17. "Standard Specification for Concentric-Lay-Stranded Aluminum Conductors, Coated-Steel Reinforced (ACSR)". ASTM International, 2017.

Appendix A

Details of the Steel-Cored Conductors Under Study

A.1 (54/7) "*Duck*" ACSR Conductor

The "*Duck*" ACSR conductor sample, on which the experimental studies presented in chapter 3 were carried out, is made from 54 aluminum 1350-H19 wires and a core of 7 galvanized steel wires. The resistivity of aluminum and steel wires measured at 20 °C are 0.028 $\Omega mm^2/m$ and 0.181 $\Omega mm^2/m$, respectively. The other measured parameters are given in Table A.1 and depicted in half of the conductor cross-section in Fig. A.1.

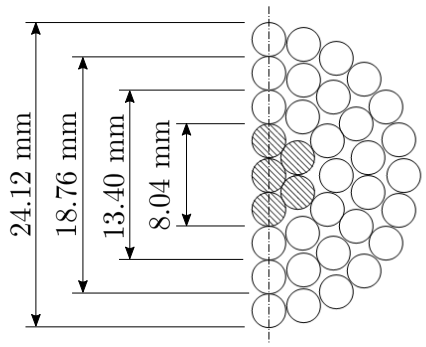

Figure A.1: Half of the cross-section of "*Duck*" conductor with outer diameter of aluminum layers (○) and steel core (▨).

A.2 (54/19) "*Grackle*" ACSR Conductor

The "*Grackle*" ACSR conductor, analyzed in chapters 2 and 4 of this thesis, has 54 aluminum wires and a core of 19 steel wires. Its physical data, measured in [15], are shown in Table A.2 and half of its cross-section is depicted in

Table A.1: Measured Parameters of the ACSR "*Duck*" conductor sample.

	Aluminum layers			Steel core
	Inner	Middle	Outer	
Number of wires	12	18	24	7
Outer diameter (mm)	13.40	18.76	24.12	8.04
Lay length (mm)	178.70	218.0	268.7	201.0
Wire diameter (mm)		2.68		

Fig. A.2. The aluminum and steel wires resistivity at 20 °C are 0.02818 Ω mm^2/m and 0.1775 Ω mm^2/m, respectively.

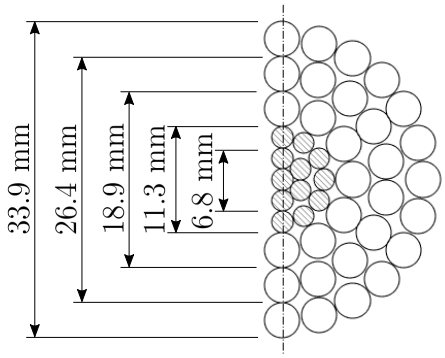

Figure A.2: Half of the cross-section of "*Grackle*" conductor with outer diameter of aluminum layers (○) and steel core (▨).

Table A.2: Parameters of the ACSR "*Grackle*" conductor. [15]

	Aluminum layers			Steel core
	Inner	Middle	Outer	
Number of wires	12	18	24	19
Outer diameter (mm)	18.9	26.4	33.9	11.3
Lay length (mm)	291.6	365.0	410.0	187.4
Wire diameter (mm)		3.77		2.26

A.3 (12/7) "*Guinea*" T-ACSR Conductor

The "*Guinea*" T-ACSR conductor analyzed in chapter 4 has a layer of 12 aluminum alloy thermal resistant wires, and a core of 7 galvanized steel wires. Its

physical data, taken from [64], are given in Table A.3 and half of its cross-section is shown in Fig. A.3. The resistivity of the aluminum and steel wires at 20 °C is 0.028736 Ω mm^2/m and 0.19157 Ω mm^2/m, respectively. The lay length (pitch) of the layers, shown in Table A.3, was calculated according to the corresponding preferred values of lay ratios, following the ASTM standard B232 [65].

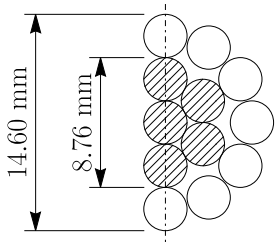

Figure A.3: Half of the cross-section of "*Guinea*" conductor with outer diameter of its aluminum layer (○) and steel core (◍).

Table A.3: Parameters of the T-ACSR "*Guinea*" conductor.

	Aluminum layer	Steel core
Number of wires	12	7
Outer diameter (mm)	14.60	8.76
Lay length (mm)	182.50	219.00
Wire diameter (mm)	2.92	

Appendix B

Calculation of correction factors k_1 and k_2 used in existing equivalent circuit models

For the mathematical formulation of the equivalent circuit model proposed by Barrett *et al.* [15], it is assumed that the current in each aluminum layer is concentrated at its mean radius. In this way, the circular magnetic flux in an aluminum layer i, external and internal to its mean radius would be, respectively,

$$\phi_{i,outer} = \frac{\mu_0}{2\pi}\left(\mathbf{I}_s + \sum_{q=1}^{i}\mathbf{I}_q\right)\ln\frac{D_i}{D_i - d} \tag{B.1}$$

and

$$\phi_{i,inner} = \frac{\mu_0}{2\pi}\left(\mathbf{I}_s + \sum_{q=1}^{i-1}\mathbf{I}_q\right)\ln\frac{D_i - d}{D_{i-1}} \tag{B.2}$$

where D_i is outer diameter of the layer i, d is the diameter of the wire in this layer, and μ_0 is the permeability of free space. $\mathbf{I}_s$ and $\mathbf{I}_q$ are the current in the steel core and in the q-th aluminum layer, respectively.

Note in (B.1) and (B.2) that the current in layer i, $\mathbf{I}_i$, produces a circular flux only outside itself and, therefore, outside the mean radius of the layer. However, as the current is not concentrated at the layer mean radius, the contribution of $\mathbf{I}_i$ to the value of $\phi_{i,outer}$ is overestimated, and its contribution to the value of $\phi_{i,inner}$ is erroneously disregarded. This is corrected in the existing models [15, 16] by means of correction factors k_1 and k_2, representing the contribution of the current in a layer to the circular flux internal and external to this layer mean radius, respectively. Using

these factors, (B.1) and (B.2) are rewritten as follows:

$$\phi_{i,outer} = \frac{\mu_0}{2\pi}\left(\mathbf{I}_s + \sum_{q=1}^{i-1}\mathbf{I}_q + k_1\mathbf{I}_i\right)\ln\frac{D_i}{D_i - d} \tag{B.3}$$

and

$$\phi_{i,inner} = \frac{\mu_0}{2\pi}\left(\mathbf{I}_s + \sum_{q=1}^{i-1}\mathbf{I}_q + k_2\mathbf{I}_i\right)\ln\frac{D_i - d}{D_{i-1}} \tag{B.4}$$

which are used in the models by Barrett *et al.* [15] and Morgan [16], see Section 2.3.2.

k_1 and k_2 for any aluminum layer of an ACSR "*Grackle*" conductor, calculated in [15], are 0.79 and 0.21, respectively. The formulation used for this calculation, however, is not presented by its authors. In [16], different values of k_1 and k_2 are calculated for the aluminum layers of the same "*Grackle*" conductor: $k_1 = 0.743$ and $k_2 = 0.257$ for the outer layer; $k_1 = 0.742$ and $k_2 = 0.258$ for the middle layer; and $k_1 = 0.741$ and $k_2 = 0.259$ for the inner layer The formulation proposed by its authors is presented below.

k_1 is calculated from the circular flux internal to the layer mean radius, ϕ_i, and the total circular flux in the layer, ϕ_t, as follows:

$$k_1 = \frac{\phi_i}{\phi_t} = \frac{S_i}{S_t}\frac{A_i}{A_t}\frac{R_o}{R_m} \tag{B.5}$$

where R_o and R_m are the outer and mean radius of the layer, respectively. A_t is the total tubular area of the layer, bounded by its internal and external radius, given by:

$$A_t = \pi\left[R_o^2 - (R_o - d)^2\right] \tag{B.6}$$

A_i is the tubular area bounded by the inner and mean readius of the layer, given by:

$$A_i = \pi\left[R_m^2 - (R_o - d)^2\right] \tag{B.7}$$

$St = \pi d^2/4$ in (B.5) is the cross-sectional area of the wire in the layer and S_i is the fraction of this area, within the mean radius of the layer, as depicted in Fig. B.1. S_i is calculated from S_t and S_o, as follows

$$S_i = S_t - S_o \tag{B.8}$$

where S_o is the fraction of the cross-sectional area of the wire external to the mean

radius of the layer, given by:

$$S_o = \frac{1}{2}\left[\frac{d^2}{4}(\alpha - \sin\alpha) - R_m^2(\beta - \sin\beta)\right] \tag{B.9}$$

where α is the central angle, given by

$$\alpha = 2\pi - 2\arcsin\left(\frac{x}{r_c}\right) \tag{B.10}$$

where x is

$$x = \frac{d}{2}\sqrt{1 - \left(\frac{d}{R_m}\right)^2} \tag{B.11}$$

and the angle β in (B.9) is

$$\beta = 2\arcsin\left(\frac{x}{R_m}\right) \tag{B.12}$$

k_2, in turn, is given by $k_2 = 1 - k_1$.

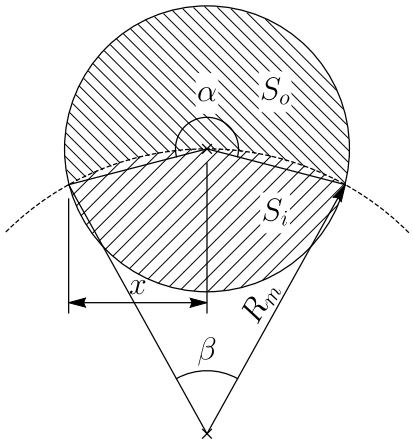

Figure B.1: Cross-section of the wire and its internal and external fractions to the layer mean radius.

It should be noted that, in the existing models [15, 16], k_1 and k_2 are only considered for the aluminum layers. The current in the steel core, in turn, is assumed to be concentrated in the outer radius of the steel core, neglecting the circular flux within it.

Appendix C

Calculation of Thermal Balance Equation Terms

This section presents the method of calculating the terms of the thermal balance equation (2.17) that depend on the weather conditions (P_r, P_c and Q_s) according to ANEEL Technical Note 38/2005 [29], which is based on the document of CIGRÉ WG 22.12 [28]. All of the following quantities are in SI units.

C.1 Radiative Cooling

The heat losses by radiation P_r are calculated by

$$P_r = \sigma_{SB}\ \varepsilon\ \pi\ D\left[(T_c + 273)^4 - (T_a + 273)^4\right] \tag{C.1}$$

where σ_{SB} and ε are the *Stefan-Bolzmann* and the conductor emissivity constants, respectively. $D$is the conductor outer diameter. T_c and T_a are the conductor surface and ambient temperature, respectively.

C.2 Convective Cooling

Heat losses by convection P_c are calculated by

$$P_c = \pi\ \lambda_f\ (T_c - T_a)\ Nu \tag{C.2}$$

where λ_f is the thermal conductivity of air, calculated by

$$\lambda_f = 2.42 \cdot 10^{-2} + 7.2 \cdot 10^{-5} T_f \tag{C.3}$$

with the temperature T_f given by

$$T_f = \frac{T_c + T_a}{2} \tag{C.4}$$

Nu in (C.2) is the *Nusselt* number, which depends on the wind speed v, as described below in section C.2.1 for $v > 0.5$ m/s, section C.2.2 for $v = 0$ m/s and section C.2.3 for $0 < v < 0.5$ m/s.

C.2.1 Forced Convective Cooling

In the case of forced convective cooling, i.e., when the wind speed is higher than 0.5 m/s, Nu is given by

$$Nu = B_2 \cdot Re^{m_2} \tag{C.5}$$

where B_2 and m_2 are constants depending on the conductor roughness RR (C.6), and the *Reynolds* number Re (C.7), as related in Table C.1.

$$RR = \frac{d}{2(D - 2d)} \tag{C.6}$$

where d is the diameter of the wires in the conductor outer layer.

$$Re = \frac{D \cdot v \cdot DRA}{v_f} \tag{C.7}$$

where v is the wind speed, and DRA is the relative air density, given by

$$DRA = \exp(-1.16 \cdot 10^{-4} h) \tag{C.8}$$

where h is the mean height of the line. v_f in (C.7) is the dynamic viscosity of air, given by

$$v_f = 1.32 \cdot 10^{-5} + 9.5 \cdot 10^{-8} T_f \tag{C.9}$$

Table C.1: Constants B_2 e m_2

Roughness	***Reynolds* number**	B_2	m_2
$0.05 < RR < 0.718$	$100 < Re < 2650$	0.641	0.471
$RR < 0.05$	$2650 < Re < 50000$	0.178	0.633
$0.05 < RR < 0.718$	$2650 < Re < 50000$	0.048	0.800

C.2.2 Natural Convective Cooling

In the case of natural convection, which corresponds to zero wind speed, Nu is calculated by

$$Nu = A_2(G_r \cdot N_{PRA})^{n_2} \tag{C.10}$$

where G_r and N_{PRA} are the *Grashof* and *Prandl* numbers, calculated by C.11 and C.12, respectively. A_2 and n_2 depend on the product of G_r and N_{PRA}, as given in Table C.2.

$$G_r = \frac{D^3(T_c - T_a)g}{(T_f + 273){v_f}^2} \tag{C.11}$$

where g is acceleration due to gravity.

$$N_{PRA} = 0.715 - 2.5 \cdot 10^{-4} T_f \tag{C.12}$$

Table C.2: Constants A_2 and n_2

$G_r \cdot N_{PRA}$		A_2	n_2
from	to		
100	10^4	0.850	0.188
10^4	10^6	0.480	0.250

C.2.3 Cooling at Low Wind Speeds

In the case of low wind speeds ($0 < v < 0.5$ m/s), P_c is the highest value calculated by the following three methods

- Calculate P_c from (C.2) using the *Nusselt* number in (C.13), assuming $\delta = 45°$

  $$Nu_\delta = Nu_{90°}[A_1 + B_2(\sin\delta)^{m1}] \tag{C.13}$$

  where A_1, B_2 and m_1 are given in Table C.3. $Nu_{90°}$ is the *Nusselt* number calculated using (C.5).

- Calculate P_c using (C.2) assuming $Nu = 0.55Nu_{90°}$;

- Calculate P_c using (C.2) assuming Nu calculated using (C.10).

Table C.3: Constants A_1, B_2 e m_1

Angle of attack	A_1	B_2	m_1
$0° < \delta < 24°$	0.42	0.68	1.08
$24° < \delta < 90°$	0.42	0.58	0.90

C.3 Solar Heating

The heat gain from solar radiation Q_s is calculated by

$$Q_s = \alpha_s \cdot D \cdot S \tag{C.14}$$

where S is the solar radiation, D is the conductor outer diameter, and α_s is the absorptivity of conductor surface.

Appendix D

Approximations of the Wires' Geometry for the Electromagnetic Modeling

D.1 Cross and Longitudinal Section of the Wires

In the model presented in section 4.2, the cross and longitudinal section of the wires are approximated to the ellipses formed by the intersection of a cylinder, with the same radius of the wire, and the xy-plane $\mathcal{P}_h$ and xz-plane $\mathcal{P}_v$, as depicted in Fig. D.1 and Fig. D.2, respectively.

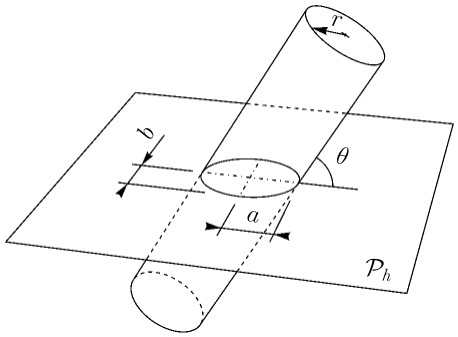

Figure D.1: Intersection of the cylinder with radius r and the xy-plane $\mathcal{P}_h$, forming the ellipse of axes $a = r/\sin\theta$ and $b = r$.

Considering the angle between the cylinder and $\mathcal{P}_h$ equal to the stranding angle of the layer θ (4.3), the ellipse formed by their intersection has then the semi-minor axis $b = r$ and semi-major axis $a = r/\sin\theta$. The intersection of this cylinder and $\mathcal{P}_v$ forms an ellipse with semi-minor axis $b = r$ and semi-major axis $c = r/\sin(\pi/2 - \theta) = r/\cos\theta$. Since the area of an ellipse with semi-axes a and b is given by $S_{ab} = \pi ab$, the cross-sectional area of the wire in the i-th layer is $S_{ellipse,t} = \pi r^2/\sin\theta_i = A_i/\sin\theta_i$, where r is the radius of the wire and A_i is the cross-sectional area of the cylinder.

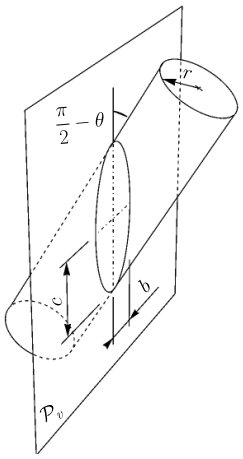

Figure D.2: Intersection of the cylinder with radius r and the xz-plane $\mathcal{P}_v$, forming the ellipse of axes $c = r/\cos\theta$ and $b = r$.

Let n_i be the number of wires in the layer i, its cross-sectional area is defined as follows

$$At_i = n_i A_i / \sin\theta_i \tag{D.1}$$

Similarly, the area of the longitudinal section of the wire in layer i is $S_{elippse,\ell} = A_i/\cos\theta_i$, and the longitudinal area of the layer is

$$A\ell_i = n_i A_i / \cos\theta_i \tag{D.2}$$

D.2 Fraction of the Cross-Section of the Wires

The fraction of the cross-sectional area of the wire at a radial distance r to the center of the conductor, see Fig. D.3, is composed of the area of the circular segment of radius r and central angle β, and the difference of the cross-sectional area of the wire and its elliptical segment with the central angle α. For the i-th layer, the fraction of the cross-sectional area of the wire at a radial distance r to the center of the conductor is given by

$$St_i(r) = A_i/\sin\theta_i - Ses_i(r) + Scs_i(r) \tag{D.3}$$

where Ses_i and Scs_i are the elliptical and circular segment, respectively. The elliptical segment in layer i at a radial distance r is given by

$$Ses_i(r) = d_i^2 \left\{\alpha_i(r) - \sin\left[\alpha_i(r)\right]\right\} / \left(8\sin\theta_i\right) \tag{D.4}$$

where d_i is the diameter of the wire and α_i is the central angle, given by

$$\alpha_i(r) = \pi - 2\gamma_i(r) \tag{D.5}$$

and the angle γ_i is

$$\gamma_i(r) = \arcsin\left\{\frac{D_i - d_i}{d_i}\tan^2\theta_i - \sqrt{1 + \left(\frac{\tan\theta_i}{d_i}\right)^2\left[(D_i - d_i)^2 - (2r\cos\theta_i)^2\right]}\right\} \tag{D.6}$$

where D_i is the outer diameter of layer i. Scs_i in (D.3) is the circular segment at a radial distance r to the center of the conductor, given by

$$Scs_i(r) = r^2\left\{\beta_i(r) - \sin\left[\beta_i(r)\right]\right\}/2 \tag{D.7}$$

where β_i is the central angle, given by

$$\beta_i(r) = \pi - 2\varphi_i(r) \tag{D.8}$$

and the angle φ_i is

$$\varphi_i(r) = \arcsin\left[\frac{D_i - d_i}{2\,r\cos^2\theta_i} - \frac{\sqrt{d_i^2 + (D_i - d_i)^2\tan^2\theta_i - (2\,r\sin^2\theta_i)}}{2\,r\cos\theta_i}\right] \tag{D.9}$$

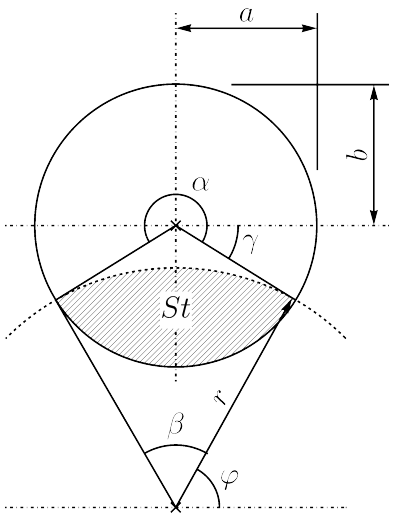

Figure D.3: Fraction of the cross-sectional area of the wire at a radial distance r.

Appendix E

Functions to Represent the Measured Complex Relative Permeability

The following polynomial functions represent the variation of the complex relative permeability $\overline{\mu}_r$ with the magnetic field strength h, of the steel core taken from an ACSR "*Duck*" conductor, measured in section 3.2 for temperatures from 40 to 230 °C in steps of 10 °C. Functions are divided into two groups, one for $h < 1200$ A/m, and the other for $h \geq 1200$ A/m. The following, from (E.1) to (E.20), represent $\overline{\mu}_r$ for $h < 1200$ A/m.

$$\begin{aligned}\overline{\mu}_r 40a(h) = {} & \left(2.6885 \times 10^{-5}\right) h^2 + \left(3.6879 \times 10^{-2}\right) h + 4.2636 \times 10^{1} \\ & - j\left[\left(1.5914 \times 10^{-11}\right) h^4 - \left(1.477 \times 10^{-8}\right) h^3 + \left(4.0158 \times 10^{-5}\right) h^2 \right. \\ & \left. + \left(1.4214 \times 10^{-2}\right) h + 3.3592 \times 10^{-2}\right]\end{aligned} \tag{E.1}$$

$$\begin{aligned}\overline{\mu}_r 50a(h) = {} & \left(-2.7831 \times 10^{-11}\right) h^4 + \left(9.4468 \times 10^{-8}\right) h^3 - \left(6.2491 \times 10^{-5}\right) h^2 \\ & + \left(6.1102 \times 10^{-2}\right) h + 3.9554 \times 10^{1} - j\left[\left(1.1417 \times 10^{-16}\right) h^6 \right. \\ & - \left(4.3933 \times 10^{-13}\right) h^5 + \left(6.4542 \times 10^{-10}\right) h^4 - \left(4.0516 \times 10^{-7}\right) h^3 \\ & \left. + \left(1.367 \times 10^{-4}\right) h^2 + \left(6.6605 \times 10^{-3}\right) h + 5.9882 \times 10^{-3}\right]\end{aligned} \tag{E.2}$$

$$\begin{aligned}\overline{\mu}_r 60a(h) = &\left(-2.8804 \times 10^{-11}\right) h^4 + \left(1.0811 \times 10^{-7}\right) h^3 - \left(6.5371 \times 10^{-5}\right) h^2 \\ &+ \left(3.6578 \times 10^{-2}\right) h + 5.5605 \times 10^{1} - j\big[\left(-5.3414 \times 10^{-14}\right) h^5 \\ &+ \left(2.0588 \times 10^{-10}\right) h^4 - \left(2.1743 \times 10^{-7}\right) h^3 + \left(1.1891 \times 10^{-4}\right) h^2 \\ &+ \left(9.3059 \times 10^{-3}\right) h + 1.0368 \times 10^{-1}\big]\end{aligned} \tag{E.3}$$

$$\begin{aligned}\overline{\mu}_r 70a(h) = &\left(-1.6108 \times 10^{-13}\right) h^5 + \left(4.2465 \times 10^{-10}\right) h^4 - \left(3.3068 \times 10^{-7}\right) h^3 \\ &+ \left(1.1666 \times 10^{-4}\right) h^2 + \left(4.712 \times 10^{-3}\right) h + 5.5955 \times 10^{1} \\ &- j\big[\left(-8.4114 \times 10^{-14}\right) h^5 + \left(2.9064 \times 10^{-10}\right) h^4 - \left(2.7983 \times 10^{-7}\right) h^3 \\ &+ \left(1.3405 \times 10^{-4}\right) h^2 + \left(9.1691 \times 10^{-3}\right) h + 8.9918 \times 10^{-2}\big]\end{aligned} \tag{E.4}$$

$$\begin{aligned}\overline{\mu}_r 80a(h) = &\left(-2.1586 \times 10^{-13}\right) h^5 + \left(5.7189 \times 10^{-10}\right) h^4 - \left(4.7005 \times 10^{-7}\right) h^3 \\ &+ \left(1.6254 \times 10^{-4}\right) h^2 + \left(2.5229 \times 10^{-2}\right) h + 4.5983 \times 10^{1} \\ &- j\big[\left(-5.1574 \times 10^{-14}\right) h^5 + \left(2.1886 \times 10^{-10}\right) h^4 - \left(1.9759 \times 10^{-7}\right) h^3 \\ &+ \left(9.4434 \times 10^{-5}\right) h^2 + \left(9.128 \times 10^{-3}\right) h + 6.5457 \times 10^{-2}\big]\end{aligned} \tag{E.5}$$

$$\begin{aligned}\overline{\mu}_r 90a(h) = &\left(-5.9739 \times 10^{-11}\right) h^4 + \left(2.1074 \times 10^{-7}\right) h^3 - \left(1.6323 \times 10^{-4}\right) h^2 \\ &+ \left(9.1046 \times 10^{-2}\right) h + 3.7439 \times 10^{1} - j\big[\left(-4.1903 \times 10^{-19}\right) h^7 \\ &+ \left(1.7334 \times 10^{-15}\right) h^6 - \left(2.8125 \times 10^{-12}\right) h^5 + \left(2.3623 \times 10^{-9}\right) h^4 \\ &- \left(1.0407 \times 10^{-6}\right) h^3 + \left(2.5766 \times 10^{-4}\right) h^2 - \left(1.1949 \times 10^{-3}\right) h \\ &+ 9.8076 \times 10^{-3}\big]\end{aligned} \tag{E.6}$$

$$\begin{aligned}\overline{\mu}_r 100a(h) = &\left(-7.798 \times 10^{-11}\right) h^4 + \left(1.3773 \times 10^{-7}\right) h^3 + \left(4.176 \times 10^{-5}\right) h^2 \\ &+ \left(1.5152 \times 10^{-3}\right) h + 3.2639 \times 10^{1} - j\big[\left(-2.9854 \times 10^{-14}\right) h^5 \\ &+ \left(1.3012 \times 10^{-10}\right) h^4 - \left(4.8291 \times 10^{-8}\right) h^3 + \left(3.6936 \times 10^{-5}\right) h^2 \\ &+ \left(8.5098 \times 10^{-3}\right) h + 2.4232 \times 10^{-2}\big]\end{aligned} \tag{E.7}$$

$$\begin{aligned}\overline{\mu}_r 110a(h) = &\left(-1.1471 \times 10^{-10}\right) h^4 + \left(2.668 \times 10^{-7}\right) h^3 - \left(1.0076 \times 10^{-4}\right) h^2 \\ &+ \left(3.567 \times 10^{-2}\right) h + 5.8501 \times 10^{1} - j\big[\left(1.7246 \times 10^{-10}\right) h^4 \\ &- \left(1.6199 \times 10^{-7}\right) h^3 + \left(7.8778 \times 10^{-5}\right) h^2 + \left(1.3106 \times 10^{-2}\right) h \\ &+ 1.289 \times 10^{-1}\big]\end{aligned} \tag{E.8}$$

$$\begin{aligned}\overline{\mu}_r 120a(h) = &\left(3.6531 \times 10^{-14}\right) h^5 - \left(1.8053 \times 10^{-10}\right) h^4 + \left(2.8318 \times 10^{-7}\right) h^3 \\ &- \left(6.9057 \times 10^{-5}\right) h^2 + \left(2.2583 \times 10^{-2}\right) h + 5.202 \times 10^{1} \\ &- j\big[\left(-1.5901 \times 10^{-14}\right) h^5 + \left(1.6039 \times 10^{-10}\right) h^4 - \left(7.7746 \times 10^{-8}\right) h^3 \\ &+ \left(3.9447 \times 10^{-5}\right) h^2 + \left(1.5719 \times 10^{-2}\right) h + 4.9825 \times 10^{-2}\big]\end{aligned} \tag{E.9}$$

$$\begin{aligned}\overline{\mu}_r 130a(h) = &\left(-1.3494 \times 10^{-10}\right) h^4 + \left(3.1503 \times 10^{-7}\right) h^3 - \left(1.228 \times 10^{-4}\right) h^2 \\ &+ \left(3.4433 \times 10^{-2}\right) h + 5.9479 \times 10^{1} - j\big[\left(-8.8847 \times 10^{-14}\right) h^5 \\ &+ \left(3.9571 \times 10^{-10}\right) h^4 - \left(3.0886 \times 10^{-7}\right) h^3 + \left(1.3599 \times 10^{-4}\right) h^2 \\ &+ \left(8.426 \times 10^{-3}\right) h + 1.3423 \times 10^{-1}\big]\end{aligned} \tag{E.10}$$

$$\begin{aligned}\overline{\mu}_r 140a(h) = &\left(-5.0449 \times 10^{-13}\right) h^5 + \left(1.2955 \times 10^{-9}\right) h^4 - \left(1.0607 \times 10^{-6}\right) h^3 \\ &+ \left(3.8234 \times 10^{-4}\right) h^2 - \left(1.877 \times 10^{-2}\right) h + 5.5126 \times 10^{1} \\ &- j\big[\left(-4.2515 \times 10^{-13}\right) h^5 + \left(1.4166 \times 10^{-9}\right) h^4 - \left(1.3163 \times 10^{-6}\right) h^3 \\ &+ \left(5.1947 \times 10^{-4}\right) h^2 - \left(3.9989 \times 10^{-2}\right) h + 6.8141 \times 10^{-1}\big]\end{aligned} \tag{E.11}$$

$$\begin{aligned}\overline{\mu}_r 150a(h) = &\left(-4.219 \times 10^{-13}\right) h^5 + \left(1.0301 \times 10^{-9}\right) h^4 - \left(7.562 \times 10^{-7}\right) h^3 \\ &+ \left(2.2962 \times 10^{-4}\right) h^2 + \left(2.0146 \times 10^{-2}\right) h + 4.7079 \times 10^{1} \\ &- j\big[\left(-3.521 \times 10^{-13}\right) h^5 + \left(1.2134 \times 10^{-9}\right) h^4 - \left(1.0989 \times 10^{-6}\right) h^3 \\ &+ \left(4.2484 \times 10^{-4}\right) h^2 - \left(2.8977 \times 10^{-2}\right) h + 5.0313 \times 10^{-1}\big]\end{aligned} \tag{E.12}$$

$$\begin{aligned}\overline{\mu}_r 160a(h) = &\left(-3.7968 \times 10^{-13}\right) h^5 + \left(8.9733 \times 10^{-10}\right) h^4 - \left(6.051 \times 10^{-7}\right) h^3 \\ &+ \left(1.8063 \times 10^{-4}\right) h^2 - \left(1.3264 \times 10^{-2}\right) h + 5.9028 \times 10^{1} \\ &- j\big[\left(-5.5127 \times 10^{-13}\right) h^5 + \left(1.7857 \times 10^{-9}\right) h^4 - \left(1.6339 \times 10^{-6}\right) h^3 \\ &+ \left(6.0389 \times 10^{-4}\right) h^2 - \left(4.8864 \times 10^{-2}\right) h + 8.2374 \times 10^{-1}\big]\end{aligned} \tag{E.13}$$

$$\begin{aligned}\overline{\mu}_r 170a(h) = &\left(-3.0133 \times 10^{-13}\right) h^5 + \left(7.8444 \times 10^{-10}\right) h^4 - \left(6.4029 \times 10^{-7}\right) h^3 \\ &+ \left(2.3579 \times 10^{-4}\right) h^2 + \left(1.2315 \times 10^{-2}\right) h + 3.7152 \times 10^{1} \\ &- j\big[\left(-3.9237 \times 10^{-13}\right) h^5 + \left(1.3862 \times 10^{-9}\right) h^4 - \left(1.3446 \times 10^{-6}\right) h^3 \\ &+ \left(5.4632 \times 10^{-4}\right) h^2 - \left(5.3693 \times 10^{-2}\right) h + 8.9016 \times 10^{-1}\big]\end{aligned} \tag{E.14}$$

$$\begin{aligned}\overline{\mu}_r 180a(h) = &\left(4.0211 \times 10^{-9}\right) h^3 + \left(6.6013 \times 10^{-5}\right) h^2 - \left(6.022 \times 10^{-3}\right) h \\ &+ 4.8202 \times 10^{1} - j\big[\left(-2.1116 \times 10^{-18}\right) h^7 + \left(8.3556 \times 10^{-15}\right) h^6 \\ &- \left(1.2652 \times 10^{-11}\right) h^5 + \left(9.3504 \times 10^{-9}\right) h^4 - \left(3.4041 \times 10^{-6}\right) h^3 \\ &+ \left(5.8539 \times 10^{-4}\right) h^2 - \left(1.6129 \times 10^{-2}\right) h + 7.209 \times 10^{-2}\big]\end{aligned} \tag{E.15}$$

$$\begin{aligned}\overline{\mu}_r 190a(h) = &\left(-7.0027 \times 10^{-14}\right) h^5 + \left(1.4964 \times 10^{-10}\right) h^4 - \left(2.704 \times 10^{-8}\right) h^3 \\ &- \left(2.1166 \times 10^{-5}\right) h^2 + \left(1.218 \times 10^{-2}\right) h + 4.6842 \times 10^{1} \\ &- j\big[\left(1.2455 \times 10^{-10}\right) h^4 - \left(1.1137 \times 10^{-7}\right) h^3 + \left(4.5145 \times 10^{-5}\right) h^2 \\ &+ \left(1.2642 \times 10^{-2}\right) h + 2.2459 \times 10^{-1}\big]\end{aligned} \tag{E.16}$$

$$\begin{aligned}\overline{\mu}_r 200a(h) = &\left(-5.1408 \times 10^{-14}\right) h^5 + \left(1.1999 \times 10^{-10}\right) h^4 - \left(2.7695 \times 10^{-8}\right) h^3 \\ &- \left(4.2039 \times 10^{-5}\right) h^2 + \left(3.8148 \times 10^{-2}\right) h + 3.183 \times 10^{1} \\ &- j\big[\left(6.8642 \times 10^{-11}\right) h^4 - \left(6.8829 \times 10^{-8}\right) h^3 + \left(3.9301 \times 10^{-5}\right) h^2 \\ &+ \left(3.5942 \times 10^{-3}\right) h + 4.0189 \times 10^{-2}\big]\end{aligned} \tag{E.17}$$

$$\begin{aligned}\overline{\mu}_r 210a(h) = &\left(-4.1136\times10^{-12}\right)h^4 + \left(3.5073\times10^{-8}\right)h^3 - \left(1.5271\times10^{-5}\right)h^2 \\ &+ \left(1.2142\times10^{-2}\right)h + 3.6892\times10^{1} - j\big[\left(3.0651\times10^{-11}\right)h^4 \\ &- \left(1.059\times10^{-8}\right)h^3 + \left(7.9712\times10^{-6}\right)h^2 + \left(9.0993\times10^{-3}\right)h \\ &+ 1.3024\times10^{-1}\big]\end{aligned} \tag{E.18}$$

$$\begin{aligned}\overline{\mu}_r 220a(h) = &\left(7.0764\times10^{-14}\right)h^5 - \left(2.1119\times10^{-10}\right)h^4 + \left(2.199\times10^{-7}\right)h^3 \\ &- \left(6.0648\times10^{-5}\right)h^2 + \left(8.5904\times10^{-3}\right)h + 3.5103\times10^{1} \\ &- j\big[\left(2.1555\times10^{-11}\right)h^4 - \left(1.2824\times10^{-8}\right)h^3 + \left(1.983\times10^{-5}\right)h^2 \\ &+ \left(8.6862\times10^{-3}\right)h + 1.3277\times10^{-1}\big]\end{aligned} \tag{E.19}$$

$$\begin{aligned}\overline{\mu}_r 230a(h) = &\left(-2.9763\times10^{-14}\right)h^5 + \left(6.1378\times10^{-11}\right)h^4 + \left(1.9996\times10^{-8}\right)h^3 \\ &- \left(6.6278\times10^{-5}\right)h^2 + \left(4.2803\times10^{-2}\right)h + 2.5934\times10^{1} \\ &- j\big[\left(3.4903\times10^{-11}\right)h^4 - \left(3.6432\times10^{-8}\right)h^3 + \left(2.5456\times10^{-5}\right)h^2 \\ &+ \left(5.4394\times10^{-3}\right)h + 4.7129\times10^{-2}\big]\end{aligned} \tag{E.20}$$

The following functions, from (E.21) to (E.40), represent $\overline{\mu}_r$ for $h \geq 1200$ A/m.

$$\begin{aligned}\overline{\mu}_r 40b(h) = &\left(-1.35\times10^{-21}\right)h^7 + \left(2.8829\times10^{-17}\right)h^6 - \left(2.5595\times10^{-13}\right)h^5 \\ &+ \left(1.2174\times10^{-9}\right)h^4 - \left(3.3222\times10^{-6}\right)h^3 + \left(5.1235\times10^{-3}\right)h^2 \\ &- 4.0008\,h + 1.3209\times10^{3} - j\big[\left(1.7864\times10^{-21}\right)h^7 \\ &- \left(3.0615\times10^{-17}\right)h^6 + \left(2.0087\times10^{-13}\right)h^5 - \left(5.9415\times10^{-10}\right)h^4 \\ &+ \left(5.7449\times10^{-7}\right)h^3 + \left(7.3379\times10^{-4}\right)h^2 - 1.6508\,h \\ &+ 8.2987\times10^{2}\big]\end{aligned} \tag{E.21}$$

$$\begin{aligned}\overline{\mu}_r 50b(h) = &\left(-2.2298\times10^{-21}\right)h^7 + \left(4.4844\times10^{-17}\right)h^6 - \left(3.7499\times10^{-13}\right)h^5 \\ &+ \left(1.6807\times10^{-9}\right)h^4 - \left(4.3258\times10^{-6}\right)h^3 + \left(6.3035\times10^{-3}\right)h^2 \\ &- 4.6664\,h + 1.448\times10^{3} - j\big[\left(7.2797\times10^{-18}\right)h^6 \\ &- \left(1.3239\times10^{-13}\right)h^5 + \left(9.7241\times10^{-10}\right)h^4 - \left(3.646\times10^{-6}\right)h^3 \\ &+ \left(7.186\times10^{-3}\right)h^2 - 6.7703\,h + 2.4565\times10^{3}\big]\end{aligned} \tag{E.22}$$

$$\begin{aligned}\overline{\mu}_r 60b(h) = &\left(-1.7717 \times 10^{-21}\right) h^7 + \left(3.575 \times 10^{-17}\right) h^6 - \left(2.9945 \times 10^{-13}\right) h^5 \\ &+ \left(1.3402 \times 10^{-9}\right) h^4 - \left(3.425 \times 10^{-6}\right) h^3 + \left(4.9015 \times 10^{-3}\right) h^2 \\ &- 3.4753\, h + 1.0291 \times 10^3 - j\big[\left(-2.969 \times 10^{-21}\right) h^7 \\ &+ \left(6.5761 \times 10^{-17}\right) h^6 - \left(6.1153 \times 10^{-13}\right) h^5 + \left(3.0799 \times 10^{-9}\right) h^4 \\ &- \left(8.989 \times 10^{-6}\right) h^3 + \left(1.4933 \times 10^{-2}\right) h^2 - \left(1.2669 \times 10^{1}\right) h \\ &+ 4.2782 \times 10^3\big]\end{aligned} \tag{E.23}$$

$$\begin{aligned}\overline{\mu}_r 70b(h) = &\left(-1.8397 \times 10^{-21}\right) h^7 + \left(3.6156 \times 10^{-17}\right) h^6 - \left(2.939 \times 10^{-13}\right) h^5 \\ &+ \left(1.2709 \times 10^{-9}\right) h^4 - \left(3.1197 \times 10^{-6}\right) h^3 + \left(4.2473 \times 10^{-3}\right) h^2 \\ &- 2.8008\, h + 7.6923 \times 10^2 - j\big[\left(-6.2456 \times 10^{-21}\right) h^7 \\ &+ \left(1.2967 \times 10^{-16}\right) h^6 - \left(1.1287 \times 10^{-12}\right) h^5 + \left(5.3186 \times 10^{-9}\right) h^4 \\ &- \left(1.4541 \times 10^{-5}\right) h^3 + \left(2.2733 \times 10^{-2}\right) h^2 - \left(1.8336 \times 10^{1}\right) h \\ &+ 5.9214 \times 10^3\big]\end{aligned} \tag{E.24}$$

$$\begin{aligned}\overline{\mu}_r 80b(h) = &\left(-2.6247 \times 10^{-21}\right) h^7 + \left(5.0985 \times 10^{-17}\right) h^6 - \left(4.0863 \times 10^{-13}\right) h^5 \\ &+ \left(1.7386 \times 10^{-9}\right) h^4 - \left(4.1967 \times 10^{-6}\right) h^3 + \left(5.6418 \times 10^{-3}\right) h^2 \\ &- 3.7481\, h + 1.0429 \times 10^3 - j\big[\left(-6.7297 \times 10^{-21}\right) h^7 \\ &+ \left(1.3657 \times 10^{-16}\right) h^6 - \left(1.1596 \times 10^{-12}\right) h^5 + \left(5.3165 \times 10^{-9}\right) h^4 \\ &- \left(1.4092 \times 10^{-5}\right) h^3 + \left(2.1232 \times 10^{-2}\right) h^2 - \left(1.6321 \times 10^{1}\right) h \\ &+ 4.9708 \times 10^3\big]\end{aligned} \tag{E.25}$$

$$\begin{aligned}\overline{\mu}_r 90b(h) = &\left(-1.4121 \times 10^{-21}\right) h^7 + \left(2.683 \times 10^{-17}\right) h^6 - \left(2.0766 \times 10^{-13}\right) h^5 \\ &+ \left(8.3492 \times 10^{-10}\right) h^4 - \left(1.8278 \times 10^{-6}\right) h^3 + \left(2.0245 \times 10^{-3}\right) h^2 \\ &- \left(7.679 \times 10^{-1}\right) h + 2.8068 \times 10^1 - j\big[\left(-8.547 \times 10^{-21}\right) h^7 \\ &+ \left(1.7094 \times 10^{-16}\right) h^6 - \left(1.4263 \times 10^{-12}\right) h^5 + \left(6.4043 \times 10^{-9}\right) h^4 \\ &- \left(1.6565 \times 10^{-5}\right) h^3 + \left(2.4269 \times 10^{-2}\right) h^2 - \left(1.8084 \times 10^{1}\right) h \\ &+ 5.3153 \times 10^3\big]\end{aligned} \tag{E.26}$$

$$\begin{aligned}\overline{\mu}_r 100b(h) = &\left(-7.6573\times10^{-19}\right)h^6 + \left(1.6105\times10^{-14}\right)h^5 - \left(1.3638\times10^{-10}\right)h^4 \\ &+ \left(5.9544\times10^{-7}\right)h^3 - \left(1.4254\times10^{-3}\right)h^2 + 1.8018\,h \\ &- 7.2133\times10^{2} - j\big[\left(-8.5621\times10^{-21}\right)h^7 + \left(1.6831\times10^{-16}\right)h^6 \\ &- \left(1.3762\times10^{-12}\right)h^5 + \left(6.0313\times10^{-9}\right)h^4 - \left(1.5139\times10^{-5}\right)h^3 \\ &+ \left(2.1319\times10^{-2}\right)h^2 - \left(1.4988\times10^{1}\right)h + 4.0745\times10^{3}\big]\end{aligned} \tag{E.27}$$

$$\begin{aligned}\overline{\mu}_r 110b(h) = &\left(5.1962\times10^{-22}\right)h^7 - \left(1.0967\times10^{-17}\right)h^6 + \left(9.9184\times10^{-14}\right)h^5 \\ &- \left(4.9793\times10^{-10}\right)h^4 + \left(1.4952\times10^{-6}\right)h^3 - \left(2.6892\times10^{-3}\right)h^2 \\ &+ 2.7122\,h - 9.6916\times10^{2} - j\big[\left(-3.8507\times10^{-21}\right)h^7 \\ &+ \left(7.1818\times10^{-17}\right)h^6 - \left(5.4839\times10^{-13}\right)h^5 + \left(2.1823\times10^{-9}\right)h^4 \\ &- \left(4.6873\times10^{-6}\right)h^3 + \left(4.7925\times10^{-3}\right)h^2 - \left(9.7934\times10^{-1}\right)h \\ &- 7.7242\times10^{2}\big]\end{aligned} \tag{E.28}$$

$$\begin{aligned}\overline{\mu}_r 120b(h) = &\left(-6.0273\times10^{-19}\right)h^6 + \left(1.2008\times10^{-14}\right)h^5 - \left(9.7504\times10^{-11}\right)h^4 \\ &+ \left(4.1348\times10^{-7}\right)h^3 - \left(9.8011\times10^{-4}\right)h^2 + 1.2624\,h \\ &- 4.6138\times10^{2} - j\big[\left(-2.5911\times10^{-21}\right)h^7 + \left(4.5579\times10^{-17}\right)h^6 \\ &- \left(3.1877\times10^{-13}\right)h^5 + \left(1.0904\times10^{-9}\right)h^4 - \left(1.6501\times10^{-6}\right)h^3 \\ &- \left(1.2299\times10^{-4}\right)h^2 + 3.2587\,h - 2.2331\times10^{3}\big]\end{aligned} \tag{E.29}$$

$$\begin{aligned}\overline{\mu}_r 130b(h) = &\left(-1.2171\times10^{-21}\right)h^7 + \left(2.4026\times10^{-17}\right)h^6 - \left(1.9503\times10^{-13}\right)h^5 \\ &+ \left(8.3703\times10^{-10}\right)h^4 - \left(2.0255\times10^{-6}\right)h^3 + \left(2.6901\times10^{-3}\right)h^2 \\ &- 1.679\,h + 5.0877\times10^{2} - j\big[\left(2.0078\times10^{-21}\right)h^7 \\ &- \left(4.5542\times10^{-17}\right)h^6 + \left(4.3373\times10^{-13}\right)h^5 - \left(2.258\times10^{-9}\right)h^4 \\ &+ \left(6.9949\times10^{-6}\right)h^3 - \left(1.3025\times10^{-2}\right)h^2 + \left(1.3502\times10^{1}\right)h \\ &- 5.5223\times10^{3}\big]\end{aligned} \tag{E.30}$$

$$\begin{aligned}\overline{\mu}_r 140b(h) = &\left(-1.2281 \times 10^{-21}\right) h^7 + \left(2.3688 \times 10^{-17}\right) h^6 - \left(1.8865 \times 10^{-13}\right) h^5 \\ &+ \left(7.9926 \times 10^{-10}\right) h^4 - \left(1.9264 \times 10^{-6}\right) h^3 + \left(2.5762 \times 10^{-3}\right) h^2 \\ &- 1.6326\, h + 5.0562 \times 10^2 - j\big[\left(6.1227 \times 10^{-21}\right) h^7 \\ &- \left(1.2547 \times 10^{-16}\right) h^6 + \left(1.0802 \times 10^{-12}\right) h^5 - \left(5.0743 \times 10^{-9}\right) h^4 \\ &+ \left(1.4113 \times 10^{-5}\right) h^3 - \left(2.3433 \times 10^{-2}\right) h^2 + \left(2.1604 \times 10^{1}\right) h \\ &- 8.0721 \times 10^3\big]\end{aligned} \tag{E.31}$$

$$\begin{aligned}\overline{\mu}_r 150b(h) = &\left(-8.8633 \times 10^{-22}\right) h^7 + \left(1.756 \times 10^{-17}\right) h^6 - \left(1.4429 \times 10^{-13}\right) h^5 \\ &+ \left(6.3489 \times 10^{-10}\right) h^4 - \left(1.6046 \times 10^{-6}\right) h^3 + \left(2.2804 \times 10^{-3}\right) h^2 \\ &- 1.5706\, h + 5.4788 \times 10^2 - j\big[\left(-9.0212 \times 10^{-18}\right) h^6 \\ &+ \left(1.6108 \times 10^{-13}\right) h^5 - \left(1.1842 \times 10^{-9}\right) h^4 + \left(4.6123 \times 10^{-6}\right) h^3 \\ &- \left(1.0085 \times 10^{-2}\right) h^2 + \left(1.1637 \times 10^{1}\right) h - 5.0116 \times 10^3\big]\end{aligned} \tag{E.32}$$

$$\begin{aligned}\overline{\mu}_r 160b(h) = &\left(-2.9984 \times 10^{-22}\right) h^7 + \left(6.7869 \times 10^{-18}\right) h^6 - \left(6.2462 \times 10^{-14}\right) h^5 \\ &+ \left(3.0243 \times 10^{-10}\right) h^4 - \left(8.2439 \times 10^{-7}\right) h^3 + \left(1.2187 \times 10^{-3}\right) h^2 \\ &- \left(7.8409 \times 10^{-1}\right) h + 2.9244 \times 10^2 - j\big[\left(-9.4846 \times 10^{-18}\right) h^6 \\ &+ \left(1.6905 \times 10^{-13}\right) h^5 - \left(1.2395 \times 10^{-9}\right) h^4 + \left(4.8103 \times 10^{-6}\right) h^3 \\ &- \left(1.0473 \times 10^{-2}\right) h^2 + \left(1.2034 \times 10^{1}\right) h - 5.1733 \times 10^3\big]\end{aligned} \tag{E.33}$$

$$\begin{aligned}\overline{\mu}_r 170b(h) = &\left(3.3656 \times 10^{-9}\right) h^3 - \left(5.1645 \times 10^{-5}\right) h^2 + \left(2.2331 \times 10^{-1}\right) h \\ &- 4.0699 \times 10^1 - j\big[\left(-7.709 \times 10^{-18}\right) h^6 + \left(1.389 \times 10^{-13}\right) h^5 \\ &- \left(1.034 \times 10^{-9}\right) h^4 + \left(4.097 \times 10^{-6}\right) h^3 - \left(9.1646 \times 10^{-3}\right) h^2 \\ &+ \left(1.0866 \times 10^{1}\right)\, h - 4.7982 \times 10^3\big]\end{aligned} \tag{E.34}$$

$$\begin{aligned}\overline{\mu}_r 180b(h) = &\left(7.0638 \times 10^{-13}\right) h^4 - \left(6.3376 \times 10^{-9}\right) h^3 - \left(4.7556 \times 10^{-6}\right) h^2 \\ &+ \left(1.3618 \times 10^{-1}\right)\, h - 5.7971 - j\big[\left(6.8693 \times 10^{-15}\right) h^5 \\ &- \left(1.2138 \times 10^{-10}\right) h^4 + \left(8.5697 \times 10^{-7}\right) h^3 - \left(2.9891 \times 10^{-3}\right) h^2 \\ &+ 4.9721\, h - 2.6692 \times 10^3\big]\end{aligned} \tag{E.35}$$

$$\begin{aligned}\overline{\mu}_r 190b(h) = &\left(-2.198\times10^{-21}\right)h^7+\left(4.0714\times10^{-17}\right)h^6-\left(3.0719\times10^{-13}\right)h^5\\&+\left(1.2101\times10^{-9}\right)h^4-\left(2.6458\times10^{-6}\right)h^3+\left(3.1167\times10^{-3}\right)h^2\\&-1.6505\,h+3.2618\times10^{2}-j\big[\left(-8.9425\times10^{-21}\right)h^7\\&+\left(1.7963\times10^{-16}\right)h^6-\left(1.5067\times10^{-12}\right)h^5+\left(6.8025\times10^{-9}\right)h^4\\&-\left(1.767\times10^{-5}\right)h^3+\left(2.5893\times10^{-2}\right)h^2-\left(1.9115\times10^{1}\right)h\\&+5.4789\times10^{3}\big]\end{aligned} \tag{E.36}$$

$$\begin{aligned}\overline{\mu}_r 200b(h) = &\left(-3.958\times10^{-21}\right)h^7+\left(7.6032\times10^{-17}\right)h^6-\left(6.0195\times10^{-13}\right)h^5\\&+\left(2.5302\times10^{-9}\right)h^4-\left(6.0545\times10^{-6}\right)h^3+\left(8.1679\times10^{-3}\right)h^2\\&-5.6137\,h+1.5663\times10^{3}-j\big[\left(-5.2527\times10^{-21}\right)h^7\\&+\left(1.1492\times10^{-16}\right)h^6-\left(1.0595\times10^{-12}\right)h^5+\left(5.3046\times10^{-9}\right)h^4\\&-\left(1.5424\times10^{-5}\right)h^3+\left(2.559\times10^{-2}\right)h^2-\left(2.1796\times10^{1}\right)\,h\\&+7.3504\times10^{3}\big]\end{aligned} \tag{E.37}$$

$$\begin{aligned}\overline{\mu}_r 210b(h) = &\left(-5.3272\times10^{-21}\right)h^7+\left(1.0179\times10^{-16}\right)h^6-\left(8.0202\times10^{-13}\right)h^5\\&+\left(3.359\times10^{-9}\right)h^4-\left(8.0295\times10^{-6}\right)h^3+\left(1.0886\times10^{-2}\right)h^2\\&-7.6356\,h+2.1902\times10^{3}-j\big[\left(4.2281\times10^{-21}\right)h^7\\&-\left(6.6388\times10^{-17}\right)h^6+\left(3.731\times10^{-13}\right)h^5-\left(7.2067\times10^{-10}\right)h^4\\&-\left(9.6653\times10^{-7}\right)h^3+\left(5.9862\times10^{-3}\right)h^2-8.0245\,h\\&+3.4895\times10^{3}\big]\end{aligned} \tag{E.38}$$

$$\begin{aligned}\overline{\mu}_r 220b(h) = &\left(-4.6899\times10^{-21}\right)h^7+\left(9.3211\times10^{-17}\right)h^6-\left(7.6784\times10^{-13}\right)h^5\\&+\left(3.383\times10^{-9}\right)h^4-\left(8.5697\times10^{-6}\right)h^3+\left(1.2418\times10^{-2}\right)h^2\\&-9.418\,h+2.9372\times10^{3}-j\big[\left(9.1662\times10^{-21}\right)h^7\\&-\left(1.6872\times10^{-16}\right)h^6+\left(1.256\times10^{-12}\right)h^5-\left(4.808\times10^{-9}\right)h^4\\&+\left(9.9179\times10^{-6}\right)h^3-\left(1.0539\times10^{-2}\right)h^2+5.1014\,h\\&-7.1094\times10^{2}\big]\end{aligned} \tag{E.39}$$

$$\begin{aligned}\overline{\mu}_r 230b(h) = &\left(-6.1637 \times 10^{-21}\right) h^7 + \left(1.2219 \times 10^{-16}\right) h^6 - \left(1.003 \times 10^{-12}\right) h^5 \\ &+ \left(4.3989 \times 10^{-9}\right) h^4 - \left(1.1076 \times 10^{-5}\right) h^3 + \left(1.593 \times 10^{-2}\right) h^2 \\ &- \left(1.1997 \times 10^{1}\right) h + 3.6968 \times 10^{3} - j\big[\left(1.1368 \times 10^{-20}\right) h^7 \\ &- \left(2.1296 \times 10^{-16}\right) h^6 + \left(1.6251 \times 10^{-12}\right) h^5 - \left(6.4559 \times 10^{-9}\right) h^4 \\ &+ \left(1.4144 \times 10^{-5}\right) h^3 - \left(1.672 \times 10^{-2}\right) h^2 + 9.8515\, h \\ &- 2.1984 \times 10^{3}\big]\end{aligned} \tag{E.40}$$

Appendix F

Obtaining the AC/DC Resistance Ratio of the T-ACSR "*Guinea*" Conductor Using the CIGRÉ Ampacity Calculation Methodology

This section describes the procedure performed to obtain a function $f_{R_{ac/dc}}$, representing the AC/DC resistance ratio of the T-ACSR "*Guinea*" conductor, using the DC/AC ampacity conversion proposed in the CIGRÉ ampacity calculation methodology, presented in section 2.4. It is important to highlight that this function is obtained only to illustrate how the variation of the conductor AC/DC resistance ratio with the current carried I_{ac} is considered when using the CIGRÉ methodology. It is not necessary to obtain or use this function to calculate the ampacity.

According to the CIGRÉ methodology [28], the alternating current ampacity I_{ac} of steel-cored conductors with up to three aluminum layers is obtained by converting their ampacity from DC to AC, as follows $I_{ac} = f(I_{dc})$, where I_{dc} is the conductor ampacity in direct current. As shown in section 2.4.4, this function is related to the conductor AC/DC resistance ratio, as follows $f(I_{dc}) = I_{dc}/\sqrt{R_{T_{ac}}/R_{T_{dc}}}$. And, therefore, it is possible to obtain the AC/DC resistance ratio from this equation. However, this AC/DC ratio is given as a function of I_{dc}, and a certain manipulation is needed to describe it as a function of I_{ac}.

In the case of the "*Guinea*" conductor, having a single aluminum layer and nominal cross-sectional area $A = 80{,}36$ mm^2, the ampacity conversion depends on the value of $I_k = I_{dc}/A$, being proposed a conversion equation (given in section 2.4.2) for each of the following four ranges of values of I_k, referred to below by range A, B, C and D, as follows:

- for $I_k \leq 0.742$, range A - equation (2.29);

- for $0.742 \leq I_k \leq 2.486$, range B - equation (2.30);
- for $2.486 \leq I_k \leq 3.908$, range C - equation (2.31);
- for $I_k > 3.908$, range D - equation (2.32).

The ampacity conversion, considering the nominal area of the "*Guinea*" conductor of 80,36 mm^2, and the equations from (2.29) to (2.32), is shown in Fig. F.1.

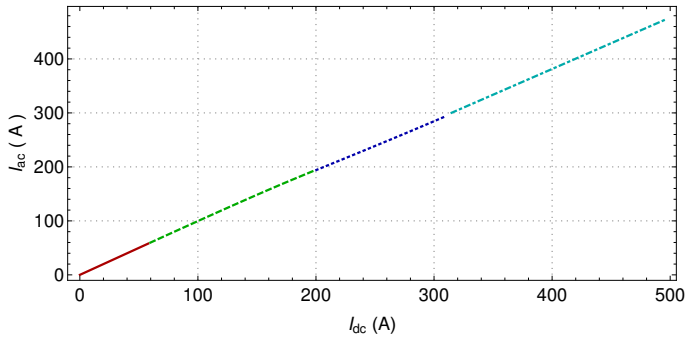

Figure F.1: Conversion of the T-ACSR "*Guinea*" conductor ampacity, from DC to AC, following CIGRÉ methodology, for current range A (——), B (- - - -), C (·····), and D (-·-·-·).

In order to obtain the AC/DC resistance ratio as a function of I_{ac}, the axes of the graph in Fig. F.1 are inverted. Then, each I_{dc} value is divided by the corresponding I_{ac} value and the result squared, since from (2.23) we have $R_{ac}/R_{dc} = (I_{dc}/I_{ac})^2$. The result is shown in Fig. F.2.

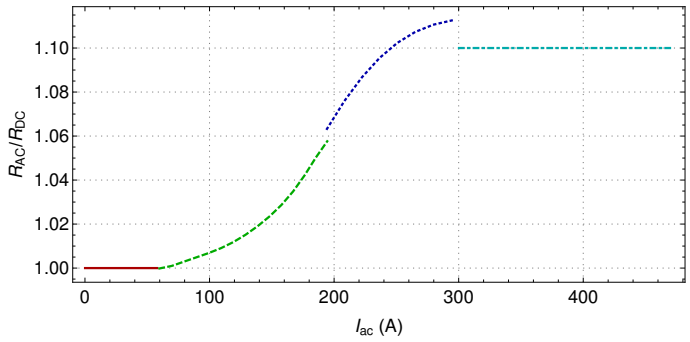

Figure F.2: Variation of the AC/DC resistance ratio of the T-ACSR "*Guinea*" conductor using the CIGRÉ methodology, for current range A (——), B (- - - -), C (·····), and D (-·-·-·).

From the graph shown in Fig. F.2, a polynomial function is obtained representing the variation of the AC/DC resistance ratio with the total current value I_{ac}. The function obtained for "*Guinea*" conductor, up to the total current value of 300 A is given by:

$$
\begin{aligned}
f_{R_{ac/dc}}(I_{ac}) = &\left(4.2411 \times 10^{-15}\right) I_{ac}^{6} - \left(3.7907 \times 10^{-12}\right) I_{ac}^{5} \\
&+ \left(1.1712 \times 10^{-9}\right) I_{ac}^{4} - \left(1.4835 \times 10^{-7}\right) I_{ac}^{3} \\
&+ \left(9.0103 \times 10^{-6}\right) I_{ac}^{2} - \left(2.0856 \times 10^{-4}\right) I_{ac} + 1.0009
\end{aligned}
\tag{F.1}
$$

Above 300 A, the function $f_{R_{ac/dc}}$ is constant, equal to 1.1.